ISSN 0914-9244
CODEN JSTEEW

Journal of
Photopolymer
Science and Technology

Volume 34 Number 2

2021

JOURNAL OF PHOTOPOLYMER SCIENCE AND TECHNOLOGY

Home Page http://www.spst-photopolymer.org
https://www.jstage.jst.go.jp/browse/photopolymer

Journal of Photopolymer Science and Technology publishes papers on the scientific progress and the technical development of photopolymers.

Editorial Board

International Advisory Board

The Editorial Office
Assoc. Prof. Hiroyuki MAYAMA
Department of Chemistry, Asahikawa Medical University, 2-1-1-1 Midorigaoka-Higashi, Asahikawa, Hokkaido 078-8510, Japan.
FAX: +81-166-68-2782, e-mail: mayama@asahikawa-med.ac.jp

Information for Contributors

Submit Manuscripts to the SPST Homepage (Journal --> Submission of Papers --> Editorial Manager). Submission is a representation that the manuscript has not been published previously elsewhere. The manuscript should be accompanied by a statement transferring copyright from the authors (or their employers-whoever holds the copyright) to the Society of Photopolymer Science and Technology. A suitable form for copyright transfer is available from the SPST Homepage. This written transfer of copyright, which previously was assumed to be implicit in the act of submitting a manuscript, is necessary under the Japan copyright law. Further information may be obtained from the "Manual for Manuscript Writing" at the SPST Homepage.

Proofs and All Correspondence: Concerning papers in the process of publication should be addressed to the Editorial Office.

Manuscript Preparation: All the papers submitted are reproduced electronically as they were. For this reason, the manuscripts should be prepared according to the Manual for Manuscript Writings shown at the SPST Homepage.

Subscription Price (Airmail Postage included):
¥12,000 (in Japan), US$ 150.00 (for Foreign)

Subscriptions, renewals, and address changes should be addressed to the Editorial Office. For the address changes, please send both old and new addresses and, if possible, include a mailing label from the wrapper of recent issue. Requests from subscribers for missing journal issues will be honored without charge only if received within six months of the issue's actual date of publication; otherwise, the issue may be purchased at the single-copy price.

Publication Charge (Reprint Order): To support a part of the cost of publication of journal pages, the author's institution is requested to pay a page charge of ¥3,000 per page (with a one-page minimum) and an article charge of ¥12,000 per article. The page charge (if honored) entitles the author to 50 free reprints. For Errata the minimum page charge is ¥3,000, with no articles charge and no free reprints.

The cover designed by M. Tsuda and M. Morishita

JOURNAL
OF
PHOTOPOLYMER SCIENCE
AND
TECHNOLOGY

Volume 34 Number 2

2021

Published by

THE SOCIETY OF PHOTOPOLYMER SCIENCE AND TECHNOLOGY

THE SOCIETY OF PHOTOPOLYMER SCIENCE AND TECHNOLOGY (SPST)

http://www.spst-photopolymer.org

President:
Minoru TSUDA
SPST & Chiba University

Director of Publication:
Hiroyuki MAYAMA
Asahikawa Meical University

Director of Scientific Program:
Masayuki ENDO
Osaka University

Director of International Affairs:
Takeo WATANABE
University of Hyogo

Director of Administration:
Takashi KARATSU
Chiba University

Office of the Administration
c/o Prof. Takashi KARATSU
Department of Applied Chemistry
and Biotechnology,
Chiba University
1-33 Yayoicho, Inage-ku,
Chiba 263-8522, Japan
Phone: +81-43-290-3366
Fax +81-43-290-3401
e-mail:office@spst-photopolymer.org

THE SPST REPRESENTATIVES 2021

Robert ALLEN, *IBM*
Tsukasa AZUMA, *Toshiba Co., Ltd.*
Teruaki HAYAKAWA, *Tokyo Institute of Technology*
Takashi HIRANO, *Sumitomo Bakelite Co., Ltd.*
Hideo HORIBE, *Osaka City University*
Masaaki KAKIMOTO, *Tokyo Institute of Technology*
Yoshio KAWAI, *Shin-Etsu Chemical Co., Ltd.*
Hiroto KUDO, *Kansai University*
Jun MIZUNO*, Waseda University*
Tomoki NAGAI, *JSR Corporation*
Hideo OHKITA, *Kyoto University*
Hiroaki OIZUMI, *Gigaphoton Inc.*
Itaru OSAKA, *Hiroshima University*
Atsushi SEKIGUCHI, *Litho Tech Japan Corporation*
Akinori SHIBUYA, *Fuji Film, Co., Ltd.*
Kuniharu TAKEI, *Osaka Prefecture University*
Minoru TSUDA, *SPST & Chiba University*
Takeo WATANABE, *University of Hyogo*
Takashi YAMASHITA, *Tokyo University of Technology*
Hitoshi ARAKI, *Toray Co., Ltd.*
Masayuki ENDO, *Osaka University*
Yoshihiko HIRAI, *Osaka Prefecture University*
Taku HIRAYAMA, *Hoya Co., Ltd.*
Takanori ICHIKI, *University of Tokyo*
Takashi KARATSU, *Chiba University*
Shin-ichi KONDO, *Gifu Pharmaceutical University*
Masayuki KUZUYA, *Chubu Gakuin University*
Seiji NAGAHARA, *Tokyo Electron Ltd.*
Tomoki NISHINO, *Ritsumeikan University*
Yasunobu OHNISHI, *University of Tokyo*
Haruyuki OKAMURA, *Osaka Prefecture University*
Shu SEKI, *Kyoto University*
Takehiro SESHIMO, *Tokyo Ohka Co., Ltd.*
Kohei SOGA, *Tokyo University of Science*
Jun TANIGUCHI, *Tokyo University of Science*
Takumi UENO, *Shinshu University*
Shinji YAMAKAWA, *University of Hyogo*
Wang YUEH, *Intel*

Notice about photocopying

Prior to photocopying any work in this publication, the permission is required from the following organization which has been delegated for copyright clearance by the copying owner of this publication.

・ In the USA
Copying Clearance Center Inc.
222 Rosewood Drive, Danvers MA 01923, USA
Tel: 1-978-750-8400, Fax: 1-978-750-4744, e-mail: info@copyright.com
http://www.copyright.com

・ Except in the USA
Japan Academic Association for Copyright Clearance (JAACC)
9-6-41 Akasaka, Minato-ku, Tokyo 107-0052, Japan
Tel: 81-3-3475-5618, Fax: 81-3-3475-5619, e-mail: info@jaacc.jp
http://www.jaacc.org

Communication

Journal of Photopolymer Science and Technology
Volume 34, Number 2 (2021) 123−126 ©2021SPST

Computational Lithography for 3-Dimensional Fine Photolithography using Sophisticated Built-in Lens Mask

Tomoaki Osumi, Akio Misaka, Kousuke Sato, Masaaki Yasuda, Masaru Sasago, and *Yoshihiko Hirai

Physics and Electronics Engineering, Graduate School of Engineering, Osaka Prefecture University

1-1, Gakuencho, Nakaku, Sakai, Osaka 599-8531, Japan
**hirai@pe.oasakafu-u.ac.jp*

Built-in lens mask lithography realizes 3D imaging by a single exposure using a conventional proximity exposure system. 3D structures are divided into seed elements with different depth of focus, and the complex amplitude of the mask is designed by combining the wavefronts that image these elements. However, due to the interference of the seeds, the three-dimensional image may be missing. For this reason, it has been necessary to set the seed pattern based on empirical knowledge. In this paper, we have developed a system to automatically design the seed pattern. The system calculates the light intensity-distribution in space and places seeds with opposite phases to cancel where excessive image remains. On the other hand, additional seeds are placed in space where light intensity is not sufficient. This procedure is repeated step by step until the required image is obtained. Computational lithography will show that this results in the required 3D image.

Keywords: Optical lithography, 3D image, Aerial image, Built-in lens mask

1. Introduction

3-dimensional fabrication has been increasing required for fine micro-scale devices such as advanced microfluidic devices, micro- and nanostructured electromechanical systems, advanced biomimetics systems, and wiring at deep steps in advanced integrated circuits.

Several beam technologies and 3-D printing technology have been proposed for the fabrication of three-dimensional (3D) micro- and nanostructures [1-6].

Si micro machining using sacrificial layers is one of promising approaches [7]. Beam-based processing methods have been proposed, such as focused ion beam deposition techniques [8] or multi-beam exposure methods based on two-photon absorption [9]. Formation of 3D structures has been demonstrated using nanoimprint techniques [10,11] or a multiple exposure technique [12] based on conventional photolithographic processing. Furthermore, microdevice fabrication has also been demonstrated using 3D printer systems [13].

However, these more conventional methods require long production times because they use multiple exposures and step-by-step processing, and they need beam scanning and/or stage movement. As a result, huge processing time is required for integrated 3 D structures.

On the other hand, novel 3D photolithography approaches that are based on single-shot exposure without beam scanning or stage movement through a photomask have been proposed, including inverse lithography [14], and holographic lithography [15-17], however, these methods could only be applied to the exposure of two-dimensional or periodic patterns. Also, they need specific optical systems such as lens or millers.

To solve these problems, we previously proposed a novel 3D photolithography method that used the multi-focusing function of built-in lens mask lithography [18] and demonstrated the 3D imaging process capability through computational lithography simulations [19-21].

Received April 1, 2021
Accepted April 27, 2021

2. 3-D Photo lithography by built-in lens mask

The built-in lens mask is an optically transparent mask with complex optical transmittance characteristics (in terms of the amplitude and phase of the optical wave). When coherent light is used to irradiate a built-in lens mask, the complex optical amplitude of the light that is transmitted through the mask is modified. Designing of the complex transmittance, multiple focused imaging could be realized by single mask and single shot. Then, imaging at voluntary focus depth could be realized. Then, 3D imaging could be realized when the 3D structures are divided into seed elements and the complex amplitude of each seed is superposed on a mask. The details of the mask and the associated processes were described theoretically and experimentally in our previous work [19,20]. However, due to the interference of the seeds, a part of three-dimensional image may be missing or unexpected ghost is coming out. For this reason, it has been necessary to set the seed pattern based on empirical knowledge.

To overcome the problem, we have developed a system to automatically design the seed pattern.

3. Automatic seed optimization

Figure 1 shows schematics of automatic seed optimization system. Firstly, the demanded 3D structure is divided into small seeds, which are usually around a quarter of exposure wavelength. Then, the optical intensity in the space is calculated by the seeds. The system calculates the light intensity-distribution in space. Then, the system calculates the light intensity-distribution in space and places seeds with opposite phases to cancel where excessive image remains. On the other hand, additional seeds are placed in space where light intensity is not sufficient. This procedure is repeated step by step until the required image is obtained. As a result, the system automatically relocates the seeds to compensate for the inconveniences.

The procedure of the seed optimization is as follows: Firstly, image intensity profile I_i(x,y,z) in space is calculated for given seed pattern. Then the differential δI between the desired profile $I_0\,(x,y,x)$ and Ii(x,y,z) is evaluated as :

$$\delta I(x,y,z) = I_0\,(x,y,x) - I_i(x,y,z). \qquad (1)$$

When the expected image intensity is weak or missing, the intensity of the seed $I_{seed}(x,y,x)$ is revised as:

$$I_{seed}(x,y,x)^{n+1} = I_{seed}(x,y,x)^{n} + \delta I(x,y,z)*f_1/n, \qquad (2)$$

where n is the number of iterations.

On the counterrally, when the image is generated on unexpected area, the intensity of seed pattern is revised as:

$$I_{seed}(x,y,x)^{n+1} = I_{seed}(x,y,x)^{n} + \delta I(x,y,z)*f_2/n, \qquad (3)$$

where f_1 and f_2 are feedback coefficients.

Beside intensity revision of the seed, phase inversion of the seed is also performed to prevent interference due to additional seed patterns with the each other.

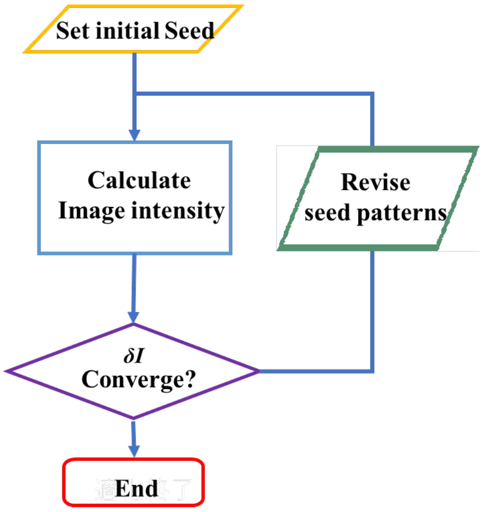

Fig. 1. Schematics of automatic seed optimization system.

4. Results and discussion

We demonstrate exposure results of novel 3D structures using the proposed systems by computational study.

Figure 2 shows line pattern on step of 20 µm in height. The space of each line is 10 µm. The gap between the mask and substrate is 60 µm. The exposure wave length λ is 365 nm. Figure 2 (a) shows initial seed pattern. Without optimization, the image intensity profile has missing portion nearby step edges as shown in Fig.2 (b) due to interference. After optimization, the missing parts are recovered and fine line pattern with 2.0 µm in width is successfully obtained.

The number of iterations for optimization was only once, where convergent parameters were f_1=0.01, and f_2=0.001, respectively.

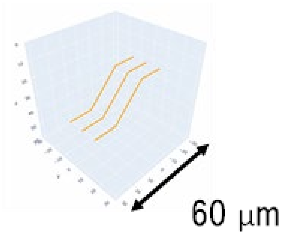

(a) Desired structure

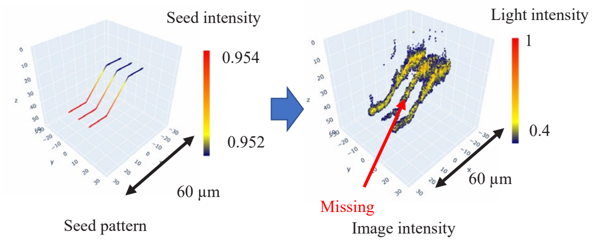

(b) Without optimization

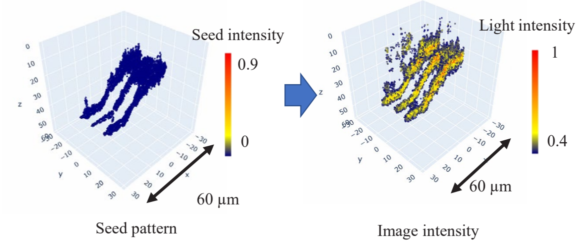

(c) After optimization ($f_1 = 0.01, f_2 = 0.001$)

Fig. 2. Line pattern along a step.

Figure 3 shows three-dimensional frame structure. There are three parallel rods of 40 µm in length with 20 µm in spacing, and connecting with each other. The exposure wave length λ is 365 nm. Without optimization of seeds, there are some missing portions due to interference. After optimization, file rod connected structure is successfully obtained as shown in Fig.3 (c), where the rod size is about 3.0 µm. In this case, the number of iterations was 4 times.

5.Conclusion

Smart optimization system of seed patterns for 3-dimensional imaging using the built-in lens mask is newly proposed. We confirmed the optimization methods is effective for elimination of fatal defects such as pattern missing due to interference.

Using the system, we demonstrated automatic optimize of seed arrangement for line pattern along a step and parallel frame structure. As a result, fine 3-dimensional photolithography is successfully confirmed by optimization of the seed using proposed smart system.

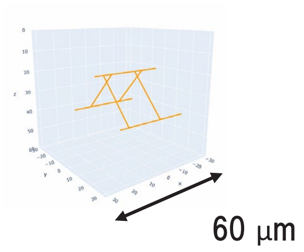

(a) Desired structure

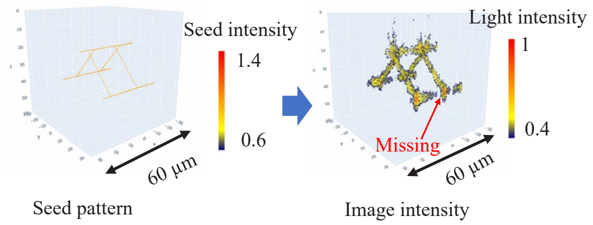

(b) Without optimization

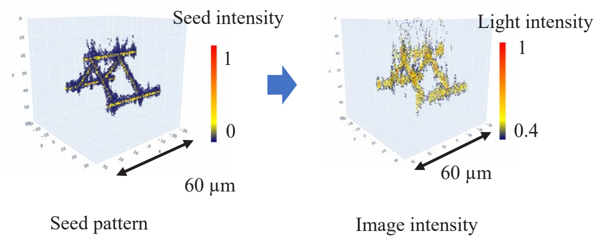

(c)After optimization ($f_1 = 0.5, f_2 = 0.05$)

Fig. 3. Parallel frame structure.

Acknowledgement

A part of this work is supported by Kakenhi (Grants-in-Aid for Scientific Research, Grant No. 2 0 K 0 5 2 8 9 (3D-Photolithography)).

References

1. M. Mao, J. He, X. Li, B. Zhang, Q. Lei, Y. Liu, and D. Li, *Adv. Micromachines,* **8** (2017) 113.
2. R. Farahani, M. Dubé, and D. Therriault, *Adv. Mater.*, **28** (2016) 5794.
3. W. Xiong, Y. Zhou, W. Hou, L. Jiang, M. Mahjouri-Samani, J. Park, X. He, Y. Gao, L. Fan, T. Baldacchini, J. Silvain, and Y. Lu, *Front. Optoelectron.*, **8** (2015) 351.
4. R. Kankala, K. Zhu, J. Li, C. Wang, S. Wang, and A. Chen, *Biofabrication*, **9** (2017) 032002.
5. F. Sima, J. Xu, D. Wu, and K. Sugioka, *Micromachines*, **8** (2017) 40.
6. A. Do, B. Khorsand, S. Geary, and A. Salem, *Adv. Healthcare Mater.*, **4** (2015) 1742.
7. M. Mehregany, S. Bart, L. Tavrow, J. Lang, and S. Senturia, *J. Vac. Sci. Technol. A*, **8** (1990) 3614.
8. S. Matsui, T. Kaito, J. Fujita, M. Komuro, K. Kanda, and Y. Haruyama, *J. Vac. Sci. Technol.*

B, **18** (2000) 3181.

9. S. Kawata, H. Sun, T. Tanaka, and K. Takada, *Nature*, **412** (2001) 667.
10. X. Cheng, X. Huang, J. Guo, S. Pang, and A. Yee, *J. Vac. Sci. Technol. B*, **20** (2002) 2881.
11. M. Tormen, L. Businaro, M. Altissimo, F. Romanato, S. Cabrini, F. Perennes, R. Proietti, H. Sun, S. Kawata, and E. Fabrizio, *Microelectronic Engineering*, **73–74** (2004) 535.
12. H. Sato, T. Kakinuma, J. Sang Go, and S. Shoji, *Sensors and Actuators A*, **111** (2004) 87.
13. K. Sun, T. Wei, B. Ahn, J. Seo, S. Dillon, and J. Lewis, *Adv. Mater.,* **25** (2013) 4539.
14. H. Koops, J. Kretz, M. Rudolph, M. Weber, and G. Lee, *Jpn. J. Appl. Phys.,* **33** (1994) 7099.
15. J. Wnuk, S. Rosenberg, J. Gorham, W. Dorp, C. Hagen, and D. Fairbrother, *Surface Science*, **605** (2011) 257.
16. D. Naik, T. Ezawa, R. Singh, Y. Miyamoto, and M. Takeda, *Optics Exp.*, **20** (2012) 19662.
17. X. Wang, J. Xu, H. Su, Z. Zeng, Y. Chen, H. Wang, Y. Pang, and W. Tam, *Appl. Phys. Lett.*, **82** (2011) 2212.
18. N. Ueda, M. Sasago, H. Kikuta, H. Kawata, and Y. Hirai, *J. Vac. Sci. Technol. B*, **32** (2014) 06F702.
19. T. Tanaka, H. Kikuta, H. Kawata, M. Yasuda, and M. Sasago, Y. Hirai, *Microelectronic Engineering*, **158** (2016) 85.
20. T. Tanaka, D. Sugihara, M. Sasago, H. Kikuta, H. Kawata, and Y. Hirai, *J. Vac. Sci. Technol. B*, **35** (2017) 06G308.
21. A. Misaka, D. Sugihara, K. Sato, M. Sasago, and Y. Hirai, *J. Photopolym. Sci. Technol.*, **32** (2019) 345.

Journal of Photopolymer Science and Technology
Volume 34, Number 2 (2021) 127－132 ©2021SPST

Impact of Water Treatment Reactor using TiO_2-coated Micropillar Made by UV-NIL

Kazuki Daigo[1], Ryota Akama[1], Noriyuki Unno[2], Shin-ichi Satake[1], and Jun Taniguchi[1*]

[1] Department of Applied Electronics, Tokyo University of Science,
6-3-1 Niijuku, Katsushika-ku, Tokyo 125-8585, Japan
[2] Department of Mechanical Engineering, Sanyo-Onoda City University,
Daigakudo-ri 1-1-1, Sanyo-Onoda, Yamaguchi 756-0884, Japan
**junt@te.noda.tus.ac.jp*

Increasing the catalyst surface area is effective for enhancing the photocatalysis effect. To understand the impact of increasing the surface area, micropillar patterns were fabricated using ultraviolet (UV) nanoimprint lithography (UV-NIL). A titanium oxide (TiO_2) layer was coated in a micropillar pattern by dip coating and this was used in a water treatment reactor. Photocatalytic decontamination was investigated using methylene blue (MB) aqueous solution. Changes in concentration of MB were observed during UV exposure to TiO_2 in the MB aqueous solution. As a result, the reaction rate of the 50 μm diameter pillar pattern was accelerated; therefore, increasing the surface area is effective for photocatalysis using TiO_2. On the other hand, the reaction rate of an 18.8 μm diameter pillar pattern was smaller than that of a flat surface because of a certain level of water-shedding effect.

Keywords: Photocatalysis, Micro-pillar, Water-treatment reactors, UV-NIL

1. Introduction

Recently, environmental cleanup technology using titanium oxide (TiO_2) photocatalysis has attracted attention [1]. In particular, there have been significant advances in the field of water cleanup [2] that uses TiO_2-coated reactors. The cleanup method for water is as follows. First, a TiO_2-coated reactor is prepared. Then, polluted water, including bacteria such as legionella and salmonella, is allowed to flow into the reactor. Simultaneously, the transparent reactor is subjected to ultraviolet (UV) light from the outside. When the reactor is exposed to UV light, the TiO_2 coating reacts with the polluted water, and detoxification by photocatalysis takes place. To obtain effective photocatalysis, enlargement of the surface area [3–5] and UV transparent materials [6,7] are important. In our previous study, MEXFLON beads were coated with TiO_2 and these were used as reactors. MEXFLON is a fluorinated polymer material and its refractive index is the same as that of water (n=1.33). This reactor obtained 3.8 times more photocatalytic reaction than a glass beads reactor [8]. This means that the MEXFLON beads did not interrupt UV light in water, because the refractive index of MEXFLON matches that of water and therefore suppresses UV light scattering and reflection between water and MEXFLON bead surfaces, and improves the exposure to UV light. Enlargement of the surface area is a candidate method for obtaining more efficient photocatalysis. In this study, to increase the surface area, micro-pillar structures were fabricated on a MEXFLON substrate by UV nanoimprint lithography (UV-NIL). The merit of UV-NIL is development less process, so production speed of UV-NIL is faster than that of photolithography. Using the patterned substrates for the reactor, the reactor performance was evaluated based on the concentration of methylene blue (MB) in solution. MB is a blue pigment and is used as a reagent for photocatalysis reactions, as described in the ISO method 10678 [9].

2. Experimental setup

2.1. Fabrication of micro-pillar pattern

Micropillar patterns were transferred using UV-NIL. The fabrication procedure was as follows: First, a master pillar-shaped mold was fabricated using photolithography. Then, a replica mold was

---

Received March 31, 2021
Accepted April 6, 2021

transferred from the master mold using UV-NIL. The replica mold shape was a hole pattern. Using this replica mold, pillar patterns were transferred to a MEXFLON substrate by UV-NIL.

The fabrication process of the master mold is illustrated in Fig. 1.

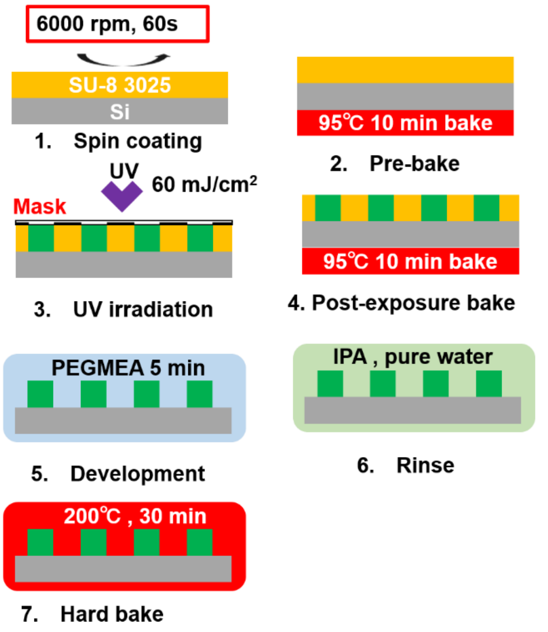

Fig. 1. Fabrication process of the master mold.

Photoresist (SU-8 3025, Nippon Kayaku Co., Ltd.) was dropped onto a silicon substrate and spin-coated at 6000 rpm for 60 s (Fig. 1(1)). After spin coating, SU-8 was pre-baked at 95 °C for 10 min (Fig. 1(2)). Two photomask patterns were prepared. One was a regular array with a 20 μm diameter circle and a 40 μm pitch, and the other was a regular array with a 50 μm diameter circle and a 100 μm pitch. These photomasks were covered with SU-8, and UV light was applied at 60 mJ/cm² (Fig. 1(3)). After UV exposure, post-exposure baking (PEB) was carried out at 95 °C for 10 min (Fig. 1(4)). After PEB, development was carried out by immersing in propylene glycol monomethyl ether acetate (PEGMEA) for 5 min (Fig. 1(5)). After development, the pillar-patterned sample was rinsed with isopropyl alcohol (IPA) and water (Fig. 1(6)). Finally, the pillar-patterned sample was baked at 200 °C for 30 min (Fig. 1(7)) to produce a pillar-shaped master mold. The fabricated master mold was release coated using 1 wt% Optool DSX (Daikin Co., Ltd.), which is a fluorinated release agent.

The fabrication process of the replica mold is illustrated in Fig. 2. SU-8 3025 was dropped onto the master mold (Fig.2(1)). Then, a polyester film (Cosmoshine A4300; Toyobo Co. Ltd.) covered the SU-8. The sample was then pressed at 6.5 MPa for 5 min to fill the mold with SU-8 resin (Fig. 2(2)). UV light was applied at 60 mJ/cm² while maintaining the pressure, to cure the resin (Fig. 2(3)). The sample was then baked at 95 °C for 10 min (Fig. 2(4)). Finally, the replica mold was released from the master mold (Fig. 2(5)). The photoresist SU-8 was used as a UV-curable resin, and the pattern shapes were hole patterns. This replica mold was also release coated using 1 wt% Optool DSX.

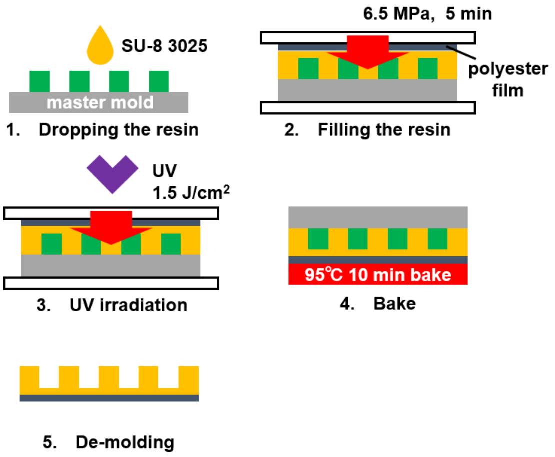

Fig. 2. Fabrication process of the replica mold.

The fabrication process of the micro-pillar pattern is shown in Fig. 3.

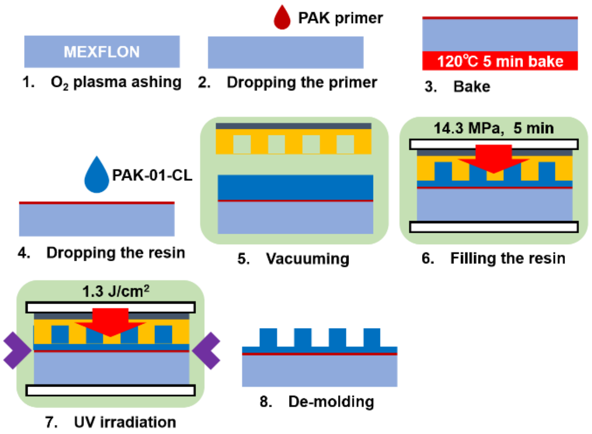

Fig. 3. Fabrication process of micro-pillar pattern.

Micropillar patterns were fabricated on MEXFLON substrate, which is composed of a fluorinated polymer, so the adhesion force is weak for UV-curable resins. Therefore, pre-treatment is necessary. First, oxygen plasma ashing was carried out for 45 s to make the MEXFLON surface hydrophilic (Fig. 3(1)). Next, the primer for PAK-01-CL (Toyo Gosei Co., Ltd.) was dropped on and coated (Fig. 3(2)). The sample was then baked at

120 °C for 5 min (Fig. 3(3)). This process is a pre-treatment to improve the adhesion of UV-curable resin. PAK-01-CL was used for pillar patterning because of the high fidelity and stability of the TiO_2 dip coating process. PAK-01-CL was dropped onto the pre-treated MEXFLON substrate (Fig. 3(4)). In the case of the microscale hole pattern replica mold, air bubbles are included in the transfer pattern. In this case, therefore, UV-NIL was carried out in a vacuum environment. The coated MEXFLON and replica mold were installed in a vacuum chamber and evacuated to less than 0.1 Pa by a dry pump (Fig. 3(5)). After that, a pressure of 14.3 MPa was applied for 5 min to fill the mold with resin (Fig. 3(6)). Next, UV light was applied at a dose of 1.3 J/cm^2 while maintaining the pressure. In this case, UV LED light was exposed from the side direction because the top and bottom plates were opaque materials (Fig. 3(7)). After ventilation, the replica mold was released, and micropillar patterns were fabricated on the MEXFLON substrate (Fig. 3(8)).

2.2. Photocatalyst coating method

The TiO_2 photocatalyst was coated on the patterned surface by dip coating. TKC-303 (Tayca Co., Ltd.) was used as the TiO_2 coating liquid material. The coating process is shown in Fig. 4.

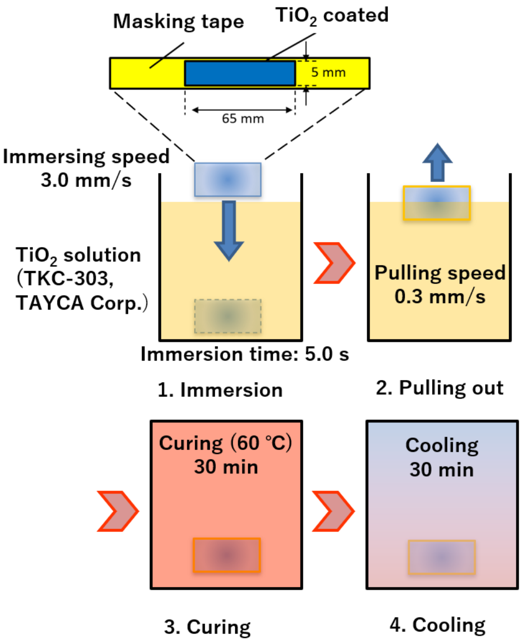

Fig. 4. Dip coating method of TiO_2 photocatalyst.

To define the TiO_2 coated area, masking tape was used. The TiO_2-coated micropillar pattern area was 5 mm × 65 mm. This sample was then immersed in a TiO_2 solution (TKC-303) for 5 s (Fig. 4(1)). Next, the sample was removed at a speed of 0.3 mm/s (Fig. 4(2)). After removal, the sample was cured at 60 °C for 30 min in an electrical furnace (Fig. 4(3)). Finally, the sample was cooled for 30 min at room temperature (Fig. 4(4)). Water absorption occurs in the cured UV-curable resin. To prevent this, the TiO_2 coating is necessary.

2.3. Water treatment reactor set-up

A reactor was constructed for treatment of polluted water, as shown in Fig. 5.

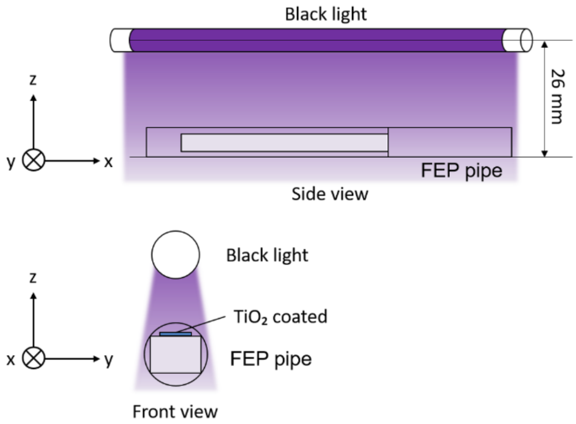

Fig. 5. Diagram of water treatment reactor using TiO_2-coated micropillar pattern.

This reactor consists of a fluorinated ethylene propylene (FEP) pipe containing the TiO_2 surface immersed in polluted water, which is exposed to UV light. A 1 ppm MB aqueous solution was used to represent polluted water. The MB aqueous solution flowed into the FEP pipe and reacted with the TiO_2-coated micropillar structure set inside the FEP pipe. FEP has high transparency for UV light and a high chemical stability. These properties are required in this experiment. The inner diameter of the FEP pipe was 10 mm, and its length was 150 mm. Black light (FL6BLB, Toshiba Lighting & Technology, Co., Ltd.) was used as the UV light source and placed 26 mm away from the FEP pipe. The main wavelength of the black light was 352 nm and the intensity of the black light was 6.4 μW/cm^2. To clean the polluted water (MB aqueous solution), UV light was applied to the TiO_2-coated micropillar pattern through the FEP pipe. A photocatalytic reaction occurs at the TiO_2 surface, and the concentration of MB is reduced. The entire system is illustrated in Fig. 6. A reservoir with a stirrer, turbine flowmeter (FT200-016-PP, Japan Flow Controls Co., Ltd.), reactor, and magnetic pump (MD-15R-N, Iwaki Co., Ltd.) are arranged in series using a silicone tube. The MB aqueous solution was impounded in the reservoir and circulated inside the silicone tube and reactor using the magnetic pump. The flow rate was 0.42 L/min and the temperature was maintained at 20 °C using a chiller (NCB-1200P, Tokyo Rikakikai Co., Ltd.). The temperature inside the reservoir was measured using a thermocouple. Before the start of UV irradiation, circulation of the MB aqueous solution was carried out for 1 h to stabilize the system.

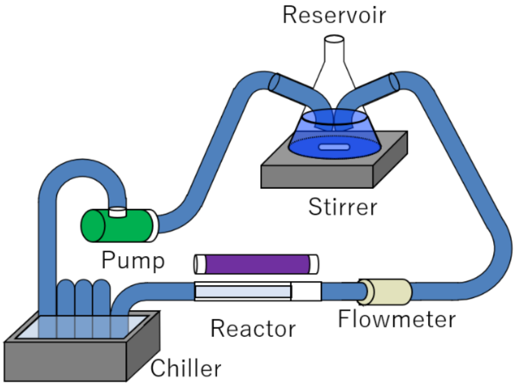

Fig. 6. Water treatment reactor system.

2.4. Evaluation methods

Micropillar patterns were observed using a scanning electron microscope (SEM; ERA-8800FE Elionix Co., Ltd.). To confirm the photocatalytic effect, water contact angles were measured with a contact angle (CA) meter (Drop Master 700, Kyowa Interface Science, Co., Ltd.). The concentration of MB was determined by measuring the absorbance at 665 nm, which is the maximum absorbance wavelength of MB. The absorbance was evaluated using the Lambert-Beer law. The absorbance measurement method was as follows: A small amount of MB aqueous solution was removed from the reservoir and a halogen lamp (LA-100USW, Hayashi Watch-works, Co., Ltd.) light was shone through the MB aqueous solution. The transmitted light was measured using a multichannel spectroscope (PMA-12 C10027-01., Hamamatsu Photonics K.K.). In this equipment, the absorbance wavelength of 665 nm was monitored. Quantitative evaluation of the photocatalysis reaction requires a reaction model. In this study, the Langmuir-Hinshelwood kinetics model was used [10]. This model is well known to be representative of photocatalytic reactions. Usually, this model deals with the decomposition of gases [11–15], but it is also applicable to the decomposition of MB in water [16–20]. In this study, the reaction rate was calculated using the Langmuir-Hinshelwood kinetics model. The details are given in Ref. [10].

3. Results and discussion

3.1 Observation of transferred micropillar pattern

SEM images of a regular array with a 50 μm diameter circle and 100 μm pitch master mold, replica mold, and micropillar pattern on the MEXFLON substrate are shown in Fig. 7. The master mold has a diameter of 50 μm and a pitch of 101.9 μm, which corresponds to the photomask design (Fig. 7(a)). The height of the pillars is 24.0 μm (Fig.7(b)). The replica mold has a diameter of 50.0 μm and a depth of 21.9 μm (Fig. 7(c)). The micropillar pattern was transferred using a PAK-01-CL on a MEXFLON substrate by UV-NIL. The pillar pattern has a diameter of 50 μm and a height of 18.7 μm. In this case, the residual PAK layer is 36.7 μm (Fig. 7(d)). The pillar diameter did not change, but the pillar height was reduced because of shrinkage of the photocurable resin (PAK-01-CL). Shrinkage was mostly in the vertical direction. Despite this pillar height shrinkage, micropillar patterns were successfully transferred by the UV-NIL process. The obtained micropillar patterns had a diameter of 50.0 μm, a pitch of 101.9 μm and a height of 18.7 μm (pillar pattern A). SEM images of a regular array with a 20 μm diameter circle and 40 μm pitch master mold, replica mold, and micropillar pattern are shown in Fig. 8. The master mold has a diameter of 19.9 μm and a pitch of 40.1 μm (Fig. 8(a)). The height of the pillars is 18.7 μm (Fig. 8(b)). The replica mold has a diameter of 18.8 μm and a depth of 18.4 μm (Fig. 8(c)). The pillar pattern has a diameter of 18.8 μm and a height of 18.1 μm. In this case, the residual PAK layer is 30.2 μm (Fig. 8(d)). In this case, shrinkage occurred during the

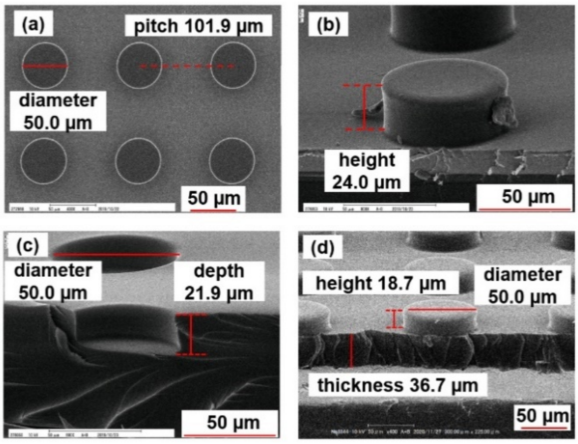

Fig. 7. SEM images of master mold, replica mold and micropillar pattern on MEXFLON. (a) Top view of master mold. (b) Tilted angle view of master mold. (c) Cross-sectional view of replica mold. (d) Cross-sectional view of micropillar pattern on MEXFLON.

fabrication process of the replica mold (see Fig. 2), and SU-8 was mainly reduced by the UV-NIL process. Although the pillar diameter was reduced by 1.2 μm, the micropillar pattern surface was successfully transferred by the UV-NIL process. The obtained micropillar patterns had a diameter of 18.8 μm, a pitch of 40.1 μm and a height of 18.1 μm (pillar pattern B).

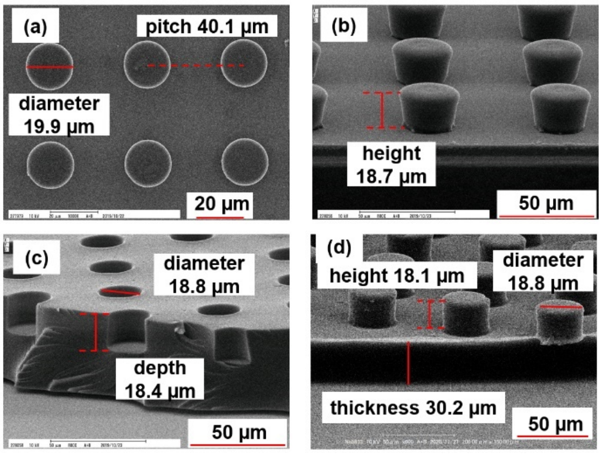

Fig. 8. SEM images of master mold, replica mold and micropillar pattern on MEXFLON. (a) Top view of master mold. (b) Tilted angle view of master mold. (c) Cross-sectional view of replica mold. (d) Cross-sectional view of micropillar pattern on MEXFLON.

3.2 Confirmation of photocatalytic effect of TiO_2-coated micropillar pattern

One pillar pattern A (sample 1) and two pillar patterns B (samples 2 and 3) were coated with TiO_2 by the dipping method (see section 2.2). Flat plates with/without TiO_2 were prepared for comparison (sample 4). Their fabrication method is the same as Fig. 3, but a non-patterned replica mold (flat film) was used. The thickness of the TiO_2 layer was 100 nm, as measured using a surface profilometer on a flat plate. To confirm the photocatalytic effect, the TiO_2 was exposed to UV light for 10 min. Subsequently, water contact angles (CAs) were measured for each surface. The volume of the water droplets was 20 μL. The measurement results are presented in Table 1.

Table 1. Contact angle before UV irradiation and after UV irradiation of each sample

Sample No.	Without TiO_2 CA [°]	With TiO_2 CA [°]	With TiO_2 and UV CA [°]
1	97.5	36.6	19.8
2	120.6	45.9	28.3
3	121.5	48.2	20.5
4	90.3	90.6	83.0

As shown in Table 1, sample 1 (50 μm diameter pillar pattern) had a lower CA than samples 2 and 3 (18.8 μm diameter pillar pattern). This result shows that samples 2 and 3 have hydrophobic properties, such as a lotus effect. In fact, without TiO_2 coating, all samples were hydrophobic (CA >90°), and samples 2 and 3 had higher CA values. Micropillar patterns (sample 1,2,3) were smaller CA than flat plate after UV irradiation, so enlargement of surface area is effective to reduce CA values.

3.3 Water cleaning using water treatment reactor

Figure 9 shows the degradation of MB by photocatalysis. The concentration of MB was measured at 1 h intervals. The y-axis of Fig. 9 is normalized concentration, i.e., the concentration divided by the initial concentration (A/A_0).

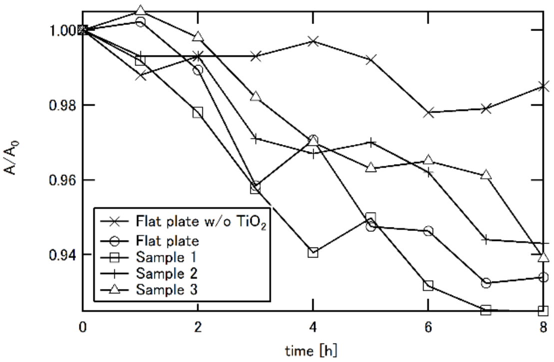

Fig. 9. MB concentration changes for each sample.

As shown in Fig. 9, the flat plate without TiO_2 shows no change because decomposition of the MB did not occur. The MB concentration of the TiO_2-coated samples was reduced, and the reduction rate of sample 1 was faster than that of samples 2 and 3. This trend is similar to that of the CA trend. Using Fig. 9 data, reaction rates were calculated using the Langmuir-Hinshelwood kinetics model (see section 2.4), and the results are summarized in Table 2. For comparison, the surface areas are also listed.

Table 2. Summary of reaction rate and surface area

	Picth [μm]	Diameter [μm]	Height [μm]	Surface area [mm^2]	Reaction rate
Flat plate without TiO_2	-	-	-	325	2.6×10^{-3}
Flat plate	-	-	-		9.5×10^{-3}
Sample1	101.9	50	18.7	416.9	12.2×10^{-3}
Sample2	40.1	18.8	18.1	541.1	6.8×10^{-3}
Sample3	40.1	18.8	18.1		6.3×10^{-3}

As shown in Table 2, sample 1 (50 μm diameter pillar pattern) had the highest reaction rate. This means that sample 1 is the most effective for treatment of water pollution. Although samples 2 and 3 (18.8 μm diameter pillar pattern) had the largest surface area, their reaction rates were lower than that of the flat plate with TiO_2. The reasons for this are as follows. Samples 2 and 3 had larger CAs than sample 1, even with UV irradiation, indicating that this surface has low wettability (see Table 1). Thus, we assume that a certain level of water-shedding effect occurred in samples 2 and 3. These results suggest that both surface area and water wettability are important for enhancing the reaction rate. To compare flat plate, sample 2 and 3 had lower CAs, so wettability was more effective than flat plate for static water droplet. However, this reactor was circulated, so dynamic wettability for water is different to CAs trend. We assume that water flow does not reach at bottom of smaller micropillar patterns, this generates loss of reaction surface area. These results suggest that optimize of micropillar pattern shape is important. In this study, sample 1 (50 μm diameter pillar pattern) is the best for circulated water treatment reactor. In order to improve the cleaning efficiency of the photocatalyst, one of the solutions is to put a large number of TiO_2-coated micropillar plates in the reactor. This is the future work.

4. Conclusion

In this study, the impact of a water treatment reactor using a TiO_2-coated micropillar made by UV-NIL was investigated. Using UV-NIL, micropillar patterns with diameters of 50.0 and 18.8 μm were obtained at 6 mm × 65 mm area. After fabricating the pillar pattern, the TiO_2 coating and photocatalysis effects were evaluated in MB aqueous solution, with MB representing a pollutant. The reaction rate with the 50 μm diameter pillar pattern was higher than that of the flat plate, so increasing the surface area is effective for enhancing the photocatalytic effect.

Acknowledgement

This study was supported by KAKENHI 26420158 and 19K04224.

References

1. A. Fujishima and K. Honda, *Nature*, **238** (1972) 37.
2. N. J. Peill and M. R. Hoffmann, *Environ. Sci. Technol.*, **29**(12) (1995) 2974.
3. T. Ochiai, K. Masuko, S. Tago, R. Nakano, K. Nakata, M. Hara, Y. Nojima, T. Suzuki, M. Ikekita, Y. Morito, and A. Fujishima, *Water*, **5**(3) (2013) 1101.
4. F. Denny, J. Scott, V. Pareek, G. D. Peng, and R. Amal, *Chem. Eng. Sci.*, **64**(8) (2009) 1695.
5. M. Mehrvar, W. A. Anderson, and M. Moo-Young, *Adv. Environ. Res.*, **6**(4) (2002) 411.
6. H. Shiraishi, S. Fukinbara, K. Imai, and K. Nakano, *CELSS J.*, **9** (1996) 19-25.
7. H. Taoda, *Chemical Industry*, **54** (2003) 197.
8. M. Kuniyasu, N. Unno, S. Satake, K. Yuki, and Y. Seki, *J. Photochem. Photobiol. A.*, **338** (2017) 8.
9. A. Mills, C. Hill, and P. K. J. Robertson, *J. Photochem. Photobiol. A*, **237**, (2012) 7.
10. D. F. Ollis and C. Turchi, *Environ. Prog. Sustain. Energy*, **9** (1990) 229.
11. M. Hunger, G. Hu¨sken, and H. J. H. Brouwers, *Cem. Concr. Res.*, **40** (2010) 313.
12. X. Wang, X. Tan, and T. Yu, *Ind. Eng. Chem. Res.*, **53** (2017) 7902.
13. A. A. Assadi, A. Bouzaza, and D. Wolbert, *J. Photochem. Photobiol. A*, **236** (2012) 61.
14. E. Lim, K. Yamamoto, E. Sumiyoshi, T. Yamaguchi, and K. Itou. *Soc. Heat. Air-Conditioning and Sanit. Eng. Japan*, **40** (224) (2015) 19.
15. E. Sumiyoshi, T. Yamaguchi, K. Itou, and K. Yamamoto, *Soc. Heat. Air-Conditioning and Sanit. Eng. Japan*, **41**(229) (2016) 35.
16. A. Houas, H. Lachheb, M. Ksibi, E. Elaloui, C. Guillard, and J.-M. Herrmann, *Appl. Catal. B: Environ.*, **31**(2) (2001) 145.
17. C. Sahoo, A. K. Gupta, and I. M. S. Pillai, *J. Environ. Sci. Health, Part A*, **47**(10) (2012) 1428.
18. C. Xu, G. P. Rangaiah, and X. S. Zhao, *Ind. Eng. Chem. Res.*, **53**(38) (2014) 14641.
19. A. H Jawad, N. Shazwani A. Mubarak, M. A. M. Ishak, K. Ismail, and W. I. Nawawi, *J. Taibah Univ. Sci.*, **10**(3) (2016) 352.
20. W. Vallejo, C. Di´az-Uribe, and K. Rios, *Adv. Phys. Chem.*, **2017** (2017) 6358601.

Journal of Photopolymer Science and Technology
Volume 34, Number 2 (2021) 133－138 ©2021SPST

Fabrication of Moth-eye Antireflective Nanostructures via Oxygen Ion-beam Etching on a UV-curable Polymer

Takao Okabe[1]*, Katsuyuki Yatagawa[1], Kazuki Fujiwara[1], and Jun Taniguchi[1]

[1] *Department of Applied Electronics, Faculty of Advanced Engineering,*
Tokyo University of Science, 6-3-1 Niijuku, Katsushika-ku, Tokyo 125-8585,
Japan
**okabe@te.noda.tus.ac.jp*

We report a low-cost, high-throughput process for fabricating a moth-eye-like anti-reflector on a curved surface. First, a curved surface was made from a UV-curable resin via UV imprinting. Then, the moth-eye-like structures were formed directly on the polymer surface via oxygen ion-beam etching. This produced flexible, transparent, and curved polymer products with anti-reflective properties. The method avoids duplication, which is generally needed for conventional anti-reflector fabrication. We compared the anti-reflective performance both flat and curved lenses before and after etching. The reflectance after etching for 150 s was substantially 10% lower than that of the non-etched surface. The usefulness of this method for polymer optical products with anti-reflective properties was demonstrated.

Keywords: Anti-reflection, Moth-eye, Nanostructures, UV nanoimprinting, Ion-beam etching

1. Introduction

Moth-eye-like structures are well known anti-reflectors (ARs), which have applications in devices such as solar cells [1], liquid crystal displays [2,3], and optical lenses [4-6]. Their nanostructure mimics that of a moth's eye, which has many nanoscale bumps on its surface, allowing it to gather light with high efficiency. To satisfy the increasing demand for AR devices, better methods to fabricate such nano-scale structures are required.

One of a most popular methods for moth-eye fabrication is a combination of etching (dry or wet) and nanoimprint lithography (NIL). In the etching process, moth-eye-like structures are formed on a hard material, such as silicon [2], metal [3,4], carbon [7-9], or a ceramic [10]. In this process, masking is sometimes used to make regularly arranged patterns. For example, Ji *et al*. reported a particle-masking method ('colloidal lithography') that uses a particle monolayer as a mask [11, 12]. Processes that do not need masking have also been reported, whereby the moth-eye-like nanostructures are etched on glassy carbon using an oxygen ion beam [7-9].

After etching, several NIL processes using a soft and flexible resin are needed to copy the etched moth-eye shape to the target devices or to additional NIL molds, as schematically shown in Fig. 1(a) [8, 13-15]. This is because it is difficult and costly to make smooth curved surfaces, such as lenses and roll-to-roll molds, directly on hard materials. Although these processes can be used to fabricate practical moth-eyes with low reflectance [7-9, 16, 17], cheaper and higher-throughput methods are needed, particularly for AR applications in portable camera devices [18-20].

To meet the aforementioned demands, we propose a method to fabricate moth-eye-like nanostructures directly on a photo-curable polymer via oxygen ion-beam etching. Figure 1(b) shows the proposed method, which consist of two steps: UV imprinting and etching. First, a curved surface was fabricated

---

Received March 26, 2021
Accepted April 24, 2021

using a UV-curable resin. The cured resin was then directly etched by the ion beam to form the moth-eye-like nanostructure. The use of a UV curable resin makes this process is both low-cost and high-throughput. Another advantage of the process is that there is no need for duplication of the structure onto a flexible and transparent polymer. This also lowers the cost and increases the throughput.

In this study, we formed moth-eye nanostructures on a UV-curable resin on flat and curved (concave and convex) surfaces and investigated their AR performance. In addition, AR etching on an UV-NIL-duplicated lens array was demonstrated.

2. Experimental

2.1. Materials

The moth-eye-like structures were made using a UV-curable resin. The resin consisted of a monomer (2,2-bis(4-glycidyloxyphenyl)propane; Tokyo Chemical Industry Co., Ltd., Tokyo, Japan), and a photo-acid generator (PAG) (CPI-100P; San-Apro Ltd., Tokyo, Japan) as the photopolymerization initiator; the chemical structures are shown in Fig. 2(a) and (b), respectively. PAG (0.01 g) was directly mixed into the monomer (0.5 g) in a hot-water bath (85 °C) with ultrasonic mixing for 10 minutes. This mixture produced a UV-curable resin by cationic ring-opening polymerization of the epoxy functional groups [21, 22].

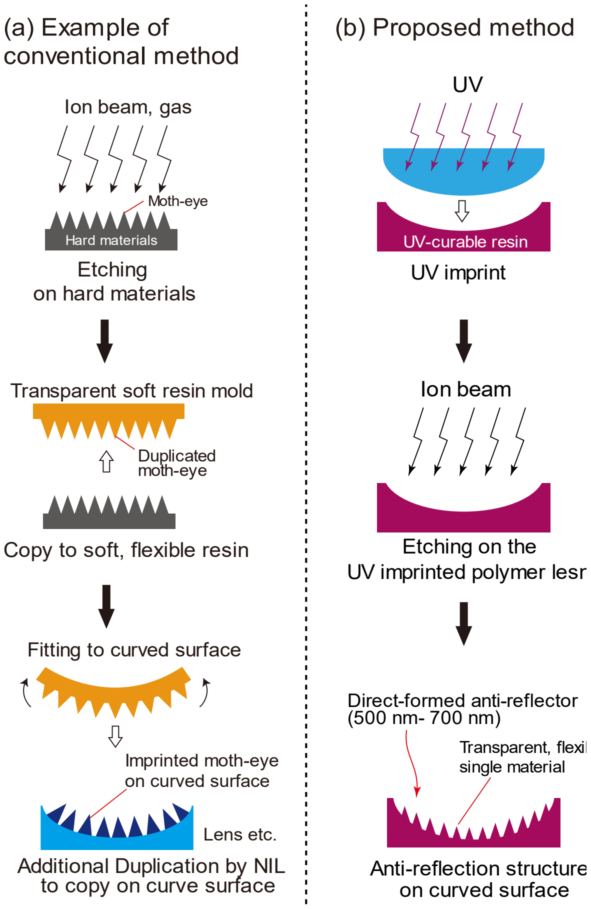

Fig. 1. Comparison of the conventional and proposed moth-eye fabrication methods. (a) Conventional method, which involves etching the moth-eye structure onto hard materials, and then duplicating this to a soft, transparent, and flexible resin replica mold. (b) Proposed method to form moth-eye structures directly onto UV-curable polymers via oxygen ion-beam etching.

2.2. Processes

Our process produces moth-eye-like structures on a UV-cured polymer surface in two-step process: UV lithography (e.g. UV-NIL) and oxygen ion-beam etching. The fabrication process is schematically shown in Fig. 3a and 3b for flat and curved surfaces, respectively.

For the flat surface, the UV-curable resin droplet was first dropped onto a cut Si wafer substrate (15 mm × 15 mm) and spin-coated with a rotational speed of 3000 rpm (Fig. 3(a-1)). We note that we coated the Si wafer substrate with hexamethyldisilazane (HMDS) (Tokyo Chemical Industry Co., Ltd., Tokyo, Japan) to improve the adhesion between the Si substrate and the resin layer. The HMDS-coated-substrate was baked on a hot plate at 120 °C for 20 minutes. After baking, the substrate was washed with acetone. The spin-coated resin layer was then cured with a UV lamp (Aicure UP-50; Panasonic Co., Osaka, Japan) with a UV dose and peak wavelength of 60 mJ/cm^2 and 365 nm, respectively (Fig. 3(a-2)). The cured layer was etched using an oxygen ion beam produced by an inductively coupled-plasma (ICP) etching machine (EIS-700; ELIONIX Inc., Tokyo, Japan) with a power and oxygen flow rate of 500 W and 3.5 sccm, respectively (Fig. 3(a-3). The distance from the beam gun to the workpiece was 110 mm. Three different etching times were used (90, 120, and 150 s). Finally

(a) Momomer

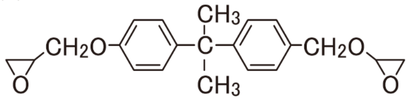

(b) PAG

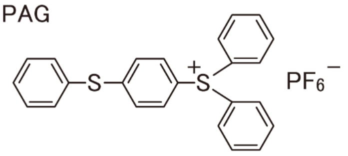

Fig. 2. Materials used for the UV-curable resin: (a) monomer; (b) photopolymerization initiator.

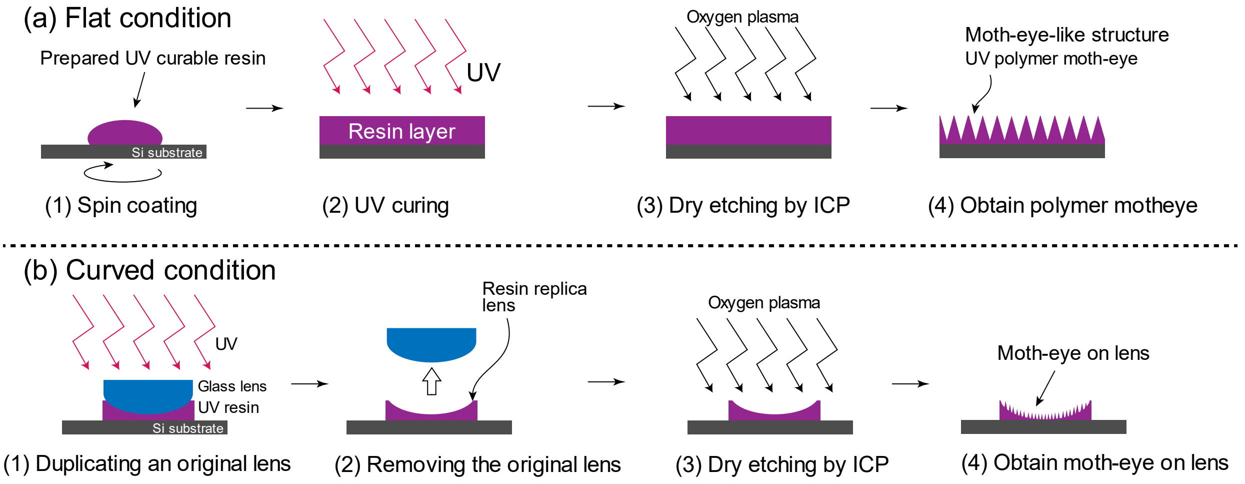

Fig. 3. Fabrication process of moth-eye structures on a UV-cured polymer using ICP etching. (a) Flat surface: (a-1) spin coating of the resin on a Si substrate; (a-2) UV curing; (a-3) oxygen plasma etching by ICP without masking; and (a-4) the moth-eye structure obtained on the polymer surface. (b) Curved surface: (b-1) duplication of the original lens by UV curing; (b-2) removal of the original lens; (a-3) oxygen plasma etching onto the duplicated concave lens without masking; and (b-4) the moth-eye structure obtained on the surface of the concave lens.

(Fig. 3(a-4)), a layer with moth-eye-like structures was obtained on the flat substrate.

To form the structures on a curved surface, we fabricated a concave lens duplicated from a convex lens mold. As depicted in Fig. 3(b-1), the UV resin was first UV imprinted to form the duplicated lens. The resin lens was duplicated on a Si wafer substrate for easy handling. The UV light was irradiated through the transparent glass lens mold with a UV dose of 60 mJ/cm^2. A release agent was coated of the surface of the lens mold by first dipping the lens into a 1.0% OPTOOL DSX (DAIKIN Industries, Ltd., Osaka, Japan) solution for 3 hours and baking on a hot plate at 100 °C for 15 minutes. After baking, the lens mold was washed in NOVEC7300 (3M Company, Minnesota, USA) to remove contamination. Owing to the release coating, the lens mold was released smoothly from the UV cured resin, and a concave resin lens was obtained. Next, the duplicated concave resin lens was etched with the oxygen ion beam under the same etching conditions as described above (Fig. 3(b-3)). Finally, the moth-eye-like structure was obtained directly on the concave resin lens (Fig. 3(b-4)). Each sample was observed using a scanning electron microscope (SEM; ERA8800FE, ELIONIX Inc., Tokyo, Japan) and its reflectance was measured using a spectrophotometer (Solidspec-3700; Shimadzu Corp., Kyoto, Japan).

3. Results and discussion

3.1. Flat surface

An SEM image of the etched layer on a flat-polished Si substrate for an etching time of 120 s is shown in Fig. 4. The moth-eye structure was formed on the UV-cured polymer layer, which had a thickness of 44.7 µm, as seen in Fig. 4(a). Pillar structures, as shown in Fig. 4(b), covered the surface of the 20 mm × 20 mm polymer layer. The average pillar height, diameter, and pitch were 700, 300, and 100 nm, respectively. Thus, this single etching process can produce high-aspect-ratio moth-eye-like nanostructures. The shape and height of the structures were almost same as those formed on glassy carbon.

We measured the reflectance from the flat surface. Figure 5 shows the reflectance ratio before and after etching for etching times of 90, 120, and 150 s. Figure 5(a) and (b) show the reflectance for initial layer thicknesses (i.e. before etching) of 26 (condition A) and 92 µm (condition B), respectively. The reflectance decreased with etching time for both conditions, reaching 7% after 150 s. Thus, the oxygen ion beam effectively produced antireflective structures onto the UV-cured polymer layer. Figure 5(c) shows the relationship between the etching time and average reflectance in conditions A and B. For each etching time, the decrease in reflectance was similar for both conditions. On the basis of these results, we suggest that the height of the moth-eye-like structure was independent of the initial thickness. Therefore, it is possible to add an anti-reflection structure to films of any thickness.

3.2. Curved surface

Next, we fabricated moth-eye-like structures on concave and convex polymer lenses, which were

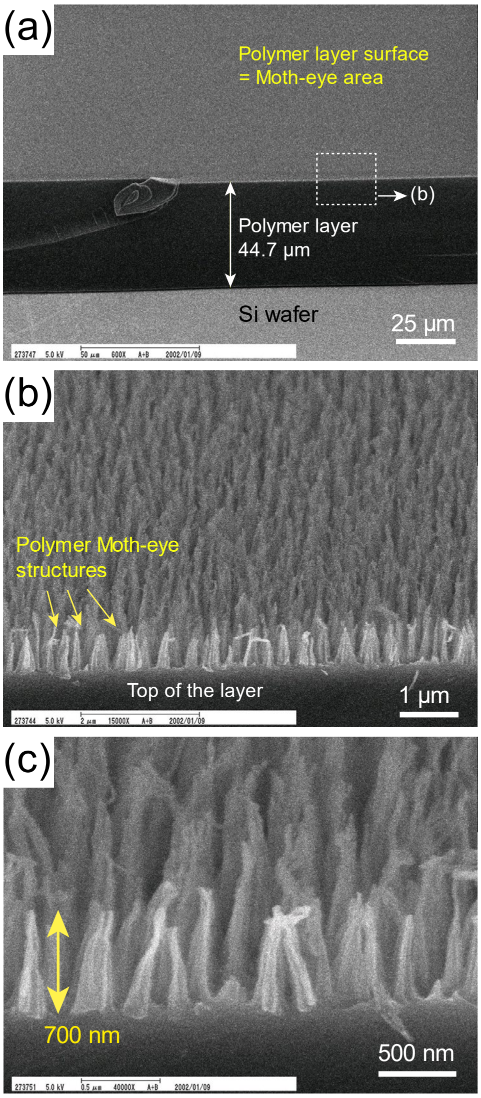

Fig. 4. Cross-sectional SEM images of the moth-eye-like nanostructure on a flat surface. (a) Etched UV-cured polymer layer. (b) Pillar structures on the polymer layer. (c) Higher-magnification image of the pillars, from which the average height and pitch were measured to be 200 and 700 nm, respectively.

duplicated by UV imprinting from original glass lenses, as schematically shown in Fig. 3(b). Figure 6a and 6b show SEM images of the etched concave and convex lenses, respectively. In this demonstration, the concave lens was shaped on a substrate and the convex lens was shaped as a stand-alone-lens. In each sample, bumpy structures were formed over the entire surface. The pitch of the structure was wider than that created on the flat surface. The height of the nanostructures on both the concave and convex lenses was 700 nm. However, the width of the nanostructures was smaller on the convex lens than on the concave lens. In summary, moth-eye-like structures formed on the UV-imprinted replica lenses.

The reflectance was measured for both etched lenses with the method described above for the flat surface. Figure 7a and 7b show the reflectance of the concave and convex lenses, respectively; the reflectance from the non-etched lenses is shown for comparison. For both lenses, the reflectance decreased after etching, although the extent of the reduction was much greater for the concave lens. This demonstrates that AR nanostructures could be etched in a single step using the oxygen ion beam. On the basis of these results, we expect that our method will improve future manufacturing processes for AR lenses and their molds.

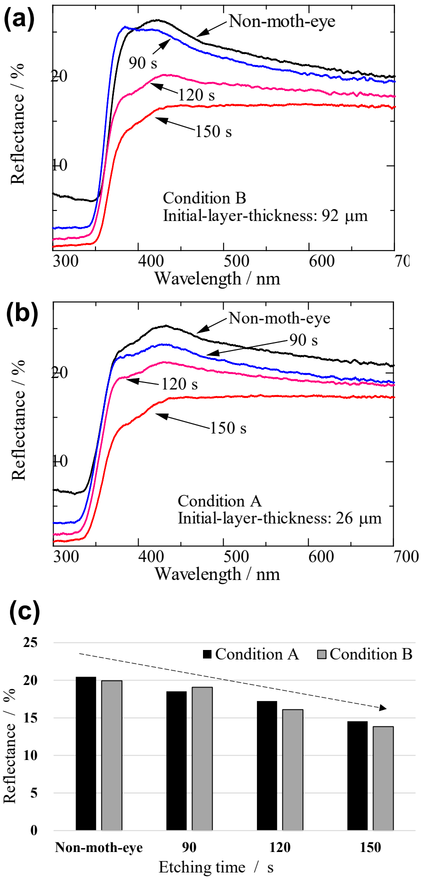

Fig. 5. Reflectance of the etched surfaces for etching times of 90, 120, and 150 s for initial thicknesses of (a) 26 μm (condition A) and (b) 92 μm (condition B). (c) Comparison of the reflectance for conditions A and B for each etching time.

3.3. Etching onto a microlens array

Finally, we formed a moth-eye-like structure on a UV-imprinted lens array. The process involved first UV-imprinting a lens array on a primer coated Si wafer with a UV dose of 60 mJ/cm^2. The convex

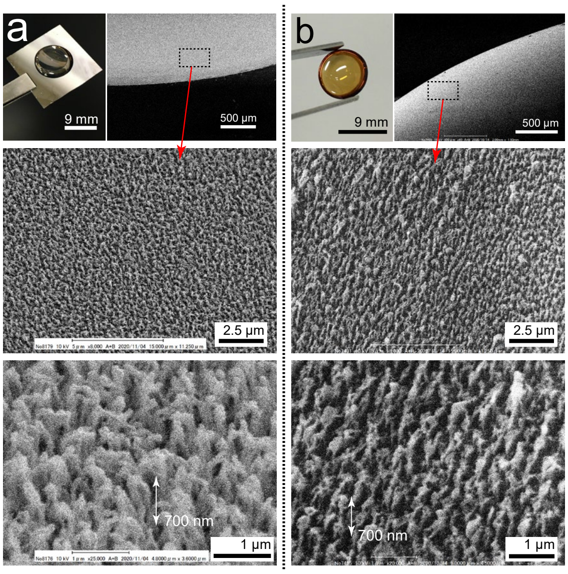

Fig. 6. SEM images of the moth-eye-like nanostructures etched on (a) concave and (b) convex polymer lenses shaped by UV imprinting.

(a) Curve condition: Concave lens

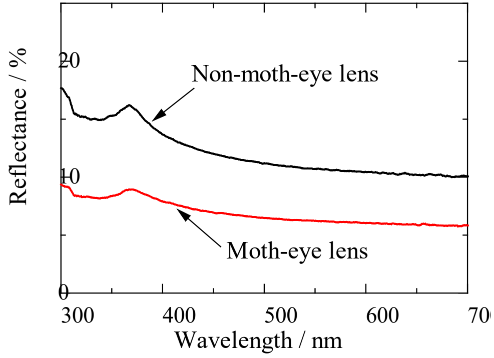

(b) Curve condition: Convex lens

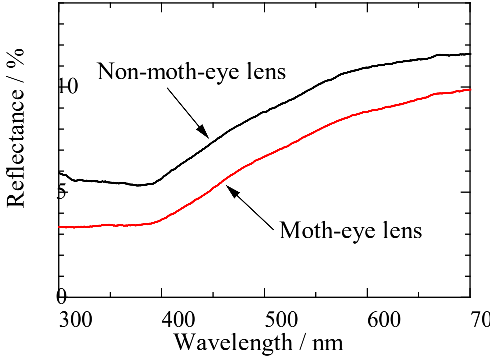

Fig. 7. Comparison of reflectance of the moth-eye-etched and non-etched (a) concave and (b) convex lenses.

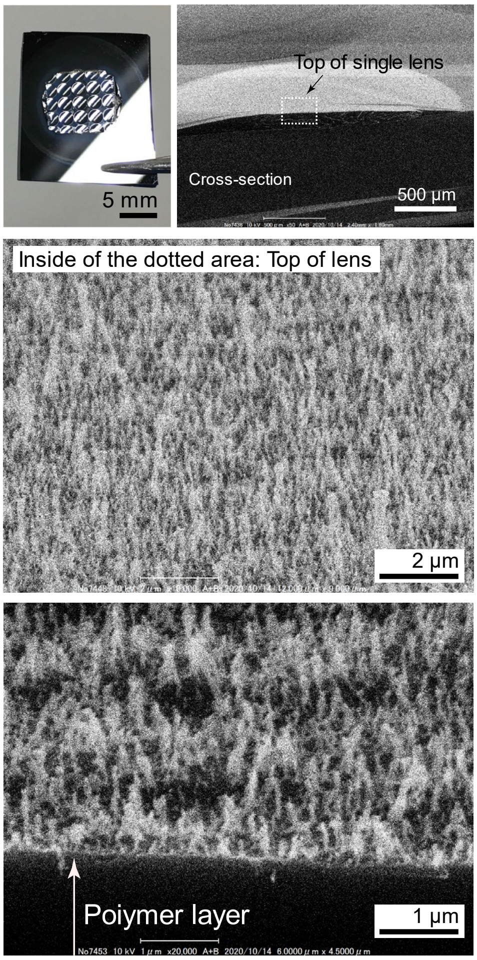

Fig. 8. Photograph and SEM images of the moth-eye-like nanostructures formed on a UV-imprinted convex microlens array.

lens array was imprinted from a glass convex master mold. As shown in Fig. 8, the moth-eye-like nanostructure formed over the entire lens array with an average pillar height of approximately 700 nm. Thus, our method can even create moth-eye-like structures by etching on regular patterns formed by UV-NIL. We expect that this method will be used to fabricate moth-eye structures on microscale patterns using NIL

4. Conclusion

In this paper, we proposed a simple method to fabricate moth-eye-like AR nanostructures via oxygen ion-beam etching directly onto a UV-curable polymer. The moth-eye-like nanostructures had a high aspect ratio and an average height of 700 nm. For both flat and curved lenses, the reflectance was substantially reduced after etching, demonstrating the potential of these surfaces for AR applications. We also formed moth-eye-like structures on a UV-imprinted lens array. The method can make moth-eye-like nanostructures on patterns formed by the UV-NIL process. In summary, our method allows the low-cost production of polymer lenses with AR functions and their NIL molds.

References

1. S. M. Kang, S. Jang, J. K. Lee, J. Yoon, D. E. Yoo, J. W. Lee, M. Choi, and N. G. Park, *Small*, **12** (2016) 2443.
2. G. Tan, J. H. Lee, Y. H. Lan, M. K. Wei, L. H. Peng, I. C. Cheng, and S. T. Wu, *Optica*, **4** (2017) 2334.
3. Y. Uozu, *J. Photopolym. Sci. Technol.*, **32** (2019) 291.
4. S. S. Oha, C. G. Choi, and Y. S. Kim, *Microelectron. Eng*., **87** (2010) 2328.
5. S. Xie, X. Wan, B. Yang, W. Zhang, X. Wei, and S. Zhuang, *Nanomaterials*, **9** (2019) 747.
6. P. B. Clapham and M. C. Hutley, *Nature*, **244** (1973) 281.
7. T. Yano, H. Sugawara, and J. Taniguchi, *Microelectron. Eng*., **9** (2020) 100077.
8. I. Mano, T. Uchida, and J. Taniguchi, *Microelectron. Eng*., **191** (2018) 97.
9. H. Eto, S. Hiwasa, and J. Taniguchi, *J. Photopolym. Sci. Technol*., **30** (2017) 533.
10. T. Yanagishita, T. Kondo, and H. Masuda, *J. Vac. Sci. Technol. B*, **36** (2018) 031802.
11. S. Ji, J. Park and H. Lim, *Nanoscale*, **4** (2012) 4603.
12. S. Ji, K. Song, T. B. Nguyen, N. Kim, and H. Lim, *ACS Appl. Mater. Interfaces*, **5** (2013) 10731.
13. M. R. Lotz, C. R. Petersen, C. Markos, O. Bang, M. H. Jakobsen, and R. Taboryski, *Optica*, **5** (2018) 557.
14. T. Senn, O. Kutz, C. Weniger, J. Li, M. Schoengen, H. Lochel, J. Wolf, P. Gottert, and B. Lochel, *J. Vac. Sci. Technol. B,* **29** (2011) 061601.
15. J. W. Leem, X. Y. Guan, M. Choi, and J. S. Yu, *Sol. Energ. Mat. Sol. C*, **134** (2015) 45.
16. S. Ju, J. Y. Choi, D. Chae, H. Lim, H. Kang, and H. Lee, *Nanotechnology*, **31** (2020) 505301.
17. J. S. Choi, J. H. An, J. K. Lee, J. Y. Lee, and S. M. Kang, *Polymers*, **12** (2020) 296.
18. C. Zhang, P. Yi, L. Peng, X. Lai, and J. Ni, *IEEE Trans. Nanobioscience*, **14** (2015) 1127.
19. Q. Chen, G. Hubbard, P. A. Shields, C. Liu, D. W. E. Allsopp, W. N. Wang, and S. Abbott, *Appl. Phys. Lett*., **94** (2009) 263118.
20. I. N. Baena, A. J. Martín, J. J. Hernández, J. R. C. Smirnov, F. Viela, M. A. Monclús, M. R. Osorio, J. M. M. Aldareguia, and I. Rodríguez, *Nanoscale*, **10** (2018) 15496.
21. X. Ning and H. Ishida, *Polym. Sci. A Polym. Chem*. **32** (1994) 1121.
22. G. Liu, X. Zhu, B. Xu, X. Qian, G. Song, and J. Nie, *Appl. Polym. Sci*. **130** (2013) 3698.

Journal of Photopolymer Science and Technology
Volume 34, Number 2 (2021) 139−144 ©2021SPST

Molecular Dynamics Simulation of the Resist Filling Process in UV-nanoimprint Lithography

Hiroki Uchida[1], Ryosuke Imoto[1], Tadashi Ando[1*], Takao Okabe[1], and Jun Taniguchi[1]

[1] Department of Applied Electronics, Faculty of Advanced Engineering,
Tokyo University of Science, 6-3-1 Niijuku, Katsushika-ku, Tokyo 125-8585, Japan
**tando@rs.tus.ac.jp*

The selection and design of appropriate resist materials is indispensable for a successful nanoimprint lithography (NIL) technique. Currently, the pattern resolution of NIL is below 10 nm. Therefore, atomic-scale analysis of the NIL process is required for further development in this field. In this study, we performed all-atom molecular dynamics (MD) simulations of the filling process of resist molecules in ultraviolet NIL (UV-NIL). To simulate the filling process, silicon molds with different trench widths (1, 2, and 3 nm) were pressed into different resist materials composed of two or four molecular species with different viscosities (viscosity range 4 to 5,566 mPa·s) under constant pressure (100 atm). In the MD simulations, resists with viscosities lower than 10 mPa·s were successfully filled into the 3-nm wide trench. Lowering the resist viscosity shortened the time required for complete filling. In the resist consisting of four molecular species, the 1-nm-wide trench was preferentially filled by the lower-viscosity molecules; consequently, the resist molecules were non-uniformly distributed in the system. This inhomogeneity would lead to defects after the UV curing process. The MD simulations also showed that when mixed with small resist molecules, the multi-functional resist molecules can more easily enter a narrow cavity, which is advantageous for fabricating high-resolution patterns by UV-NIL. The molecular behaviors during the filling process observed in the MD simulations provide useful information for the future design of defect-free resists.

Keywords: Nanoimprint lithography, Molecular dynamics simulation, Viscosity of resist

1. Introduction

Nanoimprint lithography (NIL) is a promising technology for fabricating nano-scale patterns at low-cost with high throughput. Using compression molding, NIL creates a pattern in a thin resist carried on a substrate [1, 2]. In 2012, Li et al. demonstrated the transfer of 4-nm-wide half-pitch lines into a resist using NIL combined with high-resolution helium ion beam patterning [3]. When the pattering size is below 10 nm, the molecular properties of the resist molecules and the atomistic interactions between the resist and the mold significantly affect the resolution and defect formation in NIL. Therefore, atomic-scale analysis of the NIL process is essential for further development in this field. Molecular dynamics (MD) simulation is a powerful tool for investigating the molecular behavior of materials at the atomic level. The effects of resist polymer size on the resist filling process in thermal NIL (T-NIL) have been well studied in MD simulations [4-7]. Adhesion between the mold and the resist polymer in the T-NIL process has also been simulated by MD methods [8-10]. In contrast, the behaviors of the resist molecules during the filling process of ultraviolet NIL (UV-NIL) are not well understood. To fill this knowledge gap, we performed MD simulations of the UV-NIL filling process using four different resist materials with viscosities ranging from 4 to 5,566 mPa·s, and investigated how the macroscopic viscosity of the resist affects its filling behavior.

Received March 24, 2021
Accepted April 28, 2021

2. Simulation model and methods

2.1. Resist models

Table 1 lists the molecular constituents, viscosities, and numbers of acryloyl or vinyl groups in the resist materials. Fig. 1 shows the molecular structures, and Table 2 gives the compositions and experimentally measured viscosities of the four resists.

Table 1. Viscosities and numbers of acryloyl or vinyl groups of the resist molecules used in this study

Molecule	Viscosity[a] [mPa·s]	Functional groups
NVP (N-Vinyl pyrrolidone)	2.07[b]	one vinyl group
HDDA (Hexane-1,6-diyl diacrylate)	4	two acryloyl groups
TPGDA (Tripropylene glycol diacrylate)	10	two acryloyl groups
TMPTA (Trimethylolpropane triacrtlate)	92	three acryloyl groups
DPHA (Dipentaerythritol hexaacrylate)	5,702	six acryloyl groups
DMPA(2,2-Dimethoxy-2-phenylacetophenone)[c]	—	—

[a] Value at room temperature.
[b] From PubChem (PubChem CID: 6917).
[c] DMPA is a polymerization initiator, which is solid at room temperature.

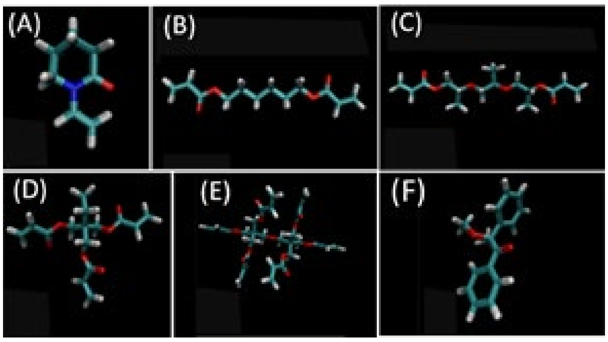

Fig. 1. Structures of molecules in the resist material used in this study: (A) NVP, (B) HDDA, (C) TPGDA, (D) TMPTA, (E) DPHA, and (F) DMPA (see Table 1 for descriptions). Figures were generated by VMD [11].

Table 2. Compositions and measured viscosities of the four resist materials examined in this study

	Composition (w/w%)	Viscosity [mPa·s]
Resist I	HDDA (96%), DMPA (4%)	4
Resist II[a]	TMPTA (10%), TPGDA (57%), NVP (29%), DMPA (4%)	8
Resist III	TMPTA (96%), DMPA (4%)	95
Resist IV	DPHA (96%), DMPA (4%)	5,566

[a] From Ref. [12]

2.2. Simulation systems and methods

Fig. 2 is a schematic of the simulation system used in this study.

The mold and substrate were made of silicon (Si), which has a diamond unit cell with a lattice constant of 5.43 Å. The trench width was varied as 1.09, 2.17, and 3.26 nm. A general Amber force field (GAFF) [13] and an Austin Model 1 with bond charge correction [14, 15] were used for the force field parameters and atomic charges of the resist molecules, respectively. The bonds and bond angles consisting of neighboring Si atoms were restrained by harmonic potentials with universal force field (UFF) parameters [16]. The Lennard–Jones parameters of the Si atoms were adopted from Ref. [17] and the interactions between the Si atoms and resist molecules were handled by Lorentz-Berthelot combination rules [18].

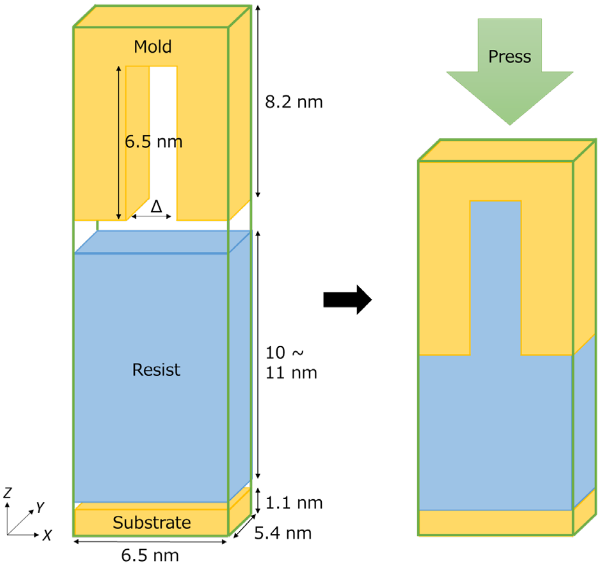

Fig. 2. Schematic of the simulation system. The trench width Δ was set to 1.09, 2.17, or 3.26 nm. The simulation box is drawn with green lines.

In all MD simulations, periodic boundary conditions were imposed in all directions. Van der Waals and short-range electrostatic interactions were cut off at 12 Å and the long-range electrostatic interactions were computed with the particle-mesh Ewald summation method [19]. The time step was 2 fs and all bonds containing hydrogen were constrained by the SHAKE algorithm [20]. The temperature was controlled by a Langevin thermostat [21] with a collision frequency of 1.0 ps^{-1}. The pressure was controlled by a Berendsen barostat [22] with a pressure relaxation time of 1.0 ps.

The resists were prepared as follows: 1) The resist molecules were randomly placed in a box of fixed size (x = 6.5 nm, y = 5.4 nm) without significant overlaps. The number of molecules was calculated based on the weight ratios listed in Table 2 (second column); 2) The system was minimized by the steepest descent method for the first 1000 steps and by the conjugate gradient method for the subsequent 1000 steps; 3) MD simulations were performed at 298 K and 1 atm until the system was well equilibrated. The pressure was controlled only along the *z*-direction (as mentioned above, the dimensions along the *x*- and *y*-axes were fixed).

When simulating the filling process, the prepared resist was placed between the mold and the substrate, and the MD simulation was run at 298 K and 100 atm along the *z*-axis.

The use of periodic boundary condition in *z*-direction would introduce unwanted dipole-dipole inter-layer interactions. However, the surfaces between resist layers are separated by several nanometers. A 2.8-nm-width Si layer exists between the resist layers even in the complete filling states. Additionally, the resist molecules are randomly arranged in the resist layer with various conformations. Therefore, effects of the inter-layer interactions along the

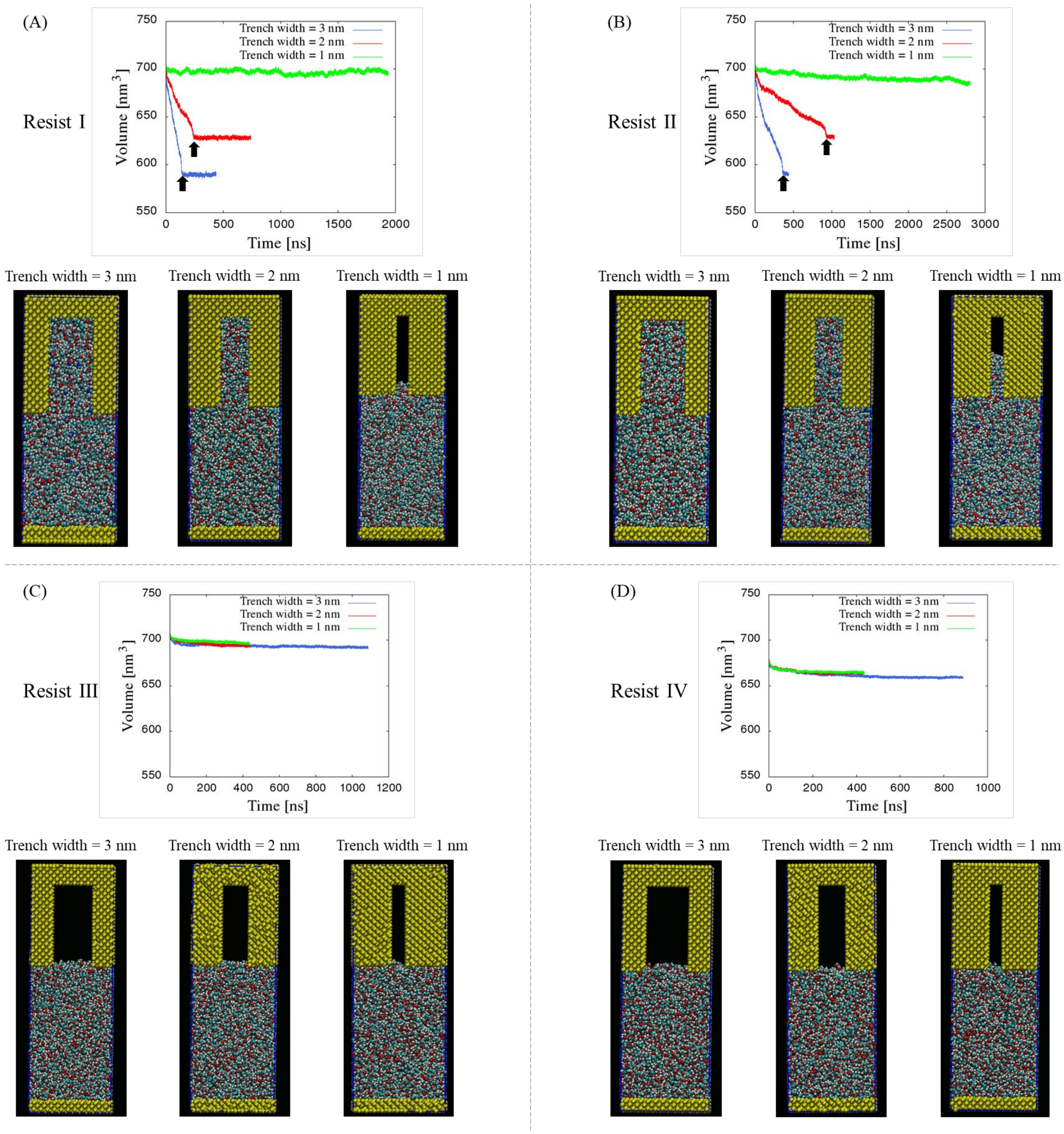

Fig. 3. Time evolutions of the simulation volumes and the system configurations with various trench widths at the end of the simulation: (A) resist I, (B) resist Ⅱ, (C) resist Ⅲ, and (D) resist Ⅳ. In panels A and B, the arrows on the graphs indicate the times and volumes at which the fillings were completed in the MD simulations. Graphics of the simulation systems were generated by VMD [11].

z-direction would be negligible in the simulation systems used in this study.

All MD simulations and analyses were performed using the Amber16 and AmberTools16 packages [23, 24]. The MD program code was slightly modified to introduce the pressure control along the *z*-axis while fixing the *x*- and *y*-dimensions.

3. Results and discussion

3.1. Filling behaviors

Long-time MD simulations were conducted in 12 systems (combinations of the four resist materials and three trench widths). Fig. 3 plots the system volumes as functions of simulation time and the configurations of the various systems at the end of the simulation.

Resist I (Fig. 3A) completely filled the 3- and 2-nm-wide trenches in the Si mold within ~150 ns and ~250 ns, respectively. In the 1-nm-wide trench, the system volume fluctuated around its initial value throughout the MD simulation (1.8 μs) and the trench was not filled.

Resist II (Fig. 3B) filled the 3- and 2-nm-wide trenches within ~350 ns and ~950 ns, respectively. These longer filling times (2–4 times longer than those of resist I) reflect the different viscosities of the resists: resist II was twice as viscous as resist I (see Table 2). In the simulation of resist II filling the 1-nm-wide trench, the system volume gradually decreased during the 2.8-μs simulation time and the top of resist II in the trench reached approximately half the trench height. Interestingly, the viscosity of resist II was higher than that of resist I but resist I could not fill the 1-nm-wide trench. The filling process will be discussed in detail later.

In the simulations of resists III and IV (Fig. 3C and D), the viscosities were higher than 90 mPa·s, and the volumes of the systems remained almost constant regardless of trench width. The resist molecules did not fill the trenches, even when the width was extended to 3 nm. It has been reported that high-viscosity resists cannot easily penetrate nano-level patterns [25]. Previously, we investigated the filling of 100 micro-scale patterns with high-viscosity resists (2,900 and 13,090 mPa·s). The pattern filling required high pressures (of the order of megapascals) and long filling times (over one minute) [26]. Therefore, the under-filling of the 3-nm wide trenches in the microsecond time range of the present MD simulations is consistent with the actual behavior of the resist.

3.2. Distribution of molecules after the filling

Next, we examined the individual distributions of the four molecular species in resist II after complete filling. In general, high-viscosity molecules are bulky, multi-armed, and multi-functional (see Table 1 and Fig. 1). Such molecules increase the hardness and curing speed after UV exposure [27-29]. Therefore, to ensure a defect-free filling, the resist molecules in the resist layer and cavities must be uniformly distributed.

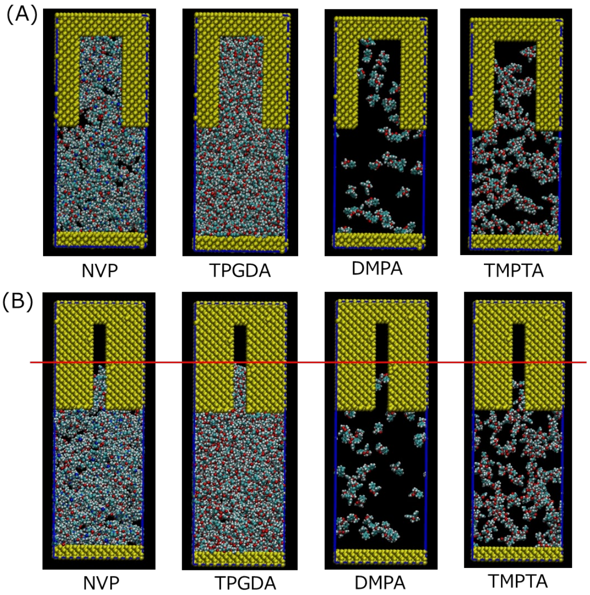

Fig. 4. Distributions of the four molecular species constituting resist II in the trenches with widths of (A) 3 nm and (B) 1 nm at the end of the simulation. In B, the red line indicates the top of the resist in the trench.

Fig. 4A shows the distributions of NVP, TPGDA, DMPA, and TMPTA at the end of the simulation in the 3-mm-wide trench. All types of molecules within the resist layer were almost equally distributed on the substrate and inside the trench. The molecular species in resist II were also uniformly distributed in the 2-mm-wide trench (data not shown). However, in the system with the 1-mm-wide trench, NVP and TPGDA more easily entered the trench than TMPTA (see Fig. 4B). In fact, TMPTA entered the trench to approximately half the entry height of NVP and TPGDA during the 2.8-μs filling process. The viscosities of NVP, TPGDA, and TMPTA are 2, 10, and 92 mPa·s, respectively (see Table 1). Therefore, even when the molecules are well mixed in the resist layer, the low-viscosity molecules would preferentially enter the narrow cavity in the UV-NIL filling process. This preference results in an inhomogeneous distribution of the resist II molecules, and subsequent defects after UV curing.

Fig. 5 shows the configurations of TMPTA in resist II at various times of the simulation in the 1-nm-wide trench. In the initial state, the TMPTA molecules were equally distributed and dispersed within the resist II layer on the substrate (Fig. 5, left panel). As the filling process proceeded, TMPTA accumulated near the entrance of the cavity, while NVP and TPGDA passed into the trench (Fig. 5, middle panel). Later, TMPTA gradually entered the trench (Fig. 5, right panel). This retardation of TMPTA filling at the entrance can be attributed to the three-armed bulky structure of this molecule (see Table 1 and Fig. 1). Interestingly, TMPTA completely entered the 2-nm-wide trench in resist II (Fig. 3B), but could not enter the 3-nm wide trench in resist III (see Fig. 3C). This result suggests that mixing high-viscosity molecules with low-viscosity molecules facilitates the filling of a narrow cavity with high-viscosity molecules. One can reasonably suppose that the small resist molecules surround the multi-functional large molecules, preventing the formation of multimeric complexes of the large resist molecules. Therefore, mixing low-viscosity and high-viscosity molecules is an effective strategy for high-resolution, defect-free pattern transfer in UV-NIL.

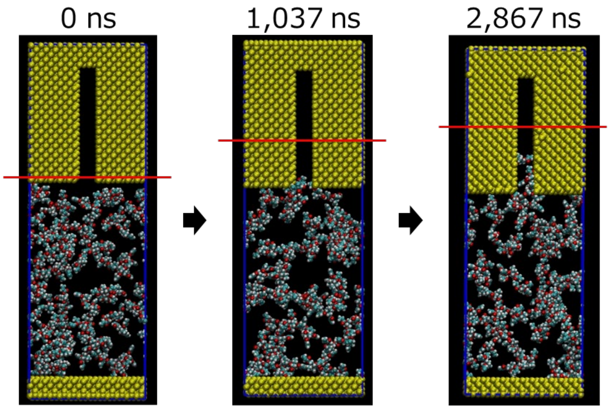

Fig. 5. Configurations of TMPTA in resist II in the 1-nm-wide trench at various times of the simulation. The red line indicates the top of the NVP or TPGDA molecules in each snapshot.

4. Conclusion

We performed all-atom MD simulations of the filling process in UV-NIL using four different types of resist materials. In the simulations, molds with line patterns were pressed into the resists under constant pressure. The trenches of the molds with trench widths of 3 and 2 nm were successfully filled with the low-viscosity resists (<10 mPa·s), and the filling speed decreased with increasing viscosity of the resist. Conversely, the resists with viscosities exceeding 90 mPa·s did not fill the trenches. These results are consistent with empirical rules obtained from experiments. In the resist consisting of four molecular species, the lower-viscosity molecules preferentially entered the 1-nm-wide trench, so the resist molecules were non-uniformly distributed in the trench. This material would develop defects after the UV curing process. The MD simulations also suggested that mixing multi-functional and bulky resist molecules with small resist molecules facilitates the entry of the large molecules into a narrow cavity, which could be advantageous for high-resolution patterns in UV-NIL. The molecular behaviors during the filling process found in this computational study provide useful information for the future design of defect-free resists.

Acknowledgement

This work was supported by JSPS KAKENHI Grant Numbers JP19K04224. The authors would like to thank Dr. Ohsaki Takeshi at Toyo Gosei Co., Ltd for viscosity measurements of resist materials.

References

1. S. Y. Chou, P. R. Krauss, and P. J. Renstrom, *Appl. Phys. Lett.*, **67**, (1995) 3114.
2. S. Y. Chou, P. R. Krauss, and P. J. Renstrom, *Science*, **272**, (1996) 85.
3. W. D. Li, W. Wu, and R. S. Williams, *J. Vac. Sci. Technol. B*, **30**, (2012).
4. Y. S. Woo, D. E. Lee, and W. I. Lee, *Tribol. Lett.*, **36**, (2009) 209.
5. A. Taga, M. Yasuda, H. Kawata, and Y. Hirai, *J. Vac. Sci. Technol. B*, **28**, (2010) C6m68.
6. M. Yasuda, K. Araki, A. Taga, A. Horiba, H. Kawata, and Y. Hirai, *Microelectron. Eng.*, **88**, (2011) 2188.
7. S. Kim, D. E. Lee, and W. I. Lee, *Tribol. Lett.*, **49**, (2013) 421.
8. J. H. Kang, K. S. Kim, and K. W. Kim, *Appl. Surf. Sci.*, **257**, (2010) 1562.
9. S. Kwon, Y. Lee, J. Park, and S. Im, *J. Mech. Sci. Tech.*, **25**, (2011) 2311.

10. S. Yang, S. Yu, and M. Cho, *Appl. Surf. Sci.*, **301**, (2014) 189.
11. W. Humphrey, A. Dalke, and K. Schulten, *J. Mol. Graph. Model.*, **14**, (1996) 33.
12. J. G. Kloosterboer, in *Advances in Polymer Science*, 1988, vol. 84, pp. 1.
13. J. Wang, R. M. Wolf, J. W. Caldwell, P. A. Kollman, and D. A. Case, *J. Comput. Chem.*, **25**, (2004) 1157.
14. A. Jakalian, B. L. Bush, D. B. Jack, and C. I. Bayly, *J. Comput. Chem.*, **21**, (2000) 132.
15. A. Jakalian, D. B. Jack, and C. I. Bayly, *J. Comput. Chem.*, **23**, (2002) 1623.
16. A. K. Rappe, C. J. Casewit, K. S. Colwell, W. A. Goddard, and W. M. Skiff, *J. Am. Chem. Soc.*, **114**, (1992) 10024.
17. G. P. Lithoxoos, J. Samios, and Y. Carissan, *J. Phy. Chem. C*, **112**, (2008) 16725.
18. H. A. Lorentz, *Annalen der Physik*, **248**, (1881) 127.
19. T. Darden, D. York, and L. Pedersen, *J. Chem. Phys.*, **98**, (1993) 10089.
20. J.-P. Ryckaert, G. Ciccotti, and H. J. C. Berendsen, *J. Comput. Phys.*, **23**, (1977) 327.
21. R. J. Loncharich, B. R. Brooks, and R. W. Pastor, *Biopolymers*, **32**, (1992) 523.
22. H. J. C. Berendsen, J. P. M. Postma, W. F. Vangunsteren, A. Dinola, and J. R. Haak, *J. Chem. Phys.*, **81**, (1984) 3684.
23. D. R. Roe and T. E. Cheatham, *J. Chem. Theory Comput.*, **9**, (2013) 3084.
24. D. A. Case, D. S. Cerutti, I. Cheatham, T.E., T. A. Darden, R. E. Duke, T. J. Giese, H. Gohlke, A. W. Goetz, D. Greene, N. Homeyer, S. Izadi, A. Kovalenko, T. S. Lee, S. LeGrand, P. Li, C. Lin, J. Liu, T. Luchko, R. Luo, D. Mermelstein, K. M. Merz, G. Monard, H. Nguyen, I. Omelyan, A. Onufriev, F. Pan, R. Qi, D. R. Roe, A. Roitberg, C. Sagui, C. L. Simmerling, W. M. Botello-Smith, J. Swails, R. C. Walker, J. Wang, R. M. Wolf, X. Wu, L. Xiao, Y. D. M., and P. A. Kollman, (2016) AMBER 2016, University of California, San Francisco.
25. L. J. Guo, *J. Phys. D*, **37**, (2004) R123.
26. H. Ueda and J. Taniguchi, *J. Photopolym. Sci. Technol.*, **31**, (2018) 283.
27. C. Decker, *Polym. Int.*, **45**, (1998) 133.
28. C. T. Ratnam and K. Zaman, *Nucl. Instrum. Methods. Phys. Res. B*, **152**, (1999) 335.
29. J. H. Choi and H. J. Kim, *J. Ind. Eng. Chem.*, **12**, (2006) 412.

Communication

Journal of Photopolymer Science and Technology
Volume 34, Number 2 (2021) 145－148 ©2021SPST

Proposal of hybrid deep learning systems for process and material design in thermal nanoimprint lithography

Sou Tsukamoto, Hidekatsu Tanabe, Ryuhei Yamamura, Kai Kameyama,
Hiroaki Kawata, Masaaki Yasuda, and Yoshihiko Hirai

Physics and Electronics Engineering, Graduate School of Engineering,
Osaka Prefecture University
1-1, Gakuencho, Nakaku, Sakai, Osaka 599-8531, Japan
**hirai@pe.oasakafu-u.ac.jp*

A hybrid smart process and material designing system for nanoimprint is proposed based on combination of deep learning system and numerical simulations. The system consists of deep learning system based on experimental data base and simulated table data base. The system complements the missing information with each other, and suggests better processes condition and/or materials. We demonstrate process and material design for low temperature nanoimprinting process using glycol contained polyvinyl alcohol.

Keywords: Nanoimprint, Polymer, Smart system, Neural network, Simulation, Process

1. Introduction

Nanoimprint lithography [1,2] realizes direct nanofabrication of a wide variety of materials. For example, organic semiconductors [3-5], low-melting-point glasses [6,7], and various materials [8] can be directly processed, and various applications such as electronics, photonics, and bio-devices have been approached.

In the field of conventional lithography, prediction of hot spots and correction of layout patterns to avoid defects are being carried out, where optimization of pattern layout is effective because highly standardized materials and equipment are good for deep-learning [9,10]. In nanoimprint lithography, few reports have been published to predict hot spots as well based on past experimental reports [11,12]. Nevertheless, no report has been seen for process and material proposals or designing for nanoimprint.

In thermal nanoimprinting, the processing conditions are determined by mechanical properties such as the viscoelastic modulus of the material and topological conditions such as the pattern width, pattern height, and pressure [13-16]. Therefore, the process conditions were set by simulation analysis or empirical knowledge based on the results of mechanical property measurement by rheometer and geometrical conditions [17].

On the other hand, one of the main features of nanoimprinting is to process customized materials according to each application. Therefore, process optimization including pattern layout based on characteristics of the material is required.

However, for materials with unknown properties or novel new processes, a series of preliminary experiments was necessary, which need huge time for measurement of material characteristics and optimization.

The purpose of this research is to propose a smart manufacturing system that can handle new processes or materials based on the experimental and simulation knowledge bases to provide the optimized nanoimprinting process for various materials and structures using artificial neural network systems [18-20].

In this study, we used multi-layered back propagation neural network (BPNN) system, which is one of the typical deep learning systems among machine learning systems for prediction of the nanoimprinted results, and suggestion of nanoimprinting processes and materials.

2. Low temperature direct nanoimprint for Polyvinyl Alcohol (PVA) with Glycerol added

The motivation for this study is to develop low

Received March 30, 2021
Accepted April 27, 2021

temperature direct nanoimprint process for PVA. PVA is a water-soluble resin and has great value for use as a disposable mold and sacrificial layer. However, it is known that the water solubility of PVA is impaired when heated above about 150℃. Therefore, in order to perform nanoimprinting using PVA, it is necessary to do so at the lowest possible temperature below 150℃.

To solve this problem, we newly discovered that the pressing temperature of PVA can be lowered by adding Glycerol to PVA. Figure 1 demonstrates direct nanoimprint to Glycerol added PVA. The effect of Glycerol additive is evidently revealed.

However, there is no way to know the optimal additive concentration of Glycerol, and many experiments are required to confirm the optimal conditions by successively changing the amount of Glycerol added and the process temperature. On the other hand, for simulation prediction, it is necessary to measure the unknown material parameters.

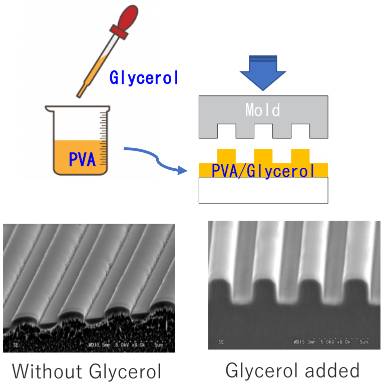

Without Glycerol

Glycerol added

Fig. 1. Direct nanoimprint results with and without Glycerol additive to PVA. (10MPa, 130°C, Line width=2.0μm)).

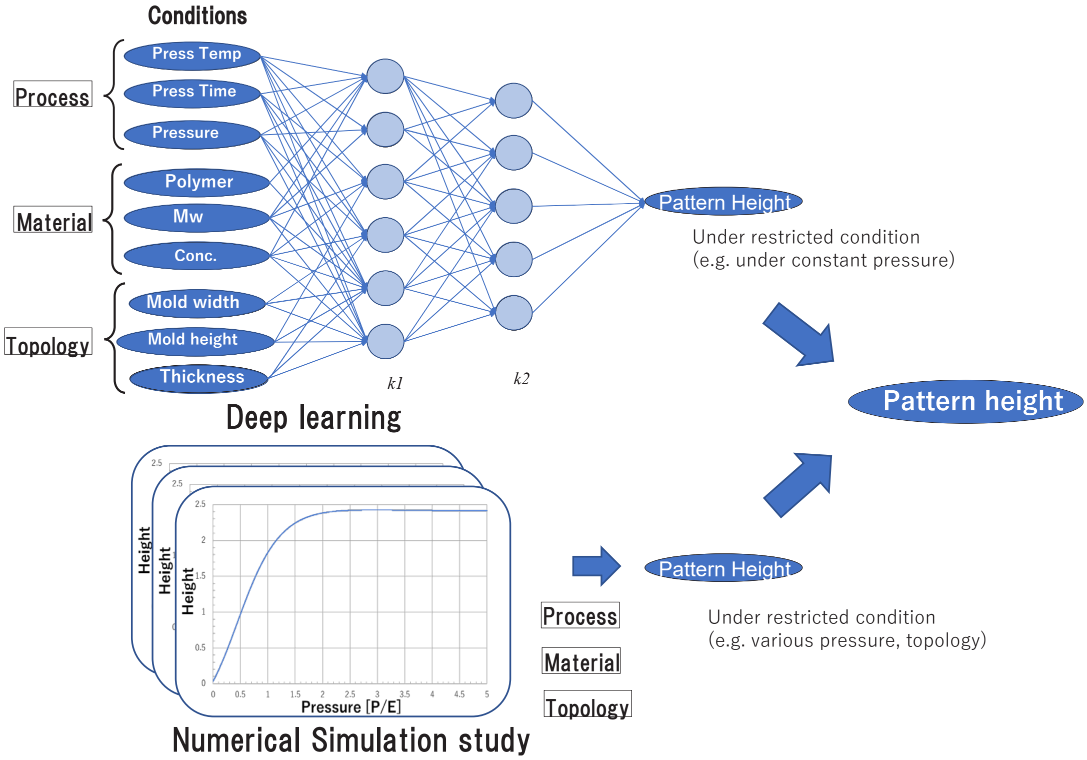

Fig. 2. Schematics of ‘hybrid’ deep learning system in combination with numerical simulation.

3. Hybrid deep learning

We propose a novel system that predicts the pattern height after thermal nanoimprint by complementing experimental learning and simulation under various conditions.

We use deep learning systems to predict pattern height for various process temperature and the glycol concentration under fixed imprinting pressure based on the experimental database. On the other hand, numerical simulation has done and the results are tabled to compensate the prediction of the deep learning results. Here, we assume the imprint results are approximately determined by the ratio of imprinted pressure various elastic modulus of material and topology of the mold pattern. Therefore, we need training experimental dates where only the glycol concentration is varied.

So, we call the proposed system as hybrid system in combination with deep learning and numerical simulation systems.

Figure 2 shows the schematics of the hybrid system. In the deep learning, we input the experimental results of the pattern height after nanoimprinting in various glycol concentration and pressing temperatures. The deep learning system consist of 2 hidden layers with 11 nodes for each, which was determined concerning prediction errors. Typical epochs for learning process were 5,000.

In this case, we predict the dependence of the pattern height on the glycol concentration and on the press temperature. However, the dependence on pressing pressure could not be predicted because the learning data is out of consideration.

On the other hand, simulation can calculate the dependence on the pattern shape, press temperature, press pressure, and elastic modulus of the material, but it could not handle the dependence on an unknown material with unknown physical parameters. However, the system is normalized system based on continuous mechanics and under the similarity rule, relative normalized pattern height could be derived from normalized pressure *P/E*, where *P* is pressing pressure and *E* is elastic modulus of polymer.

In other words, if the mechanical properties of the resins are relatively the same, then if we know the normalized pattern height, we can find the normalized relative press pressure. As a result, even if the modulus of elasticity of the material is unknown, the relative pressure can be estimated.

Furthermore, if we know the relative press pressure, we can predict the pattern height after nanoimprinting by the change in press pressure.

In this way, under a certain approximation, the simulation can complement the learning results.

In this study, PVA with Glycerol was considered as a rubber elastic material and mechanical dynamics was expressed by the Mooney-Rivlin model [21,22], where the Mooney coefficient was determined by well-known empirical formula.

In this study, the elastic modulus of the PVA with Glycerol was substituted by the elastic modulus of PMMA (Polymethyl methacrylate). By the similarity rule, the pattern shape after nanoimprinting was assumed to be uniquely determined by the relative pressure, *P/E* as discussed, which the relative value of press pressure P is and elastic modulus *E*.

Thanks to this approximation, measurement of the actual elastic modulus of each resin is skipped and provides a relative relationship of the molding height to the press pressure. Changes in the shape of the mold can be handled in the same way.

3. Results and discussion

Table 1 shows examples of the experimental results for learning data. The weight present of the added Glycerol to PVA is varied from 0 to 25 %. The nanoimprinting temperatures were 100, 130, and 150 °C, respectively. The pressing pressure is 10 [MPa]. The total number of learning data sets was 43.

Figure 3 demonstrates deep learning results of the pattern height after nanoimprint for various pressing temperature and Glycerol concentrations.

In this system, the inputs are press temperature, pressure, pressing time, baking temperature, and baking time as a process conditions, and Glycerol concentration as a material condition, and pattern width, pattern height of mold, and initial thickness as a topological parameter.

The learning system has 2 intermediate layers, and each layer has 11 nodes, which are determined regarding to the learning error. The learning coefficient was set to 0.01 and number of learning epochs was over 5,000.

Table. 1 Experimental result for PVA with Glycerol (Pressure:10MPa)

w. % ℃	0.0	10.0	16.6	25.0
100	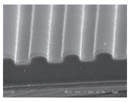	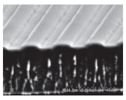	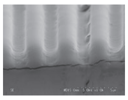	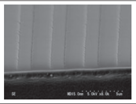
130	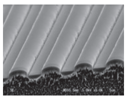	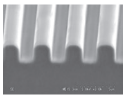	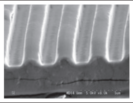	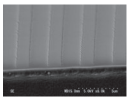
150	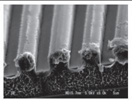	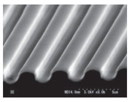	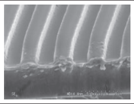	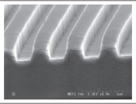

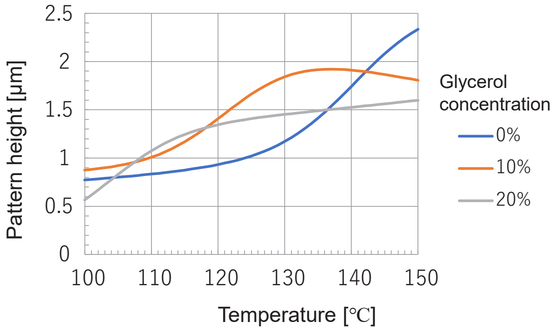

Fig. 3. Learning results of the prospected pattern height for various pressing temperature and Glycerol concentration.

Based on deep learning, the pattern height after nanoimprinting could be prospected in any temperatures and Glycerol concentrations under constant pressure.

Nevertheless, the pressure dependence is not included because it was out of consideration in learning experiments. To complement the pressure dependence, the relationship between relative pressure and relative height is calculated using simulation in advance as demonstrated in Figure 4.

Then, from the relative height predicted by the artificial intelligence, the relative breath pressure is obtained from Figure 4. Then, the pattern height at any given pressure can be estimated based on the relative pressure.

Figure 5 demonstrates experiments and prediction results for various pressures when the nanoimprinting temperature is 100 ℃ and the concentration of Glycerol is 25%. The solid line shows the predicted pattern height after nanoimprint in variation with pressure, and the squares experimental results at 5MPa and 15 MPa, respectively. The prediction by the deep learning shows good agreements to experimental results.

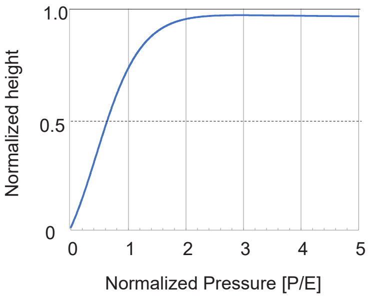

Fig. 4. Simulated relation between normalized pressure and pattern height by nanoimprint under fixed topological condition. (Aspect ratio of mold pattern:1.2)

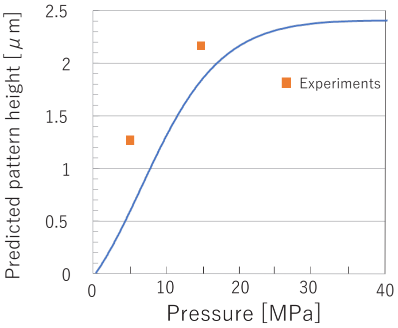

Fig. 5. Prediction by deep learning and experimental results. The nanoimprinting temperature was 100℃ and the concentration of Glycerol was 25%. (Solid line: Prediction, Squares: Experiments)

4. Conclusion

We firstly proposed smart design systems for process and material for nanoimprint, based on hybrid system of deep learning and numerical simulation. The hybrid smart system well predicts results for unknown process conditions and materials in nanoimprint.

The system will expand for various materials and topological structures and confirm the results.

References

1. S. Chou, P. Krauss, and P. Renstrom, *Appl. Phys. Lett.*, **67** (1995) 3114.
2. S. Chou, P. Krauss, and P. Renstrom, *J. Vac. Sci. Technol. B*, **14** (1996) 4129.
3. M. Austin and S. Chou, *Appl. Phys. Lett.*, **81** (2002) 4431.
4. G. Leising, B. Stadlober, U. Haas, A. Haase, C Palfinger, H. Gold, and G. Jakopic, *Microelectronic Eng.*, **83** (2006) 831.
5. K. Tomohiro, N. Hoto, H. Kawata, and Y. Hirai, *J. Photopolymer Sci. Technol.*, **24** (2011) 71.
6. M. Li, H. Tan, L. Chen, J. Wang, and S. Chou, *J. Vac. Sci. Technol. B*, **21** (2003) 660.
7. Y. Hirai, K. Kanakugi, T. Yamaguchi, K. Yao, S. Kitagawa, and Y. Tanaka, *Microelectronic Eng.*,**67-68** (2003) 237.
8. Y. Hirai and Y. Tanaka, *J. Photopolymer Sci. Technol.*, **15** (2002) 474.
9. H. Yang, L. Luo, J. Su, C. Lin, and B. Yua, *J. Micro/Nanolith. MEMS MOEMS*, **16** (2017) 033504.
10. X. Ma, X. Zheng, and G. Arce, *Optics Express*, **28** (2020) 20404.
11. T. Akter and S. Desai, *Materials and Design*, **160** (2018) 836.
12. S. Aihara, N. Takakura, F. Kizu, S. Jimbo, K. Ishibashi, J. Seki, Y. Oguchi, T. Asano, Y. Matsuoka, M. Tamura, and O. Morimoto, *Proc. SPIE* **11610** (2021) 1161007.
13. Y. Hirai, M. Fujiwara., T. Okuno, Y. Tanaka, M. Endo, S. Irie, K. Nakagawa, and M. Sasago, *J. Vac. Sci. Technol. B*, **19** (2001) 2811.
14. Y. Hirai, S. Yoshida, and N. Takagi, *J. Vac. Sci. Technol. B*, **21** (2003) 2765.
15. Y. Hirai, T. Konishi, T. Yoshikawa, and S. Yoshida, *J. Vac. Sci. Technol. B*, **22** (2004) 3288.
16. Y. Hirai, Y. Onishi, T. Tanabe, M. Shibata, T. Iwasaki, and Y. Irie, *Microelectronic Eng.*, **85** (2008) 842.
17. Y. Hirai, T. Yoshikawa, N. Takagi, and S. Yoshida, *J. Photopolymer Sci. Technol.*, **16** (2003) 615.
18. D. Specht, *Neural Networks*, **3** (1990) 109.
19. D. Specht, *IEEE Trans. Neural Networks*, **2** (1991) 568.
20. Y. LeCun, Y. Bengio, and G. Hinton, *Nature* **521** (2015) 436.
21. M. Moony, *J. Appl. Phys.* **11** (1940) 582.
22. R. S. Rivlin, *Phil. Trans. Roy. Soc. London*, Ser. A **241**, (1948) 379.

Communication

Journal of Photopolymer Science and Technology
Volume 34, Number 2 (2021) 149－153 ©2021SPST

Flexible and Semi-Transparent Antenna for ISM Band Fabricated by Direct Laser Writing

Ashiqur Rahman[1,2] and Akira Watanabe[1]

[1]Institute of Multidisciplinary Research for Advanced Materials,
Tohoku University,2-1-1 Katahira, Aoba-ku, Sendai 980-8577, Japan
[2]Department of Electrical and Electronics Engineering, Faculty of
Engineering, American International University Bangldesh, 408/1, Kuratoli
Road, Kuril Dhaka-1229, Bangladesh
**rahman.ashiqur.b8@tohoku.ac.jp*

In this paper, a flexible and semi-transparent antenna is proposed having impedance bandwidth of 110 MHz (from 2.45 GHz to 2.56 GHz) of ISM band which covers the most popular (2.4 GHz) for Wi-Fi application all over the world. A simple dipole shape rectangular ring antenna with two extended edge on the opposite sides was prepared by laser direct writing on an Au sputtered PET film. The center part of the antenna was kept empty and transparent intentionally to incorporate with either a planar capacitor for microwave wireless charging or to integrate this antenna with a solar cell in future. The compact, miniature and flexibility of the antenna are suitable for easy integration in any smart devices or clothing for wireless charging to implement self-powered sensors. The performance of the patch antenna is evaluated using return loss (S11) parameter analysis. A measured reflection coefficient and simulated current distribution along with radiation pattern demonstrate that the fabricated antenna is suitable for Wi-Fi application.

Keywords: Flexible, Semi-transparent, Direct Laser writing, Wi-Fi

1. Introduction

Flexible electronics describe circuits that can bend and stretch, enabling significant versatility in applications and the prospect of low-cost manufacturing processes. A flexible substrate should be mechanically robust with highly deformability and extreme tolerance levels of bending repeatability to adapt with flexible technologies and integrated components. Flexible electronics have been extensively studied because they provide a simple means of integrating electronic devices on curved surfaces for various applications, such as wearable devices, artificial skins, flexible displays, and flexible solar energy harvesters [1]. All of these reconfigurable antennas are mainly focused on frequency tuning and exhibit their radiation patterns with relatively low directivity. Moreover, the flexible antennas have over-performance compared to rigid devices, in terms of compactness, flexibility, durability, lightweight, and energy efficiency. However, the antenna designers working on flexible antennas must address some challenges, including the shift of the resonant frequency and degradation impedance mismatch due to the variation of effective capacitance during bending of the antenna. Other than the reconfiguration and flexibility characteristics, the antenna compactness is highly appreciated as the miniaturized antennas significantly reduce the size of electronic systems [2]. Furthermore, optically transparent antennas have attracted a great deal of interest in the recent years due to the potential applications in solar panels integrated with satellites, smart windows and other related areas [3]. However, the realization of flexible and optically transparent patch antennas is very challenging due to the unavailability of suitable materials and complex fabrication processes.

In the traditional transparent thin films [4] and meshed conductors [5], there is a tradeoff between the optical and electrical properties, hence, high

---

Received March 31, 2021
Accepted April 9, 2021

optical transparency and good RF performance cannot be achieved simultaneously. Moreover, complex and costly fabrication techniques are required to fabricate antennas with these materials. It is also challenging to maintain robust integration of these transparent conductors with flexible substrates in harsh physical deformations [6].

In near future, all the devices will be interconnected that linked with an internet itself. Smart energy distribution, health care, smart cities and smart car supposed to exchange information in forthcoming years through internet access. In massive IoT applications, consistent wireless connectivity between sensor and cloud is prerequisite with the cost of sufficient low power. Radio frequency (RF) band for GSM, 3G, LTE, and Wi-Fi with frequencies between 900 MHz and 2.6 GHz are considered as one of the potential and optimistic sources in urban environment due to their greatest amount of ambient energy. However, there is a need for low-cost and eco-friendly antenna materials that are flexible and/or optically transparent to fully embody the ubiquitous potential of IoT [7]. Flexible wireless sensors could be integrated as wearables in clothing [8] or directly on the human body to monitor, for instance, the temperature, blood pressure and heart rate of patients on a continuous basis [9].

The innovation of sensor manufacturing process both in material and fabrication technique is necessary to reduce the cost of them. The printed electronics is one of the candidates for the innovative manufacturing. The contribution of laser processing in printed electronics is expected because of the compatibility with on-demand manufacturing and role-to-role processing [10]. A number of printing and lithographic techniques have been used for the preparation of in plane patch antenna, but further improvements in cost, fabrication time, scalability, and compatibility to the current electronic industry are required to exert their full potential and commercialization. Laser direct writing is a noncontact, fast, single-step fabrication technique with no need for masks, post processing, and a complex clean room, and compatible with current electronic product lines for commercial use. Thus, it has potential to be employed in the fabrication of materials with specific patterns and even preparation of self-powered integrated stretchable devices [11]. The advantages of the laser direct writing are the high resolution up to sub-micron level and the fast sintering process where the local heating at a small laser beam focal point reduces the damage of a polymer substrate in flexible device manufacturing [12].In this paper a compact, flexible and semi-transparent antenna for (Industrial, Scientific and Medical) ISM band that achieves a stable impedance bandwidth even after 5 mm bending diameter has been designed and investigated. The planar antenna consists of a simple rectangular ring structure with extended length at opposite direction. The antenna structure is flat and its design is simple and straightforward.

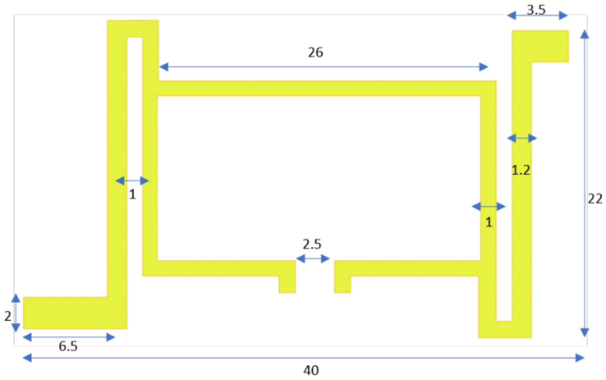

Fig. 1. Dimension in mm of the proposed antenna.

2. Material Preparation and Antenna Design

Figure 1 shows the geometrical layout of the proposed laser-written antenna pattern, which consists of a simple dipole shape rectangular ring. The patch, which has a compact dimension of 40×22 mm, is prepared in an inexpensive (polyethylene terephthalate) PET substrate of relative permittivity 2.1, loss tangent 0.003 and thickness 0.5 mm, which is a special PET film designed for monochrome laser printing (A-ONE 27054). The surface roughness of the PET film improved the adhesion between Au layer and PET substrate. Thin substrates with lower dielectric constants are desirable for good antenna performance because they minimize undesired radiation and coupling and provide better efficiency and larger bandwidth, respectively [13]. The performance of the antenna has been analyzed by AXIEM 3D planar method-of-moments (MoM) EM analysis simulator by Cadence. The proposed antenna is designed to operate at 2.45 GHz to 2.56 GHz to cover the Wi-Fi band. At first deep UV treatment using a UV/ozone surface processor equipped with a low-pressure Hg lamp (PL-16, SEN LIGHTS Co., Ltd.) was carried out for 10 minutes followed by Au sputtering of 120 nm thickness by JFC-1500 ion sputtering device. Finally, an antenna pattern was drawn by laser ablation using a galvano-scanning of the laser beam controlled witha laser marking software (BJJCZ, EzCAD). The laser source was an ns fiber laser (Raycus, RFL-P30Q, 1064 nm, 34 W, pulse width 125 ns, 30-60 kHz). The laser beam was scanned by a galvano-scanner through an f-θ lens with the focus length of 100 mm. The return loss spectra were observed by a Tektronix TTR506A vector network analyzer for both flat and bending condition from 55 mm to 5 mm bending diameter. The transparency of the realized antenna was measured by spectrophotometer by Jasco V-670, within the wavelength from 300 to 1100 nm.

3. Simulation and Experimental Results

The semi-transparent antenna was subsequently fabricated for experimental verification, as shown in Figure 2a and 2b. The variation of the optical transparency of the fabricated antenna exhibits in figure 3. The transparency is about 87.7% for the PET before Au sputtering at 500 nm wavelength. The transparency drops to 67.5% and 34 % in the center of the rectangular ring structure and on Au layer of the antenna respectively as predicted. Figure 4 illustrates the plots of the reflection coefficient (S11) for both simulation and measurement of the proposed antenna. It is observed from the plot that the prototyped antenna achieved a good impedance matching from 2.45 to 2.56 GHz with a measured|S11| parameter below -10dB. The return loss was reduced to a highest value of 15.45 dB and 35 dB for the simulation and measured results, respectively. The simulation and measured operating bandwidth of the proposed antenna were found to be 90 MHz and 110 MHz respectively with resonant frequency at 2.49 GHz which covers the entire Wi-Fi frequencies as mentioned earlier. A small deviation was observed because of the fabrication tolerance.

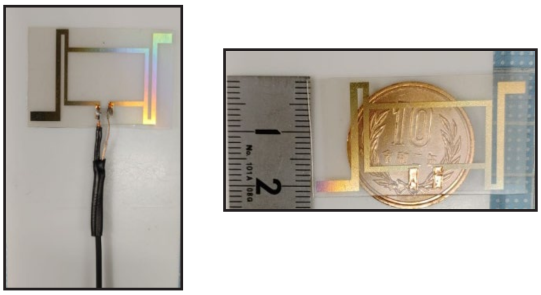

Fig. 2. a) Prototype of the antenna b) Transparency of the fabricated antenna

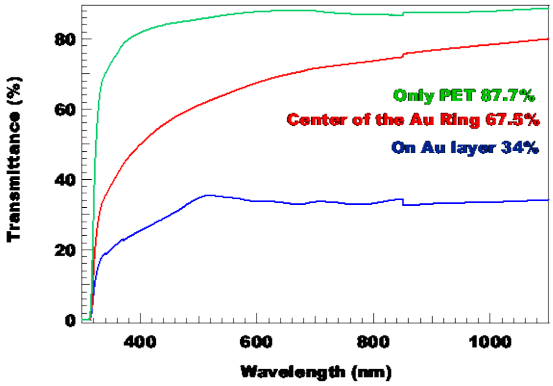

Fig. 3. Variation of measured transparency

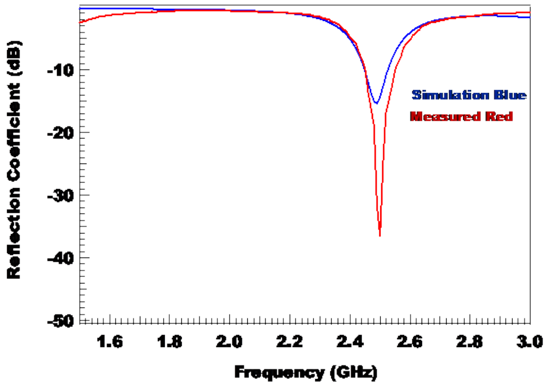

Fig. 4. Simulation and measured reflection coefficient

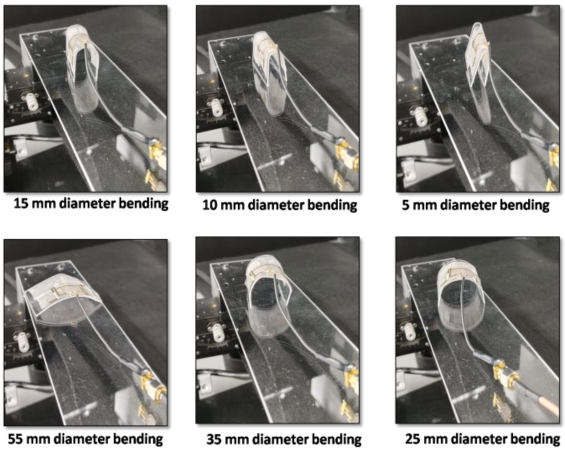
15 mm diameter bending
10 mm diameter bending
5 mm diameter bending
55 mm diameter bending
35 mm diameter bending
25 mm diameter bending

Fig. 5. Bending measurement process

The material exhibits remarkable flexibility and robustness, consequently, without any mechanical damage the antenna can be bent until 5 mm bending diameter as shown in Figure 5. The reflection coefficient against the frequency for the antenna bending from 55 mm to 5 mm were illustrated in Figure 6. Such bending experiments were carried out from the practical interest to

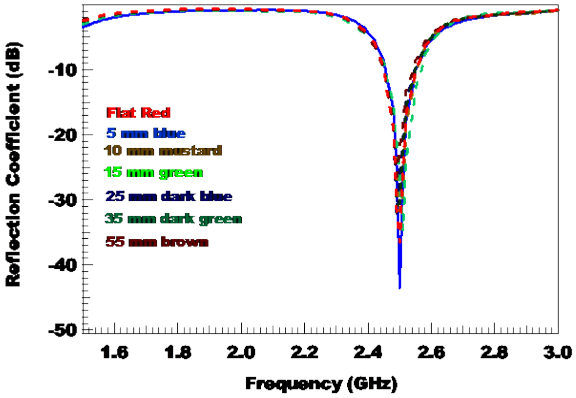

Fig. 6. Measured reflection coefficient for different bending diameter

demonstrate the flexibility of this antenna. From the figure it was observed that for all the cases the variation of the antenna resonance frequency was only 2 MHz but with constant impedance bandwidth.

The simulated surface current distributions of the proposed antenna at resonance frequency of 2.49 GHz are illustrated in Figure 7. It is seen that, the strongest currents are concentrated on the right wing and the upper left side of the patch antenna and play a key role in creating resonance and omnidirectional radiation pattern.

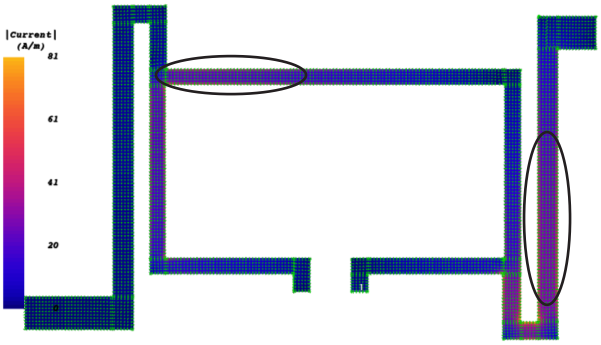

Fig. 7. Simulated surface current distribution of the proposed antenna

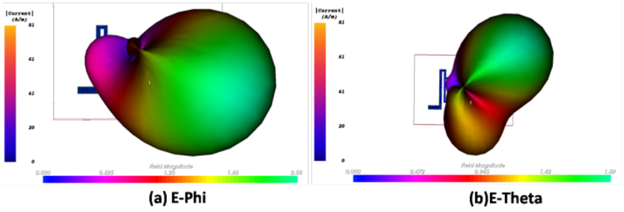
(a) E-Phi

(b)E-Theta

Fig. 8. a) Simulated 3D radiation pattern for E-Phi
b) Simulated 3D radiation pattern for E-Theta

The presented antenna achieves a wider frequency range because the surface current maintains a harmonic order flow. From Figure 8 we can observe the simulated 3D radiation pattern of the proposed antenna. Figure 8a and 8b depicted an omnidirectional and donut shape radiation pattern for E-Phi and E-Theta respectively. Figure 9a and 9b demonstrate the top and bottom of the total radiation pattern. A considerable amount of back lobe has also been observed.

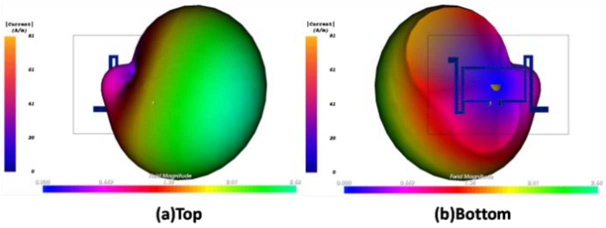
(a)Top

(b)Bottom

Fig. 9. (a) Simulated 3D radiation pattern from top view
(b) Simulated 3D radiation pattern from bottom view

4. Conclusion

In this paper, a flexible and semi-transparent antenna is presented for Wi-Fi antenna application. Experimental results demonstrate that, the fabricated antenna could achieve an impedance bandwidth from 2.45 GHz to 2.56 GHz both in flat and 5 mm bending diameter status. The design of the proposed antenna is simple, easy to fabricate and will be compatible for any flexible electronic devices.

Acknowledgement

This work was partially supported by JSPS KAKENHI Grant Number JP19H05356.

References

1. W. Li, A. Meredov, K. Klionovski, and A. Shamim, *2019 IEEE Indian Conference on Antennas and Propogation (InCAP)*, Ahmedabad, India, (2019) 1.
2. N. Hussain, W.A. Awan, S.I. Naqvi, A. Ghaffar, A. Zaidi, S.A. Naqvi, A. Iftikhar, and X.J. Li, *IEEE Access*, **8**, (2020) 173298.
3. H. A. E. Elobaid, S. K. A. Rahim, M. Himdi, X. Castel, and M. A. Kasgari, *IEEE Antennas and Wireless Propagation Letters*, **16** (2017) 1336.
4. S. Y. Lee, M. Choo, S. Jung, and W. Hong, *Appl. Sci.*, **8** (2018) 901.
5. T. Jang, C. Zhang, H. Youn, J. Zhou, and L. J. Guo, *IEEE Trans. Antennas Propag.*, **65** (2017)

50.

6. A. S. M. Sayem, D.Le, R.B.V.B. Simor, T. Bjorninen, K.P. Esselle, R.M. Hashmi, and M. Zhadobov, *IEEE Antennas and Wireless Propagation Letters,* **19** (2020) 2334.
7. M. A. Andersson, A. Özçelikkale, M. Johansson, U. Engström, A. Vorobiev, and J. Stake, *IEEE Access*, **4** (2016) 5850.
8. M. M. Ur Rashid, A. Rahman, L. C. Paul, and A. Krishno Sarkar, *2019 1st International Conference on Advances in Science, Engineering and Robotics Technology (ICASERT)*, Dhaka, Bangladesh, (2019) 1.
9. S. M. R. Islam, D. Kwak, M. H. Kabir, M. Hossain, and K.-S. Kwak, *IEEE Access*, **3** (2015) 678.
10. A. Watanabe, A. Rahman, J. Cai, and M. Aminuzzaman, *J. Photopolym. Sci. Technol*, **33** (2020) 2.
11. A. Watanabe, A. Rahman, J. Cai, and M. Aminuzzaman, *Proc. SPIE*, **11674** (2021) 116740T.
12. A. Watanabe, A. Rahman, J. Cai, and M. Aminuzzaman, *Proc. SPIE*, **11268** (2020) 1126817.
13. A. Rahman, M.T. Islam, M. Samsuzzaman, M.J. Singh, and M. Akhtaruzzaman*, Materials*, **9** (2016) 5.

Journal of Photopolymer Science and Technology
Volume 34, Number 2 (2021) 155−159 ©2021SPST

Communication

Self-assembly of Amphiphilic Peptide in Phospholipid Membrane

Anju Kawakita, Noriyuki Uchida*, Yunosuke Ryu, and Takahiro Muraoka*

Department of Applied Chemistry, Graduate School of Engineering, Tokyo University of Agriculture and Technology, 2-24-16 Nakacho, Koganei, Tokyo 184-8588, Japan
**n-uchida@go.tuat.ac.jp *muraoka@go.tuat.ac.jp*

An amphiphilic molecule **Lipid-(RADA)₂** consisting of a repeating RADA peptide sequence and alkyl chains appending a fluorescent nitrobenzoxadiazole (NBD) dye, was synthesized. In a fluorescence microscopic observation, localization of an aggregate containing **Lipid-(RADA)₂** at a bilayer membrane formed with 1,2-dioleoyl-*sn*-glycero-3-phosphocholine (DOPC) was observed.

Keywords: Peptide, Phospholipid, Self-assembly, Fluorescence microscopy, Vesicle

1. Introduction

In physiological conditions, cells control various biological functions by assembling biomolecules in a bilayer membrane [1–5]. For example, lipid raft, a type of membrane microdomain composed of self-assemblies of sphingolipids and cholesterol, accumulates membrane proteins, and plays important roles in signal transduction through the membrane, infection of bacteria and viruses, cell adhesion, vesicle transport, and intracellular polarity [1–3]. Inspired by the lipid raft formation in a biological membrane, a variety of synthetic methodologies of self-assembly in a bilayer membrane have been developed. For example, self-assemblies of nucleic acids [6], saccharides [7], synthetic polymers [8] and peptides [9] in phospholipid membranes have been reported.

Peptide-based self-assemblies in aqueous media are an attractive platform capable of imparting various bioactive functions by controlling the amino acid sequence. Indeed, a lot of biomaterials with superb functions have been realized by using self-assembling peptides [10–20]. In this work, to study self-assembly of peptides at a bilayer membrane, we designed an amphiphilic molecule **Lipid-(RADA)₂**. **Lipid-(RADA)₂** consists of a peptide headgroup having a repeating RADA sequence and alkyl chains attached at main-chain and side-chain amino groups of the N-terminal lysine residue, in which a fluorescent nitrobenzoxadiazole (NBD) dye was appended (Figure 1). **(RADA)₂** peptide has alternating hydrophilic (R and D) and hydrophobic (A) amino acid residues [21]. Such an alternating sequence between hydrophilic and hydrophobic amino acid residues is known to be favorable to form a β-sheet

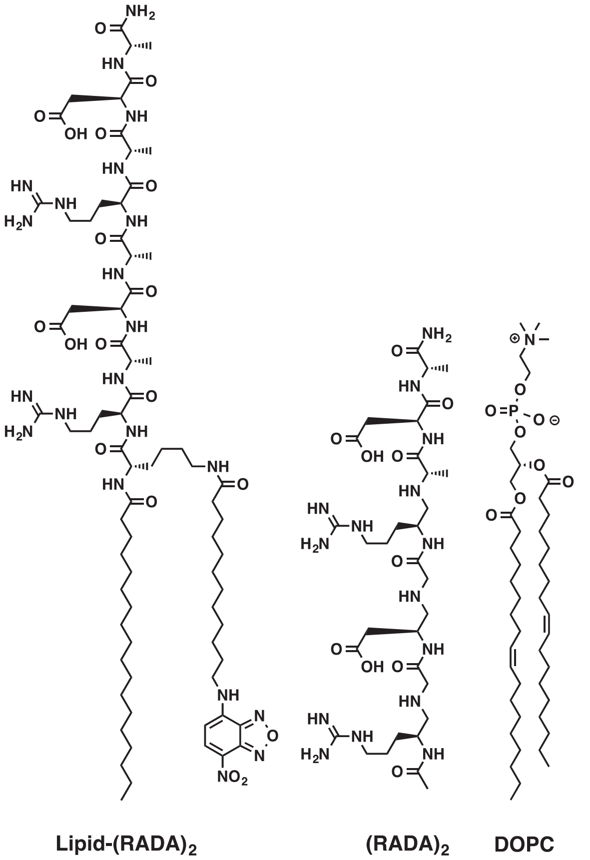

Fig. 1. Molecular structures of **Lipid-(RADA)₂**, **(RADA)₂**, and DOPC used in this study.

Received March 9, 2021
Accepted April 16, 2021

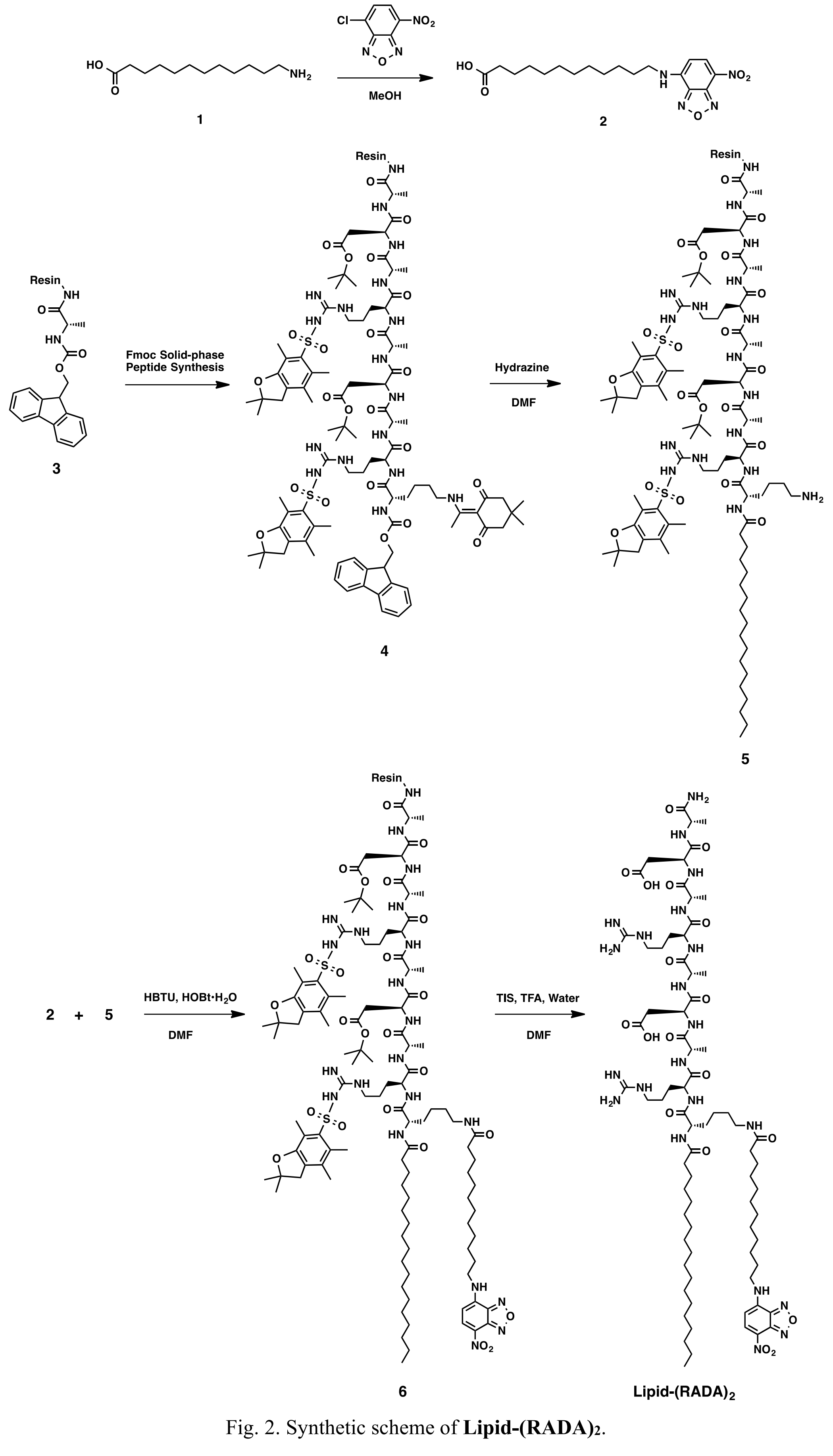

Fig. 2. Synthetic scheme of **Lipid-(RADA)₂**.

self-assembly [18–20]. The alkyl chains with a fluorescent group were attached to **(RADA)₂** peptide as an anchoring unit into the phospholipid membranes and for direct observation under a fluorescence microscopy.

2. Methods

2.1. General

^{1}H nuclear magnetic resonance (NMR) spectra were recorded on a JEOL ECX-400 spectrometer. High-resolution electrospray ionization time-of-fight mass (HR ESI TOF MS) spectra were recorded on a Bruker micrOTOF-QII. Fluorescence and phase-contrast microscopic observations were performed with an Olympus IX-73 microscope.

2.2. Reagents

N,N'-Dimethylformamide (DMF), Et_2O, *N*-methyl-2-pyrrolidone (NMP), piperidine, and trifluoroacetic acid (TFA) were purchased from Kishida Chemical (Tokyo, Japan). *N,N*-Diisopropylethylamine (DIEA), hydrazine monohydrate and mineral oil were purchased from Nacalai Tesque (Kyoto, Japan). Stearic acid, 12-aminolauric acid (**1**), NBD-Cl, and triisopropylsilane (TIS) were purchased from Tokyo Chemical Industry (Tokyo, Japan). Fmoc-Ala-OH•H_2O, Fmoc-Arg(Pbf)-OH, Fmoc-Asp(OtBu)-OH, Fmoc-Lys(Dde)-OH, Fmoc-NH-SAL Resin, HATU, HBTU, and HOBt•H_2O were purchased from Watanabe Chemical Industries (Hiroshima, Japan). 1,2-Dioleoyl-*sn*-glycero-3-phosphocholine (DOPC) was purchased from Avanti (Alabama, U.S.A.). Ultrapure water (filtered through a 0.22 μm membrane filter, >18.2 MΩ cm) was purified in Purelab DV35 of ELGA (Buckinghamshire, UK).

2.3. Synthesis

2.3.1. Synthesis of **2**

To an aqueous solution (4.5 mL) of $NaHCO_3$ (0.88 g, 10.5 mmol), a MeOH solution (25 mL) of **1** (2.3 g, 10.5 mmol) was added at 50 °C and stirred for 10 min. To the resulting solution, a MeOH solution (18 mL) of NBD-Cl (0.30 g, 1.5 mmol) was added and stirred for 2 h at 50 °C. After cooling to room temperature, the reaction mixture was filtered, and the filtrate was extracted with CH_2Cl_2 (20 mL, three times). The collected organic phase was evaporated and the residue was chromatographed on silica gel with a mixture of $CHCl_3$ and MeOH (10/1 v/v) as an eluent, followed by recrystallization from a mixture of CH_2Cl_2 and *n*-hexane to allow isolation of **2** (473 mg, 1.25 mmol) in 83% yield.

^{1}H NMR ($CDCl_3$, 400 MHz): $\delta = 8.49$ (d, $J = 8.8$ Hz, 1H), 6.46 (s, 1H), 6.19 (d, $J = 8.8$ Hz, 1H), 3.50 (q, $J = 6.4$ Hz, 2H), 2.35 (t, $J = 7.2$ Hz, 2H), 1.82 (quin, $J = 7.3$ Hz, 2H), 1.63 (quin, $J = 7.5$ Hz, 2H), 1.47 (quin, $J = 7.4$ Hz, 2H), 1.29 (m, 12H).

2.3.2. Synthesis of **(RADA)₂** and **Lipid-(RADA)₂**

(RADA)₂ and **Lipid-(RADA)₂** were synthesized by Fmoc solid-phase peptide synthesis as shown in Figure 2. A mixture of HBTU (3.05 g, 8.04 mmol) and HOBt•H_2O (1.25 g, 8.16 mmol) in DMF (16 mL) as condensation reagents, a mixture of DIEA (2.8 mL) and NMP (14.3 mL), and a mixture of TIS (62.5 μL), TFA (2.4 mL), and water (62.5 μL) as cleavage reagents were prepared just before the synthesis. Fmoc-NH-SAL Resin (0.1 mmol) was dispersed in DMF (2 mL) in a polypropylene tube and soaked over 3 h at 25 °C. After removing DMF by filtration, piperidine in DMF (20%, 2 mL) was added to the resin and mixed with a vortex device for 1 min. After removing the reaction solution, piperidine in DMF (20%, 2 mL) was added and the reaction mixture was shaken for 10 min at 25 °C. After removal of the solution phase of the reaction mixture, the resin was washed with DMF (2 mL, 5 times), CH_2Cl_2 (2 mL, 3 times) and DMF (2 mL, 3 times). Then, Fmoc-protected amino acid (0.3 mmol) dissolved in the mixture of condensation reagents (700 μL) and the mixture of DIEA and NMP (700 μL) was added to the resin. After shaking for 15 min at 25 °C, the solution phase of the mixture was removed by filtration and the resin was washed with DMF (2 mL, 5 times), CH_2Cl_2 (2 mL, 3 times) and DMF (2 mL, 3 times). The Fmoc deprotection reactions with piperidine and coupling reactions of Fmoc-protected amino acid were repeated following the designed sequence. For the synthesis of **Lipid-(RADA)₂**, after the deprotection of Fmoc group of **4**, stearic acid (142.2 mg, 0.5 mmol) was coupled using HATU (186.5 mg, 0.49 mmol) and DIEA (0.17 mL, 1.00 mmol) in DMF (1.5 mL), which was then reacted with hydrazine monohydrate (30 μM) in DMF (1.5 mL) for deprotection of the Dde group to afford **5**. **5** was coupled with **2** (189.2 mg, 0.50 mmol) using HATU (186.5 mg, 0.49 mmol) and DIEA (0.17 mL, 1.00 mmol) in DMF (1.5 mL) to afford **6**. After removal of the solution phase of the reaction mixture, the resin was washed with DMF (2 mL, 5 times), CH_2Cl_2 (2 mL, 3 times) and DMF (2 mL, 3 times). The mixture of cleavage reagents (2.5 mL) was added to the resin and the reaction tube was left to stand for 90 min at 25 °C with gentle shaking every 30 min. The solution was collected into a polypropylene centrifuge tube by filtration. The reaction tube was rinsed with TFA (500 μL, 3 times), which is also collected by filtration. To the centrifuge tube Et_2O (40 mL) was added and the tube was mixed on a vortex device for 1 min followed by centrifugation at 4 °C (3500 × g, 5 min) and removal of the supernatant liquid. After repeating this process for 3 times, the residue was dried under vacuum over 2 h at 25 °C, dispersed in water and lyophilized.

HR ESI TOF MS: *m/z* calculated for $C_{74}H_{129}N_{21}O_{18}^{2+}$ [**Lipid-(RADA)₂** + 2H]$^{2+}$ 799.9834; found 799.9855.

3. Results and discussion

To study self-assembly of **Lipid-(RADA)₂** at a lipid bilayer membrane, DOPC giant unilamellar vesicles (GUVs) were prepared in the presence of **Lipid-(RADA)₂**. A 10 μL of $CHCl_3$/MeOH (2/1) solution of DOPC (2 mM) and a 10 μL of MeOH solution of **Lipid-(RADA)₂** (2 μM) were mixed in a glass test tube, and the mixture was gently dried under N_2 flow to produce thin lipid film. The film was subsequently dried under vacuum over 3 h at 25 °C. 200 μL of mineral oil was added to the lipid film and sonicated for 1 h. For the preparation of an emulsion, a 75 μL of the resulting mineral oil solution was mixed with a 3 μL of sucrose aq. (200 mM). The remaining mineral oil solution (125 μL) was gently put on a 50 μL of glucose aq. (200 mM) and the mixture was centrifuged (1600 × g) for 1 min. After the centrifugation, a 50 μL of the emulsion was put on top of the resulting mixture and centrifuged (1600 × g) for 1 min. On the top of the resulting mixture after the centrifugation, a 50 μL of the emulsion was put on and centrifuged (1600 × g) for 1 min. After removing the upper layer composed of the mineral oil, the lower layer was collected for the microscopic observations.

Phase-contrast micrographic observation showed a ring image (Figure 3a), indicating the formation of a GUV. A ring image was also observed by fluorescence microscopy, indicating localization of **Lipid-(RADA)₂** at the DOPC bilayer membrane. Interestingly, the fluorescence microscopic observation showed a bright spot with a strong fluorescence intensity at a part of the membrane (Figure 3b, yellow arrow), suggesting localization of an aggregate containing **Lipid-(RADA)₂**. It is also noteworthy to mention that, in the phase-contrast micrograph, intravesicular medium is relatively dark compared to the extravesicular medium. This is likely due to the different refractive index between glucose and sucrose aqueous solutions, and the sucrose solution was enclosed in the vesicle. Thus, it is likely that a mixture of DOPC and **Lipid-(RADA)₂** ([DOPC]/[**Lipid-(RADA)₂**] = 1000/1) formed a stable bilayer membrane with a localization of an aggregate containing **Lipid-(RADA)₂**.

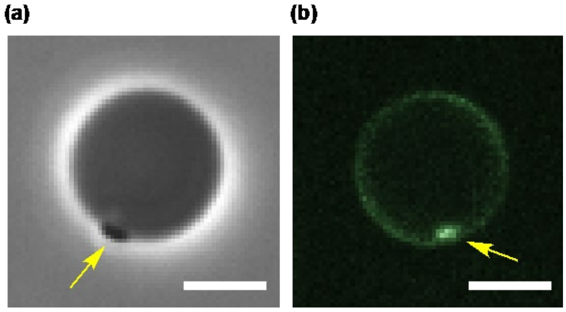

Fig. 3. Phase-contrast micrograph (a) and fluorescence micrograph (b) of the DOPC vesicle containing **Lipid-(RADA)₂** (DOPC/Lipid-(RADA)₂ = 1000/1). Yellow arrows indicate an aggregate containing **Lipid-(RADA)₂**. Scale bar = 5 μm.

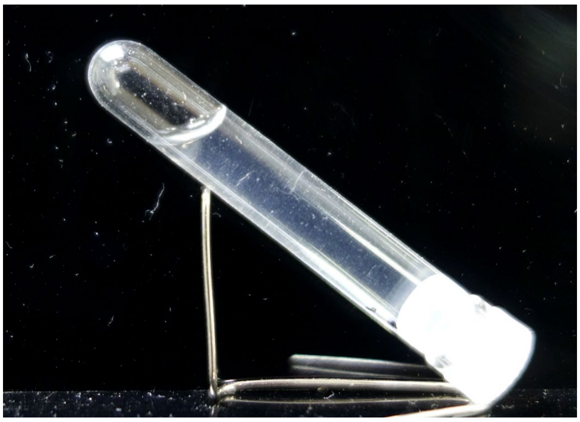

Fig. 4. A photograph of **(RADA)₂** in water containing 2.2% trifluoroacetic acid.

As shown in Figure 4, **(RADA)₂** in water formed dispersed precipitates indicating the self-assembling property. This result suggests that the self-assembling property of the **(RADA)₂** unit likely contributes to the aggregate formation, at least partially, of **Lipid-(RADA)₂** at the membrane. Detailed analyses of the self-assembling structures of **Lipid-(RADA)₂** at the membrane and physicochemical properties of DOPC GUVs containing **Lipid-(RADA)₂** are currently under investigation.

4. Conclusion

We synthesized **Lipid-(RADA)₂**, a lipid consisting of a peptide with a self-assembling property and a fluorescent probe, and studied its localization at a bilayer membrane. Microscopic observations indicated that **Lipid-(RADA)$_2$** was localized at a DOPC bilayer membrane, and an aggregate containing **Lipid-(RADA)$_2$** was visualized at the membrane.

Acknowledgement

This work was partly supported by JSPS Grant-in-Aid for Early-Career Scientists (JP19K15378 to N.U.), JACI grant (N.U.), JST CREST (JPMJCR19S4 to T.M.) and JSPS Grants-in-Aid for Scientific Research B (JP19H02828 to T.M.).

References

1. D. Lingwood and K. Simons, *Science*, **327** (2010) 46.
2. K. Simons and W. L. C. Vaz, *Annu. Rev. Biophys. Biomol. Struct.*, **33** (2004) 269.
3. K. Simons and M. J. Gerl, *Nat. Rev. Mol. Cell Biol.*, **11** (2010) 688.
4. T. Sych, Y. Mély, and W. Römer, *Phil. Trans. R. Soc. B*, **373** (2018) 20170117.
5. P. Monnard and D. W. Deamer, *Anat. Rec.,* **268** (2002) 196.
6. A. Patwa, A. Gissot, I. Bestel, and P. Barthélémy, *Chem. Soc. Rev.*, **40** (2011) 5844.
7. M. Hato, H. Minamikawa, K. Tamada, T. Baba, and Y. Tanabe, *Adv. Colloid Interface Sci.*, **80** (1999) 233.
8. L. Hosta-Rigau, Y. Zhang, B. M. Teo, A. Postma, and B. Städler, *Nanoscale*, **5** (2013) 89.
9. Y. Zhou, *Crit. Rev. Solid State Mater. Sci.*, **33** (2008) 183.
10. D. A. Slick, J. K. Kretsinger, D. J. Pochan, and J. P. Schneider, *J. Am. Chem. Soc.,* **129** (2007) 14793.
11. V. A. Kumar, S. Shi, B. K. Wang, I. Li, A. A. Jalan, B. Sarkar, N. C. Wickremasinghe, and J. D. Hartgerink, *J. Am. Chem. Soc.,* **137** (2015) 4823.
12. T. L. Lopez-Silva, D. G. Leach, A. Azares, I. Li, D. G. Woodside, and J. D. Hartgerink, *Biomaterials*, **231** (2020) 119667.
13. X. Yan, P. Zhu, and J. Li, *Chem. Soc. Rev.*, **39** (2010) 1877.
14. Z. Yu, F. Tantakitti, T. Yu, L. C. Palmer, G. C. Schatz, and S. I. Stupp, *Science*, **351** (2016) 497.
15. T. Fan, X. Yu, B. Shen, and L. Sun, *J. Nanomaterials*, **2017** (2017) 4562427.
16. P. Sharma, H. Kaur, and S. Roy, *Biomacromolecules*, **20** (2019) 2610.
17. H. Yokoi, T. Kinoshita, and S. Zhang, *Proc. Natl. Acad. Sci. U. S. A.*, **102** (2005) 8414.
18. A. Ishida, G. Watanabe, M. Oshikawa, I. Ajioka, and T. Muraoka, *Chem. Eur. J.* **25** (2019), 13523.
19. A. Ishida, M. Oshikawa, I. Ajioka, T. and Muraoka, *ACS Appl. Bio Mater.* **3** (2020), 3605.
20. R. Zou, Q. Wang, J. Wu, J. Wu, C. Schmuck, and H. Tian, *Chem. Soc. Rev.*, **44** (2015) 5200.
21. T. C. Holmes, S. de Lacalle, X. Su, G. Liu, A. Rich, and S. Zhang, *Proc. Natl. Acad. Sci. U. S. A.*, **97** (2000) 6728.

Communication

Journal of Photopolymer Science and Technology
Volume 34, Number 2 (2021) 161－165 ©2021SPST

Properties of Imidazolinium-containing Multiblock Amphiphile in Lipid Bilayer Membranes

Miki Mori and Kazushi Kinbara*

School of Life Science and Technology, Tokyo Institute of Technology
4259 B58, Nagatsuta-cho, Midori-ku, Yokohama 226-8501, Japan
**kkinbara@bio.titech.ac.jp*

A multiblock amphiphile **CBA** bearing a cationic imidazolinium moiety at its center formed different types of assembly in THF and $CHCl_3$, which show characteristic emission bands around 300 and 465 nm upon excitation at 295 and 320 nm, respectively. These assemblies were able to be transferred into lipid bilayer membranes, keeping the similar spectral profiles with those in solutions. These results indicate a new potential of self-assembling processes for the control of supramolecular architecture hierarchically formed in lipid bilayer membranes.

Keywords: Amphiphile, Self Assembly, Lipid Bilayer Membranes.

1. Introduction

Control of self-assembled architecture formed in lipid bilayer membranes is an important issue [1–11], in particular for regulating the transportation of materials across the membrane by synthetic molecules [1–7]. Meanwhile, the domain formation due to the lateral phase separation in lipid bilayer membrane has also been drawing interest, in association with raft formation which is considered to play important roles for controlling activity of membrane proteins [12–14]. We have been involved in development of multiblock amphiphiles which form stimuli-responsive ion channels [15–21] and thermally responsive assemblies in lipid bilayer membranes [22,23]. Recently, we have developed a multiblock amphiphile bearing an imidazolimium moiety at the center of molecule (**CBA**), which are able to transport anions through lipid bilayer membranes as a mobile carrier [24]. In the course of investigation of the properties of **CBA**, we have noticed that **CBA** may adopt different states of assembly in solution depending on the solvent, which were also transferable into the lipid bilayer membranes. In this study, we investigated such properties of **CBA** in different solvents based on spectroscopic analysis.

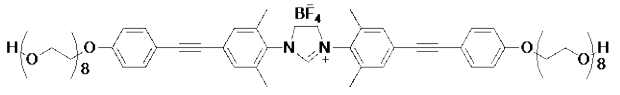

Fig. 1. Chemical structure of **CBA**.

2. Experimental

2.1. Instruments and Reagents

UV-Vis absorption spectra were recorded on JASCO V-530 UV-Vis spectrophotometer. Fluorescence spectra were recorded on JASCO FP-6500 spectrometer using quartz cell of 10-mm optical path length. TEM images were obtained using a JEOL model JEM–1400 electron microscope operating at 100 kV. TEM support grids (Catalog No. U1015) were purchased from EM Japan Co., LTD. Negative staining was performed using NANO–WTM manufactured by Nanoprobes. Large unilamellar vesicles were prepared using Avanti Mini Extruder with 100 nm polycarbonate membranes. 1,2-dioleyl-sn-glycero-3-phosphocholine (DOPC) was purchased from Avanti Polar Lipids. **CBA** was synthesized following the procedure reported in our previous paper [24].

2.2. UV-Vis absorption and emission spectroscopy in various solvents.

Received April 1, 2021
Accepted April 22, 2021

15 μL of **CBA** in $CHCl_3$ (1 mM) was taken into vial and dried under vacuum in dark, and 3 mL of each solvent (THF, $CHCl_3$, MeOH, DMSO, and H_2O) was added to the vial so as to prepare 5 μM solution. The solution was transferred into clean, dried cuvette for absorption and emission spectroscopic measurements.

2.3. Preparation of DOPC LUVs for spectroscopic analysis

$CHCl_3$ solution of DOPC (10 mM) was evaporated in glass tube to form a thin lipid film. The resulting film was dried for at least 1 h under vacuum, and hydrated with HEPES buffer (20mM HEPES, 50 mM NaCl, pH 7.1, same volume as $CHCl_3$, 10 mM final concentration) at 37 ºC, followed by freezing and thawing (5 cycles). The resulting solution was incubated at 37 ºC for at least 1 h, and then extruded by polycarbonate membranes for 21 times at room temperature.

2.4. Spectroscopic analysis in lipid bilayer membranes.

60 μL of DOPC LUVs were added to 2.94 mL of 20 mM HEPES, 50 mM NaCl, pH 7.1 buffer solution and stirred for 30 s. THF or DMSO solution of **CBA** were added to DOPC LUVs and stirred for 30 s for incorporation to lipid bilayer membranes.

2.5. TEM Observation

A 1 mM stock solution of **CBA** in THF or $CHCl_3$ was prepared and then heated at 60 ºC for 30 min followed by dilution to 100 μM.

A 5 μL of sample solution ([**CBA**] = 100 μM in THF or $CHCl_3$) was deposited onto a copper TEM grid with a carbon support film (200 mesh, EM Japan Co., LTD.) and held in place with tweezers for 1 min. The sample solution was removed by capillary action using a filter paper, and the grid was dried for another 1 min. The sample was then stained with 5 μL of NANO–W^{TM} (1wt%) for 1 min and the solution was removed by capillary action using a filter paper. The staining process was repeated once again. The grid was dried overnight before imaging.

2.6. Preparation of DOPC GUVs for microscopic observation

100 μL of 6 mM DOPC in $CHCl_3$ was coated on the ITO-coated side of glass plate and dried on heat block of 50 ºC for 5 min to make a thin lipid film. The lipid film was dried under vacuum for overnight. Silicon sheet with squared gap was filled with milliQ and covered with another ITO glass plate so that ITO glass plate would face each other. The plates were connected to the electrode, and hydrated at 50 ºC for 2 h to afford a DOPC GUV solution (ca. 2 mM).

100 μL of DOPC GUVs solutions prepared above were transferred to a vial. To this was added 1 μL of 1 mM **CBA** in THF or DMSO, and the resulting mixture was incubated at 37 ºC for at least 1 h for incorporation of **CBA$_T$** and **CBA$_C$** into the lipid bilayer membranes.

3. Results and discussion

3.1. Spectroscopic analysis of **CBA** in various solvents

First, a $CHCl_3$ stock solution of **CBA** was prepared which was dried under vacuum. Then, to the residue were added THF, $CHCl_3$, MeOH, DMSO, and H_2O, respectively, for UV-Vis absorption and emission spectral analysis.

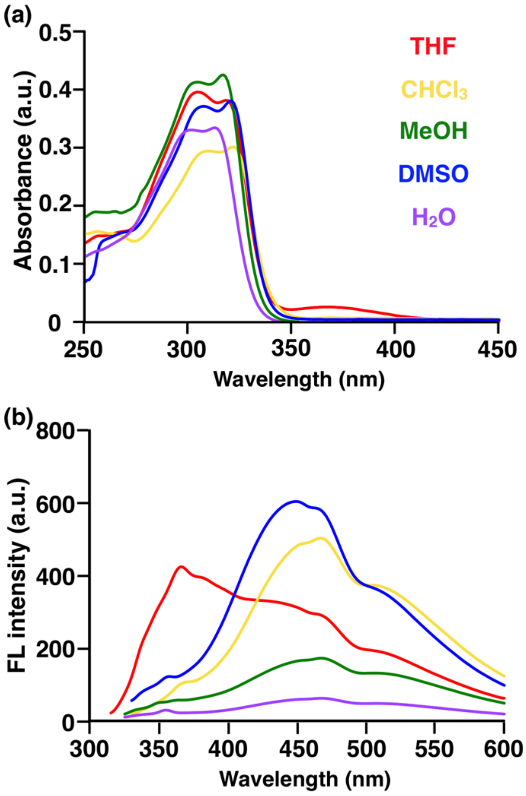

Fig. 2. (a) UV-Vis absorption and (b) emission spectra of **CBA** in various solvents (λ_{ex} = 305 nm (THF), 320 nm ($CHCl_3$ and DMSO), and 315 nm (MeOH and H_2O) before annealing. All measurements were carried out at 5 μM, 20 ºC.

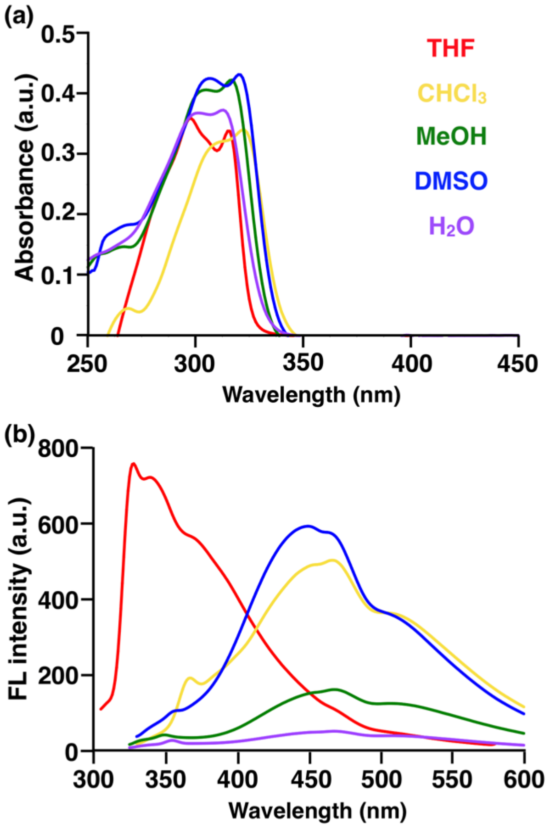

Fig. 3. (a) UV-Vis absorption and (b) emission spectra of **CBA** in various organic solvents (λ_{ex} = 295 nm (THF), 315 nm (MeOH and H_2O) and 320 nm ($CHCl_3$ and DMSO) after annealing at 60 ºC for 30 min. All measurements were carried out at 5 μM, 20 ºC.

The absorption spectra showed a broad band around 310 nm, where the absorption maximum differed depending on solvents (Fig. 2a). As for the emission spectra, the maximum emission bands were observed around 465 nm for the solvents besides THF, which showed the maximum band around 366 nm, with a shoulder around 465 nm (Fig. 2b). Interestingly, after annealing at 60 °C (Fig. 3a), both absorption and emission spectra in THF showed hypsochromic shifts while the those in the other solvents remained substantially unchanged. From these results it is likely that **CBA** forms two kinds of assemblies depending on solvents; one was thermally stabilized in $CHCl_3$, MeOH, DMSO and H_2O, and gave emission bands around 465 nm, while another one was thermally stabilized in THF, and gave emission around 330 nm.

3.2. TEM observation

Based on the above-mentioned spectroscopic studies, we have carried out microscopic

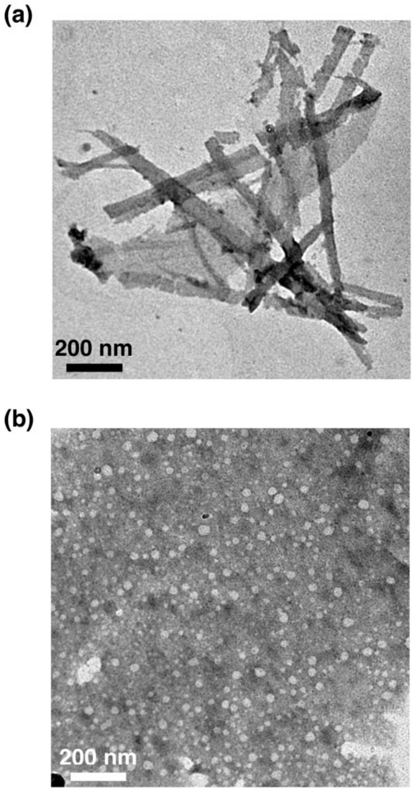

Fig. 4. TEM images of **CBA** prepared in (a) THF (**CBA$_T$**) and (b) $CHCl_3$ (**CBA$_C$**). Both samples were prepared at 100 μM and stained with NANO–WTM (1wt%)

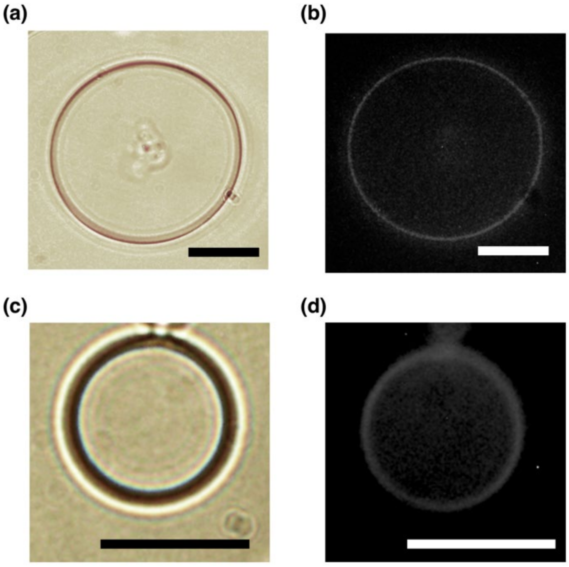

Fig. 5. (a), (c), Phase contrast and (b), (d) and fluorescent microscopic images of (a), (b) **CBA$_T$** and (c), (d) **CBA$_C$**. All samples were prepared as [**CBA**/DOPC] = 1/200 in milliQ, λ_{ex} = 330 nm–385 nm, λ_{em} = 420 nm. Scale bars indicate 10 μm.

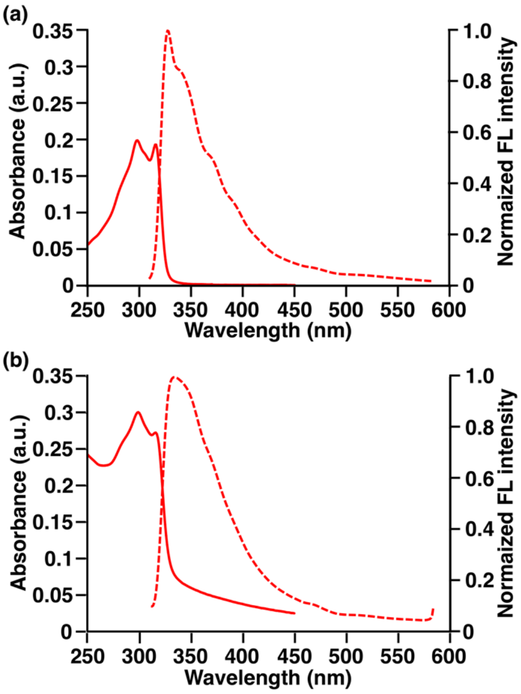

Fig. 6. UV-Vis absorption spectra (solid lines) and normalized emission spectra (dashed lines) of (a) **CBA**$_{\mathrm{T}}$ in THF, λ_{ex} = 298 nm, (b) **CBA**$_{\mathrm{T}}$ in DOPC LUVs solution, λ_{ex} = 299 nm. Measurements were carried out at (a) [**CBA**] = 5 µM, and (b) [**CBA**] = 2.5 µM, [DOPC] = 200 µM, in 20 mM HEPES, 50 mM NaCl buffer, pH 7.1, at 20 ºC.

observations of **CBA** assemblies prepared in THF (**CBA**$_{\mathrm{T}}$) and CHCl$_3$ (**CBA**$_{\mathrm{C}}$), which showed different emissions as shown in Fig. 3. Considering the possibility that **CBA** could form assemblies by both kinetic and thermodynamic controls, we dissolved **CBA** in THF and CHCl$_3$ and annealed the resulting solutions at 60 ºC respectively for complete formation of each assembly. Importantly, TEM observation of **CBA**$_{\mathrm{T}}$ and **CBA**$_{\mathrm{C}}$ revealed differences in morphology (Fig. 4): **CBA**$_{\mathrm{T}}$ showed sharp-edged and ribbon-like structures (Fig. 4a) while **CBA**$_{\mathrm{C}}$ showed small spherical aggregates (Fig. 4b). From these observations, it is likely that the assembly formed in THF has relatively higher order compared to that prepared in CHCl$_3$.

3.3. Incorporation of **CBA**$_{\mathrm{T}}$ and **CBA**$_{\mathrm{C}}$ into lipid bilayer membranes

Since preparation of two different assemblies could be controlled by proper choice of solvents, we investigated the possibility whether these two assemblies could be transferred into lipid bilayer membranes. Thus we prepared **CBA**$_{\mathrm{T}}$ and **CBA**$_{\mathrm{C}}$ in THF or DMSO, respectively, and added them to the vesicles. In this case, DMSO was used to prepare **CBA**$_{\mathrm{C}}$ instead of CHCl$_3$, due to its miscibility with water.

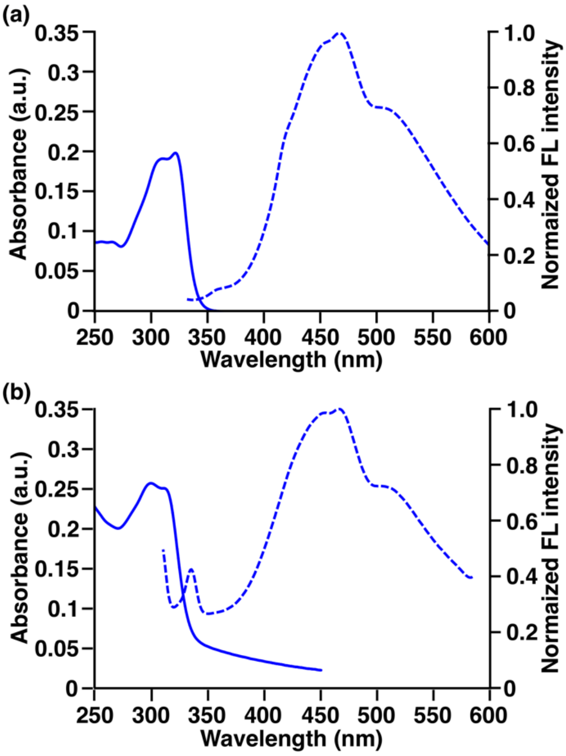

Fig. 7. UV-Vis absorption spectra (solid lines) and normalized emission spectra (dashed lines) of (a) **CBA**$_{\mathrm{C}}$ in CHCl$_3$, λ_{ex} = 322 nm, and (b) **CBA**$_{\mathrm{C}}$ in DOPC LUVs solution, λ_{ex} = 301 nm. Measurements were carried out at (a) [**CBA**] = 5 µM, and (b) [**CBA**] = 2.5 µM, [DOPC] = 200 µM, in 20 mM HEPES, 50 mM NaCl buffer, pH 7.1, at 20 ºC.

Incorporation of **CBA**$_{\mathrm{T}}$ and **CBA**$_{\mathrm{C}}$ into the lipid bilayer membranes was confirmed by microscopic observations of vesicles after addition of **CBA**$_{\mathrm{T}}$ and **CBA**$_{\mathrm{C}}$. To giant unilamellar vesicles (GUVs) of DOPC, was added **CBA**$_{\mathrm{T}}$ in THF or **CBA**$_{\mathrm{C}}$ in DMSO, respectively. In the phase contrast and fluorescent microscopic images shown in Fig. 5, circular objects corresponding to GUVs were clearly observed, indicating that **CBA**$_{\mathrm{T}}$ and **CBA**$_{\mathrm{C}}$ were both successfully incorporated into the lipid bilayer membranes.

Importantly, the emission spectra of **CBA**$_{\mathrm{T}}$ in DOPC LUVs showed little difference from that in THF (Figs. 6a, b, dashed lines). The emission maximum wavelength was 333 nm in DOPC LUVs, which was very close to that in THF (328 nm). This result strongly indicates that **CBA**$_{\mathrm{T}}$ was maintained within the lipid bilayer membranes. Similarly, emission spectra of **CBA**$_{\mathrm{C}}$ in DOPC LUVs was very similar to that in CHCl$_3$ (Figs. 7a, b, dashed lines), where the emission maximum wavelength was 466 nm in both cases. Therefore,

CBA$_C$ was also preserved within the lipid bilayer membranes. From these results, it is strongly suggested that the assemblies of **CBA** formed in solvents could successfully be transferred to in the lipid bilayer membranes.

4. Conclusion

The self-assembling properties of multiblock amphiphile **CBA** is unique in that the structure formed in $CHCl_3$ gradually changed into other forms in THF as shown in Figs. 2 and 3. This apparently slow conversion process between two states likely allows transfer of **CBA$_T$** and **CBA$_C$** into lipid bilayer membranes, respectively. These findings suggest a possibility of controlling supramolecular architectures in lipid bilayer membranes through kinetically controlled self-assembling processes in solution [25].

Acknowledgement

The authors thank Materials Analysis Division, Open Facility, Tokyo Institute of Technology for TEM and Open Research Facilities for Life Science and Technology, Tokyo Institute of Technology, for fluorescence spectroscopy. This work was supported by Grand-in-Aid for Scientific Research on Innovative Areas “Molecular Engine (No.8006)” (18H05419 and 18H05418 to KK) and Grant-in-Aid for Scientific Research B (19H02831 to KK).

References

1. Y.-M. Legrand and M. Barboiu, *Chem. Rec.* 2013, **13** (2013) 524.
2. B. Gong and Z. Shao, *Acc. Chem. Res.*, **46** (2013) 2856.
3. S. Matile, A. Vargas Jentzsch, J. Montenegro, and A. Fin, *Chem. Soc. Rev.*, **40** (2011) 2453.
4. T. M. Fyles, *Chem. Soc. Rev.*, **36** (2007) 335.
5 C. P. Wilson and S. J. Webb, *Chem. Commun.*, (2008) 4007.
6 P. Barton, C. A. Hunter, T. J. Potter, S. J. Webb, and N. H. Williams, *Angew. Chem., Int. Ed.*, **41** (2002) 3878−3881.
7. M. M. Tedesco, B. Ghebremariam, N. Sakai, and S. Matile, *Angew. Chem., Int. Ed.*, **38** (1999) 540.
8 R. Ohtani, K. Kawano, M. Kinoshita, S. Yanaka, H. Watanabe, K. Hirai, S. Futaki, N. Matsumori, H. Uji-i, M. Ohba, K. Kato, and S. Hayami, *Angew. Chem., Int. Ed.*, **59** (2020) 17931.
9 R. Ohtani, M. Inukai, Y. Hijikata, T. Ogawa, M. Takenaka, M. Ohba, and S. Kitagawa, *Angew. Chem., Int. Ed.*, **54** (2015) 1139.
10 S. Tomas and L. Milanesi, *Nat. Chem.*, **2** (2010) 1077.
11 K. Bernitzki and T. Schrader, *Angew. Chem., Int. Ed.*, **48** (2009) 8001.
12. S. Grassi, P. Giussani, L. Mauri, S. Prioni, S. Sonnino, and A. Prinetti, *J. Lipid Res.*, **61** (2020) 636.
13. Y. G.Zhao and H. Zhang, *Dev. Cell*, **55** (2020) 30.
14. C. Hayden, J. S. Hwang, E. A. Abate, M. S. Kent, and D. Y. Sasaki, *J. Am. Chem. Soc.*, **131** (2009) 8728.
15. Y. Shimizu, K. Sato, and K. Kinbara, *Chem. Commun.*, **57** (2021) DOI: 10.1039/D1CC01111A.
16. R. Sasaki, K. Sato, K. V. Tabata, H. Noji, and K. Kinbara, *J. Am. Chem. Soc.*, **143** (2021) 1348.
17. T. Muraoka, D. Noguchi, R. S. Kasai, K. Sato, R. Sasaki, K. V. Tabata, T. Ekimoto, M. Ikeguchi, K. Kamagata, N. Hoshino, H. Noji, T. Akutagawa, K. Ichimura, and K. Kinbara, *Nat. Commun.*, **11** (2020) 2924.
18. T. Muraoka, K. Umetsu, K. V. Tabata, T. Hamada, H. Noji, T. Yamashita, and K. Kinbara, *J. Am. Chem. Soc.*, **139** (2017) 18016.
19. T. Muraoka, T. Endo, K. V. Tabata, H. Noji, S. Nagatoishi, K. Tsumoto, R. Li, and K. Kinbara, *J. Am. Chem. Soc.*, **136** (2014) 15584.
20. T. Muraoka, T. Shima, T. Hamada, M. Morita, M. Takagi, K. V. Tabata, H. Noji, and K. Kinbara, *J. Am. Chem. Soc.*, **134** (2012) 19788.
21. T. Muraoka, T. Shima, T. Hamada, M. Morita, M. Takagi, and K. Kinbara, *Chem. Commun.*, **47** (2011) 194.
22. R. Li, T. Muraoka, and K. Kinbara, *RSC Adv.*, **10** (2020) 25758.
23. R. Li, T. Muraoka, and K. Kinbara, *Chem. Commun.*, **53** (2017) 11662.
24. M. Mori, K. Sato, T. Ekimoto, S. Okumura, M. Ikeguchi, K. V. Tabata, H. Noji, and K. Kinbara, *Chem. Asian J.*, **16** (2021) 147.
25. M. Wehner and F. Würthner, *Nat. Rev. Chem.,* **4** (2020) 38.

Journal of Photopolymer Science and Technology
Volume 34, Number 2 (2021) 167－174 ©2021SPST

Oriented Nanowire Arrays with Phthalocyanine – C_{60} Multi-Heterojunctions

**Masaki Nobuoka,[1] Koshi Kamiya,[1] Shugo Sakaguchi,[1] Akira Idesaki,[2] Tetsuya Yamaki,[2]
Tsuneaki Sakurai,[3] and Shu Seki[1]***

[1] *Department of Moecular Engineering, Graduate School of Engineering, Kyoto University,*
Nishikyo-ku, Kyoto 615-8510, Japan.
[2] *Department of Advanced Functional Materials Research, National Institutes for Quantum and Radiological*
Science and Technology (QST), Takasaki, Gunma 370-1292, Japan
[3] *Faculty of Molecular Chemistry and Engineering, Kyoto Institute of Technology,*
Sakyo-ku, Kyoto 606-8585, Japan.
E-mail: seki@moleng.kyoto-u.ac.jp

One dimensional nanowires systems with programmed multi-heterojunction along their axes have been presumed as an ideal nanomaterials platform for quantum confinements exhibiting novel electronic/photonic functions. Herein we have successfully produced free-standing nanowires with multi-heterojunctions of which spatial alignments are perfectly under control on a substrate by a facile protocol referred to as Single Particle Triggered Linear Polymerization method. Uniform nanowires were well-vertically aligned on substrates with tightly bound bases, and represented by the sequential bottom-up of ~ 10 nano-segments from copper phthalocyanine and Buckminster fullerene molecules. Efficient polymerization/crosslinking reactions with high enough *G* values of 20-40 (100 eV)$^{-1}$ were rationalize the formation of the nano-segments with significant changes in their radial thickness. Although the released energy density by the employed high energy charged particle was extremely high, which is presumed from the value of linear energy transfer of 1 – 1.4 ×10^4 eV nm^{-1}, however electronic and Raman spectroscopies confirmed clearly that the nano-segments in nanowires reflected well opto-electronic characteristics of molecules at least the outer boundaries, suggesting the future application of the present multi-heterojunction systems as magneto-optical nanomaterials. We are able to make our own choices of the molecules with designed electronic states, and program them to 0-1 dimensional nanomaterials with sequential connection along a direction by the present technique.

Keywords: nanowire, high-energy particle, heterojunction, solid-state polymerization, free-standing

1. Introduction

Dot, wire, and plane-like structures of metals/semiconductor materials with nm-sizes have been attracted many attentions in view of their deserving as interesting platforms for quantum confinements [1, 2]. Single-nm scaled structures of the above 0-2 dimensional systems have been predicted as prerequisite for giving discrete energy levels of electrons, spins, or the other elementary excitations, and their deviations in sizes are crucial for recognizing outputs from the systems clearly represented by quantum confinements [3]. 2D quantum well systems with heterostructures have been widely investigated as a new class of materials and devices exhibiting novel electronic and photonic functions till date. Since the last decade, 1D nanowire systems have been developed with hetero-interfaces of coaxial core-shell manners

---

Received March 26, 2021
Accepted May 8, 2021

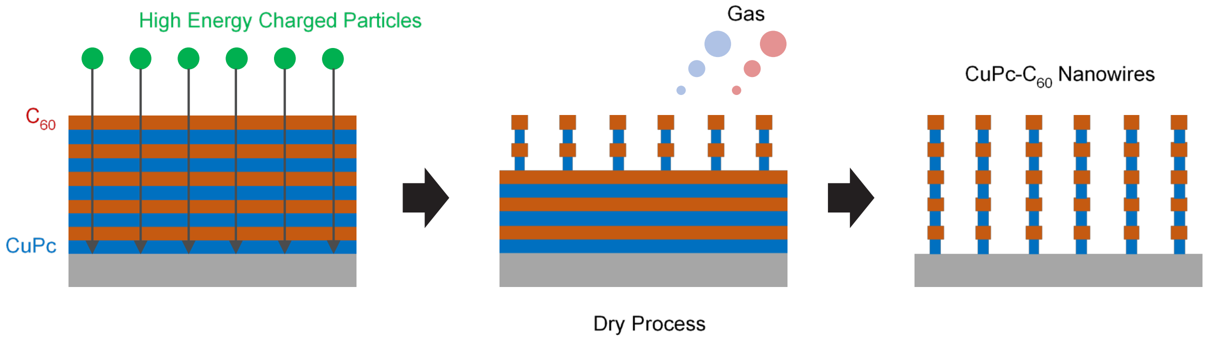

Fig. 1. Schematic illustration of isolation process of CuPc–C_{60} nanowires prepared by STLiP method. Sublimation of organic molecules is used in the dry process.

[4, 5]. In particular, exciton confinements in the quantum well exhibited efficient amplification of light output from the structures and lasing of the systems [6]. The low-dimensional 1D nature of nanowires are, however, not reflected by the hetero-interface of the "core-shell" structure: an extension of 2D quantum well structures embedding onto the surfaces of 1D nanowires.

Quantum confinement effects become explicit in the lower dimensional systems of quantum dot and/or quantum wires where structural boundaries, and hence the potentials define the density of states more discretely in phase space [7]. Resulting unique properties from heterojunctions among low dimensional quantum dots/nanowires are widespread over the above photonic applications. For instance, electron injection into heterojunction structure of semiconductor quantum dots is affected significantly by the interplay of spin and repulsive Coulombic interaction between two adjacent electrons. By tuning the sizes of quantum dots, hence Coulombic interaction, the interplay leads non-magnetic metallic – antiferromagnetic Mott insulator transition of the system [8, 9]. Upon light excitation of the heterojunction systems, photogenerated excitons confined in two adjacent quantum dots interact with each other, resulting biexciton states predicted to have a significant increase in their binding energy [10, 11].

To elucidate these unique properties originated from quantum confinements, spatial alignment of quantum dots/quantum wires is necessary for statistical analysis because electrical conductivity and/or binding energy of excitons can only be detected by unidirectional electron transport in their translational motion or light output under modulated external magnetic field along a direction [12, 13]. This has been the case making it hard to explore quantum confinement effects in low dimensional nanostructures.

In contrast to the progressive studies on inorganic nanowires, macromolecular systems as well as supramolecular polymerization have been the center for the 1D nanostructure formation based on organic molecules that enable us to embed functionalities on their surfaces by chemical processes [14-16]. Herein polymerization reactions and/or supramolecular interactions limit the resulting 1D structure of the systems, and their functions have been often in debates after formation of the structure. In addition, our "STLiP" technique allows us to fabricate 1D structure from a variety of small organic molecules with designated optoelectronic properties [17-19].

In STLiP protocol, high energy charged particle is employed as a reaction source, and injected into the condensed phases of organic molecules. The released energy from a particle along its trajectory is transferred efficiently onto the molecules, giving reactive intermediated to promote polymerization reactions as well as crosslinking reactions in a confined cylindrical small spatial area [20-22]. The molecules included in the area are immobilized with a considerable increase in their molecular weight, remaining in the condensed phases after successive sublimation processes. The length of nanowires reflects perfectly the initial thickness of the films because of the orthogonal trajectory of a particle with negligible change in its momentum against the substrate supporting the films [23, 24]. This also define explicitly the alignment of nanowires as orthogonal to the substrate. One principle requisite for STLiP protocol is to facilitate efficient polymerization reactions of the target organic molecules; we can make a free choice to satisfy this requirement in a variety of organic compounds.

We report on alternating heterojunction nanowires using STLiP technique. Distinct nano-segments composed of copper phthalocyanine (CuPc) and C_{60} were clearly visualized and adjoined in one nanowire, confirmed by elemental analysis and representative optical properties of the

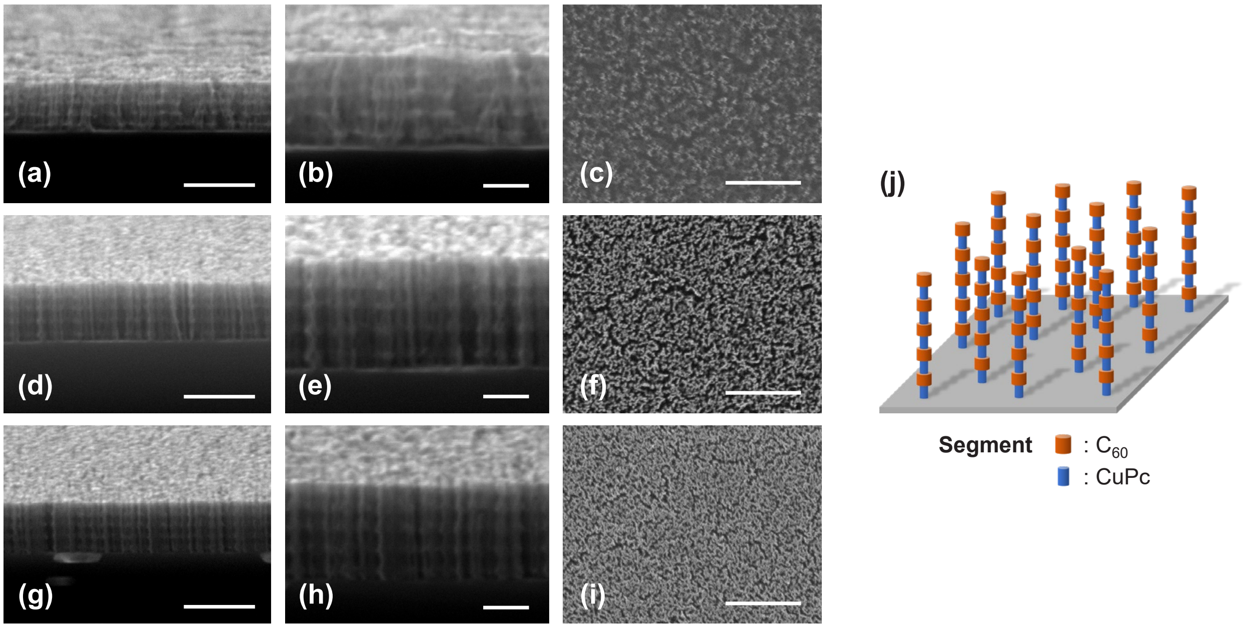

Fig. 2. SEM images of CuPc–C_{60} heterojunction free-standing nanowires ((a, b, d, e, g, h): side view, (c, f, i): top view) and (j) illustration of the nanowires on a Si substrate. The pristine films were prepared by alternating vapor-deposition of CuPc and C_{60}. Nanowires were fabricated by irradiation with 450 MeV ^{129}Xe^{23+} particles at the fluence of (a-c) 1.0×10^{11} cm^{-2}, (d-f) 5.0×10^{11} cm^{-2}, and (g-i) 1.0×10^{12} cm^{-2}, followed by isolation protocol of sublimation (dry process). Scale bars: (a, d, g) 300 nm, (b, e, h) 100 nm, and (c, f, i) 500 nm.

molecules. As demonstrated herein, we can program multi-heterojunction structures in 1D nm-sized cylindrical spaces from any organic molecules and control perfectly their alignments with an interplay of free-standing nature and extraordinarily high aspect ratio, which will be powerful candidates as future structural optical/electronic 1D nanomaterials.

2. Experimental

2.1. Chemicals

Both Buckminster fullerene 60 (C_{60}) and copper(II) phthalocyanine (CuPc) were purchased from Tokyo Chemical Industry Co. Ltd. and used without further purification.

2.2. Nanowire fabrication and observation

Si and quartz substrates were cut into 1.5 cm^2 and 1.0 cm^2 square, respectively, sonicated in 2-propanol, dried, and treated with O_2 plasma prior to the use by VACUUM DEVICE Ltd. model PIB-20 ion bombarder. C_{60} and CuPc were deposited on the substrate in a vacuum at a rate of 0.2–0.4 Å s^{-1} by using Kenix model KXV-250. The thickness of the films was evaluated by a Bruker Co. model Multimode 8 atomic force microscopy (AFM). 450 MeV ^{129}Xe^{23+} particles were generated from a cyclotron accelerator at National Institutes for Quantum and Radiological Science and Technology, Takasaki Advanced Radiation Research Institute. The prepared thin films were exposed to the above ion beam in a vacuum chamber (< 1×10^{-4} Pa). The number of incident particles was controlled at 10^{11}–10^{12} particles cm^{-2} to prevent severe overlapping of the ion tracks. Then, the irradiated films were further cut into small pieces, and developed by sublimation of the unreacted area using JEOL Ltd. model JFE-400 vacuum evaporator (< 1×10^{-3} Pa). The sublimation temperature was measured directly with a thermocouple on a tungsten board on which the substrate/samples were placed. The sizes and shapes of the isolated nanowires were characterized by using JEOL Ltd. model JSM-7001F Scanning Electron Microscope (SEM).

2.3. Spectroscopy measurements

Energy Dispersive X-ray spectroscopy (EDX) spectrum was measured on HITACHI Ltd. model Regulus 8220 SEM, equipped with HORIBA. Ltd. model X-MaxN80 011 silicon drift x-ray detector. Electronic absorption spectra were recorded on JASCO V-570 spectrometer. Raman spectra were measured on JASCO NRS-4100 spectrometer.

3. Results and Discussion

We have chosen two representative p/n type organic molecules as the target: CuPc and C_{60}, respectively. STLiP protocol was applied for

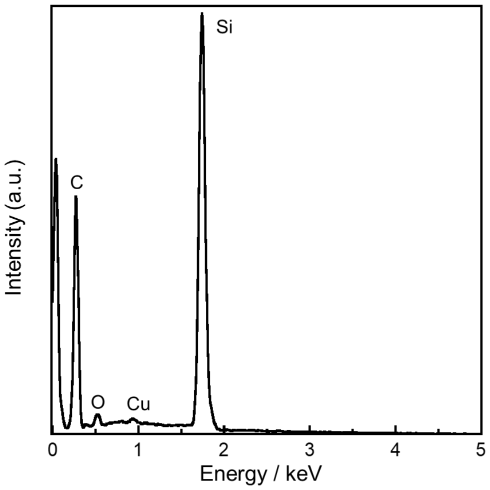

Fig. 3. EDX spectrum of CuPc–C_{60} nanowires on Si substrates. Nanowires were fabricated by irradiation with 450 MeV $^{129}Xe^{23+}$ particles at the fluence of 1.0×10^{12} cm^{-2}, followed dry process development. The electron acceleration voltage was 5 kV. The peak of Cu can be confirmed.

multiple Layer-by-Layer (LbL) films of these compounds. CuPc has a planner molecular core with delocalized π-conjugated system, facilitating molecular stacking through π-π interaction, often giving columnar structures which have been demonstrated by their characteristic condensed phases of anisotropic discotic liquid crystalline phases [25]. In contrast the shape of C_{60} is spherical and numerous previous works have been focusing particularly onto formation of 1-3D structure by polymerizing 0D C_{60} molecules [26]. C_{60}-based 1D nanowire formation was previously reported [27], in contrast, this is the first report on 1D nanostructures with heterojunctions between anisotropic disk-shaped 2D molecules and isotropic spherical 0D molecules. Fig. 1 is schematic illustration of STLiP technique employed in this work represented by three simple steps: fabrication of target LbL organic films of successive vacuum deposition of 10 layers of CuPc and C_{60} (CuPc–C_{60}) in total at 200 nm thick, irradiation of high energy particles passing through the target, sublimation of unreacted molecule for removal leading to free-standing nanowires on the surfaces (all-dry process).

Swift heavy charged particles of 450 MeV $^{129}Xe^{23+}$ were irradiated to the LbL film in a vacuum chamber (<10^{-4} Pa) at the fluence of 1×10^{11}–1×10^{12} cm^{-2}, followed by isolation of resulting nanowires by the dry process. Solvent-based wet-development processes are applicable in this case to isolate the nanowires on the substrate by dissolving unreacted parts of the films: this is the common protocol not only in the present nanowire formation but also in nanolithography processes [28]. The wet process, however, causes significant impacts on the morphology of nanowires via strong dissolution effects of molecules and surface tension of solvents themselves, which often leads the nanowires knocked-down on the substrate being no longer free-standing [19, 27]. Besides, wet process is unapplicable to the molecular systems exhibiting the lower solubility against the solvents employed with low enough boiling points and viscosity considering the successive drying of the system. The present all-dry process needs no solvents, where we can address all the issues raised in wet processes with minimized impacts on the morphology and alignments of nanowires [19]. We set temperatures at ~560 K for the sublimation of C_{60} and CuPc in LbL films under vacuum (< 10^3 Pa). The sublimation temperature of mono-layer C_{60} or CuPc as ~560 and ~480 K, respectively. The equivalent sublimation temperatures of both compounds with small mismatch of ~80 K is advantageous for the sublimation process of LbL binary molecular system, because the large mismatch tends to cause selective vaporization of one component with the lower sublimation temperature, leading to accelerated valorization of the component giving the bubbles in underlayers and hence collapsing of the structures.

Bi- or multi-layered polymer films gave successfully multi-segment polymer nanowires by single particle nanofabrication technique through efficient crosslinking reactions and gelation promoted in each polymer layer [19, 29, 30]. Wet process was only the choice for isolation (development) of the multi-segment nanowires via dissolution of uncrosslinked polymer fractions, and 2D images of nanowires lying on the substrate were clearly visualized in the case. Pristine C_{60} as well as unsubstituted CuPc are both showing low solubility against most of all solvents, thus all-dry process is the best for efficient removal of unreacted parts of molecules. Resulted nanowires isolated by the process are clearly visualized in Fig. 2 as SEM images with high enough contrast reflecting encapsulation of Cu only in CuPc-based segments. Note that all the wires are free-standing on the substrate in spite of their overwhelming aspect ratio > 30; this is in striking contrast to the conventional nanolithography techniques not to realize free-standing nanostructures with high aspect ratio of ~ 10 even with development process using super critical fluids [31]. It is also clear that the length of nanowires is uniform completely, which reflects well the initial total thickness of LbL films. Given

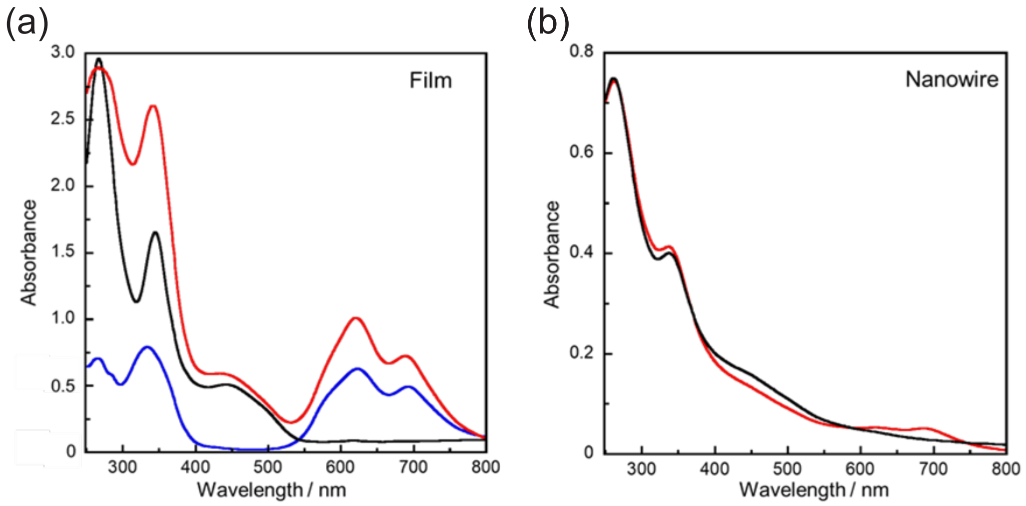

Fig. 4. Electronic absorption spectra of (a) pristine films and (b) nanowires ((blue) CuPc, (black) C_{60}, and (red) CuPc–C_{60}). The film of CuPc or C_{60} was prepared by depositing them on quartz substrates at 100 nm thick respectively. The nanowires were fabricated by irradiation with 450 MeV $^{129}Xe^{23+}$ particles at the fluence of 5.0×10^{11} cm^{-2}, followed by dry process development.

that the particle trajectories are perfectly orthogonal to the substrate plane and distribute randomly, the top-view images in Fig. 2 confirm well isolation of nanowires free from bundled structures upon fluence of particles $< \sim10^{11}$ cm^{-2}.

Clear contrast between each segment in the SEM images is also helpful to recognize the components due to electron-rich Cu incorporation in CuPc segment (bright tone) and electron-deficient all carbon segment (dark), and the significant changes in the radial thickness (cross-sectional size) is also visualized in these images. The efficiency of the cross-linking reaction depends strongly on materials against swift heavy ion irradiation, presumably showing significantly higher value in C_{60} than CuPc because of efficient neutral radical mediated chain reactions. This is the case giving the thicker radial thickness of segment even in one single isolated nanowire with multi-segments.

The radial thickness of nanowire can be theoretically accessible in terms of deposited energy density in an ion track by swift heavy ions. Given that simple polymerization/crosslinking reactions proceed at boundary surface of a nanowire, it is necessary to induce one crosslinking point per one polymer unit for macromolecular gelation, hence perfect immobilization of organic molecules. Radial size (r) of a nanowire is derived from requisite density of crosslinks which is presumed to be correlate linearly to deposited energy density within an ion track. The correlation can be given by crosslinking efficiency G (number of crosslinks produced per 100 eV absorbed energy by an organic medium), and thus r is represented by:

$$r^2 = \frac{LET\cdot G\cdot M}{400\pi d N_{\mathrm{A}}}\left(\ln\frac{e^{1/2}r_{\mathrm{p}}}{r_{\mathrm{c}}}\right)^{-1} \qquad (1),$$

where M, d, and N_A are molecular weight, density of the target material, and Avogadro’s number, respectively. r_c and r_p are radial regimes of energy deposition area referred to as “core” and “penumbra”, determined respectively by the momentum of an incident particle. The former is defined by the region where energy is directly received by the target matter from a particle passing through, and the latter is the region where the energy was deposited by the first knocked-out electrons via ionization process caused by an incident particle: according to equipartition theorem the total energy deposited in the “core” or ”penumbra” regions is well-branched each other. The values of Linear Energy Transfer (LET) are calculated with density of respective molecules in condensed phases derived from single crystal structures of C_{60} and CuPc, giving 14300 eV nm^{-1} and 10000 eV nm^{-1}, respectively for 450 MeV $^{129}Xe^{23+}$ particle. Polymerization reactions of C_{60} molecules have been of interests and reported in not only in solution but also in condensed phases. The reactions occur at multiple cites of spherical surface of a C_{60} molecule, and isotropic growth of polymerized chains [27] ; this is advantageous to promote crosslinking reactions of resulting polymer chains, and reflected by the unusually high G value of polymerization/crosslinking reaction in C_{60} as 35.3 $(100\ eV)^{-1}$. In

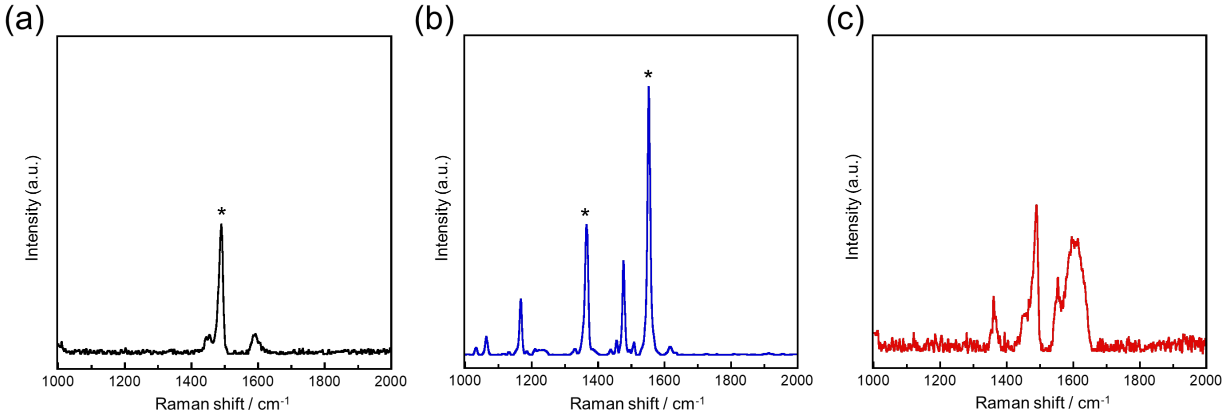

Fig. 5. Raman spectra of (a) C_{60} film, (b) CuPc film, and (c) CuPc–C_{60} nanowires on Si substrates. The film of CuPc or C_{60} was prepared by depositing them on Si substrates at 100 nm thick respectively. CuPc–C_{60} nanowires were fabricated by irradiation with 450 MeV $^{129}Xe^{23+}$ particles at the fluence of 5.0×10^{11} cm^{-2}, followed by dry process development. The characteristic peaks represent A_g mode (1470 cm^{-1}) of (a) C_{60}, and (b) A_{1g} mode (1336 cm^{-1}, 1552 cm^{-1}) of CuPc.

contrast, a CuPc molecule has heterocyclic structure similar to tetraphenylporphyrin (TPP) which shows relatively the lower G value of 25.7 $(100\ eV)^{-1}$ even with introduction of reactive groups in their periphery [32] ; this is the case giving the smaller r visualized for segments based on CuPc in Fig. 2.

Major contribution from CuPc molecules to the thinner segments was confirmed by EDX spectrometry with characteristic X-rays emission from Cu as an index (Fig. 3). The average length of the present free-standing nanowires was ~200 nm and the segments of CuPc distribute in depth of 10-200 nm. X-rays emission from the underlayers is crucial to confirm the presence of Cu atom in the segment, and thus EDX analysis with electron accelerated at 5 keV was employed in the present case rather than XPS: the former we can expect the deeper penetration length up to ~ 400 nm [33], covering entire length of nanowires in contrast to the higher selectivity for surface atoms in XPS measurements. The spectra is shown in Fig. 3, confirming the presence of Cu in the present free-standing nanowire systems.

The estimated energy density in an ion track reaches up to >1 keV nm^{-3} at the center core, and this is high enough to cause severe damage in chemical structure of organic molecules. Preserving the molecular structures of both CuPc and C_{60} was examined by electronic absorption as well as Raman spectroscopies. Nanowires could be also formed on transparent quartz substrates, and the free-standing nanowires on SiO_2 were used for above optical spectroscopies with films of pristine CuPc or C_{60} at 100 nm thick as references. From the absorption spectra, it can be seen that the absorption spectra of the C_{60} thin film [34] and the CuPc thin film [35] are almost the same as those in the literature, respectively, and that the spectra of the LbL films are the sum of these spectra (Fig. 4a). The broad spectrum was observed in Fig. 4b for single-segment nanowires based on C with weak signature of near-UV characteristic peaks of C_{60}. It is noteworthy that Q-bands electronic absorption at 620 and 690 nm, characteristic of phthalocyanine rings, is evident as a differentiate in spectra from multi-segment nanowires to C_{60} single-segment C_{60} one. The relative peak intensity between C_{60} characteristic absorption bands to the Q bands of CuPc in nanowires is lower significantly than that of a LbL film before irradiation, which is due to the dramatic change in the radial thickness segments of C_{60} and CuPc nanowires: the latter is significantly small, impacting more in the relative amounts of molecules in the volume.

Raman spectroscopy is a powerful tool to detect vibrational modes specific to the molecules with extremely high sensitivity [36], and thus used for the detection of the modes in CuPc–C_{60} nanowires. The reference Raman spectra of pristine C_{60} and CuPc films is displayed in Fig. 5(a) and (b) respectively. The characteristic peaks of specific vibrational modes are also indicated in Fig. 5(a) and (b). A peak at 1467 cm^{-1} is characterized by a symmetric vibrational mode of type A_g [37], and the CuPc peaks at 1341 and 1467 cm^{-1} can be assigned to symmetric and antisymmetric vibrations, respectively, of A_{1g} modes [38]. The characteristic peaks were observed clearly in the nanowires with high enough resolution. This is suggestive of the cage structure of C_{60} and the planar conjugated ring structure of CuPc preserving in the nanowires after high energy charged particle irradiation and even after subsequent sublimation processes at high temperature. In contrast the high frequency peak of CuPc becomes broad significantly in the spectrum recorded for nanowires, which may be due to the denaturation of CuPc during Raman spectroscopy measurement with high extinction coefficient for the excitation light source at 532 nm. Chemical post-functionalization of polymer-based nanowires has been realized via active reaction cites on their surfaces [39], and the presence of CuPc ring structures as well as C_{60} cages can be utilized as bridgeheads for the subsequent modification of the present nanowire systems with maximized active surfaces exposed by the free-standing nature.

Conclusion

Multi-heterojunction nanowires of p/n type organic semiconductor molecules were successfully fabricated by STLiP method applied for LbL films of binary organic molecules in their condensed phases: a unique protocol to produce programmed 1D nanostructures. The nanowires were supported with firm basis on a substrate, holding their vertical alignment. The length of the nanowires was uniform reflecting trajectory of a high energy particle; an energy source of chemical reactions to form the nanowire. In addition, the spatial distribution of nanowires were consistent with the hitting points by the particle orthogonally injected into the thin solid films of the molecules, visualizing well the particle trajectories with high spatial resolution. Nanowires composed of sequential multi-segments of C_{60} and CuPc were confirmed using not only SEM images but also electronic absorption and/or Raman spectroscopy techniques. In our STLiP method, multi-heterojunction nanowires can be fabricated simply by irradiating ion beams to LbL films of organic molecules upon our free choices without designing any complicated chemical reactions/physical deposition in conventional organic/inorganic 1D nanostructure fabrication processes; this is a clear advantage of the present STLiP method. Directional order of systems with heterojunctions is a primary requisite for their practical use in device structures because flow of excited energy/charges is expected to be under controlled in the devices, unlikely to the exceptional cases of bulk heterojunctions in solar cells. In this study, we have established successfully a facile method allowing us to arrange the nanowires macroscopically with precisely programmed 0D nanostructures.

Acknowledgements

This work was partly supported by a Grant-in-Aid for Transformative Research Areas (20H05862) from Ministry of Education, Culture, Sports, Science and Technology (MEXT), Japan, Scientific Research (A) (18H03918) and (B) (19KK0134) from the Japan Society for the Promotion of Science (JSPS). High energy charged particle irradiation was carried out at Takasaki Advanced Radiation Research Institute, National Institutes for Quantum and Radiological Science and Technology (QST), Japan, under Facility Shearing Program the Inter-University Program for the Joint Use of JAEA/QST Facilities.

References

1. E. Roduner, *Chem. Soc. Rev.*, **35** (2006) 583.
2. V. V. Pokropivny and V. V. Skorokhod, *Mater. Sci. Eng. C* **27**, (2007) 990.
3. A. D. Yoffe, *Adv. Phys.*, **51** (2002) 799.
4. O. Hayden, A. B. Greytak, and D. C. Bell, *Adv. Mater.*, **17** (2005) 701.
5. B. Tian, X. Zheng, T. J. Kempa, Y. Fang, N. Yu, G. Yu, J. Huang, and C. M. Lieber, *Nature*, **449** (2007) 885.
6. D. Saxena, N. Jiang, X. Yuan, S. Mokkapati, Y. Guo, H. H. Tan, and C. Jagadish, *Nano Lett.*, **16** (2016) 5080.
7. M. Fox and R. Ispasoiu, "*Springer Handbook of Electronic and Photonic Materials*", S. Kasap, and P. Capper, Eds., Springer, Cham 2017, Ch. 40, pp. 1037–1057.
8. R. Ugajin, *J. Appl. Phys.* **76** (1994) 2833.
9. S. Kuamr and V. Tripathi, *Phys. Rev. B*, **102** (2020) 235147.
10. H. Gotoh, H. Kamada, and T. Saitoh, *Appl. Phys. Lett.*, **85** (2004) 3480.
11. X. Xu, D. A. Williams, and J. R. A. Cleaver, *Appl. Phys. Lett.*, **86** (2005) 012103.
12. M. T. Björk, C. Thelander, A. E. Hansen, L. E. Jensen, M. Larsson, L. R. Wallenberg, and L. Samuelson, *Nano Lett.*, **4** (2004) 1621.
13. Z. X. Koong, G. B. Garcia, R. Proux, D. Dalacu, P. Poole, and B. D. Gerardot, *Phys. Rev. Appl.*, **14** (2020) 034011.
14. A. P. H. J. Schenning and E. W. Meijer, *Chem. Commun.*, **26** (2005) 3245.
15. F. J. M. Hoeben, P. Jonkheijm, E. W. Meijer, and A. P. H. Schenning, *Chem. Rev.*, **105** (2005) 1491.
16. S. Yagai, Y. Kitamoto, S. Datta, and B. Adhikari, *Acc. Chem. Res.*, **52** (2019) 1325.
17. Y. Takeshita, T. Sakurai, A. Asano, K. Takano, M. Omichi, M. Sugimoto, and S. Seki, *Adv.*

Mater. Lett., **6** (2015) 99.

18. A. Horio, T. Sakurai, G. B. V. S. Lakshmi, D. K. Avasthi, M. Sugimoto, T. Yamaki, and S. Seki, *Nanoscale*, 8 (2016) 14925.
19. S. Sakaguchi, K. Kamiya, T. Sakurai, and S. Seki, *Quantum Beam Sci.*, **4** (2020) 7.
20. S. Seki, K. Maeda, S. Tagawa, H. Kudoh, M. Sugimoto, Y. Morita, and H. Shibata, *Adv. Mater.*, **13** (2001) 1663.
21. S. Seki, S. Tsukuda, K. Maeda, Y. Matsui, A. Saeki, and S. Tagawa, *Phys. Rev. B*, **70** (2004) 144203.
22. S. Seki, T. Sakurai, M. Omichi, A. Saeki, and D. Sakamaki, "*High-Energy Charged Particles Their Chemistry and Use as Versatile Tools for Nanofabrication*", Springer, Tokyo, 2015, DOI; 10.1007/978-4-431-55684-8
23. A. Chatterjee and J. L. Magee, *J. Phys. Chem.*, **84** (1980) 3537.
24. S. Seki, S. Tsukuda, S. Tagawa, and M. Sugimoto, *Macromolecules*, **39** (2006) 7446.
25. T. Wöhrle, I. Wurzbach, J. Kirres, A. Kostidou, N. Kapernaum, J. Litterscheidt, J. C. Haenle, P. Staffeld, A. Baro, F. Giesselmann, and S. Laschat, *Chem. Rev.*, **116** (2016) 1139.
26. F. Giacalone and N. Martin, *Chem. Rev.*, **106** (2006) 5136.
27. Y. Maeyoshi, A. Saeki, S. Suwa, M. Omichi, H. Marui, A. Asano, S. Tsukuda, M. Sugimoto, A. Kishimura, K. Kataoka, and S. Seki, *Sci. Rep.*, **2** (2012) 600.
28. G. M. Wallraff and W. D. Hinsberg, *Chem. Rev.*, **99** (1999) 1801.
29. M. Omichi, H. Marui, V. S. Padalkar, A. Horio, S. Tsukuda, M. Sugimoto, and S. Seki, *Langmuir*, **31** (2015) 11692.
30. S. Tsukuda, S. Seki, M. Sugimoto, and S. Tagawa, *J. Phys. Chem. B*, **110** (2006) 19319.
31. Y. Liang, C. Zhen, D. Zou, and D. Xu, *J. Am. Chem. Soc.*, **126** (2004) 16338.
32. T. Sakurai, S. Sakaguchi, Y. Takeshita, K. Kayama, A. Horio, M. Sugimoto, T. Yamaki, A. Chiba, Y. Saitoh, L. B. V. S. Garimella, D. K. Avasthi, and S. Seki, *ACS Appl. Nano Mater.*, **3** (2020) 6043.
33. H. G. Paretzke, "*Kinetics of Nonhomogeneous Processes*", G. R. Freeman, Ed., Wiley, New York, 1987, Ch. 3, pp. 89–170.
34. S. Kazaoui, R. Ross, and N. Minami, *Solid State Commun.*, **90** (1994) 623.
35. A. A. M. Farag, *Opt. Laser. Technol.*, **39** (2007) 728.
36. R. L. McCreery, "*Raman Spectroscopy for Chemical Analysis*" J. D. Winefordner, Ed., Wiley, New York 2000, Ch. 1, pp. 1–14.
37. M. S. Dresselhaus, G. Dresselhaus, and P. C. Eklund, *J. Raman Spectrosc.*, **27** (1996) 351.
38. A. J. Bovill, A. A. McConnel, J. A. Nimmo, and W. E. Smith, *J. Phys. Chem.*, **90** (1986) 569.
39. A. Asano, M. Omichi, S. Tsukuda, K. Takano, M. Sugimoto, A. Saeki, and S. Seki, *J. Phys. Chem. C*, **116** (2012) 17274.

Journal of Photopolymer Science and Technology
Volume 34, Number 2 (2021) 175－180 ©2021SPST

Designed, Flexible Electrochromic Display Device with Fe(II)-Based Metallo-Supramolecular Polymer Using Mechanically Etched ITO Film

Masayoshi Higuchi* **and Yukio Fujii**

Electronic Functional Macromolecules Group, Research Center for Functional Materials,
National Institute for Materials Science, 1-1 Namiki, Tsukuba, Ibaraki 305-0044, Japan
**HIGUCHI.Masayoshi@nims.go.jp*

Electrochromic (EC) displays are expected as energy-saving smart windows or digital signages because of the memory property. We succeeded in developing a designed and flexible electrochromic (EC) display device with Fe(II)-based metallo-supramolecular polymer (polyFe) using a mechanically etched ITO film. Mechanical etching an ITO film was performed with a cutting machine having a blade of which length was adjusted so as not to cut off the film. The fabricated EC device was composed of the etched ITO film, a polyFe layer, an electrolyte layer, a nickel hexacyanoferrate layer as the counter material, and another ITO film. The EC device showed unique changes of the display upon applying a voltage of 1.5 V between the two ITO electrodes. It was revealed that the EC changes were controlled by the etching pattern such as a closed circle or the formation of a narrow ITO path.

Keywords: Electrochromic display, Metallo-supramolecular polymer, Mechanical etching, Design, Flexible

1. Introduction

Electrochromic (EC) materials have attracted much attention because of the potential applications such as electrical dimming glass in office and anti-glare mirror in cars [1-7]. Especially, flexible EC devices (ECDs) are expected to expand the application fields to displays or fashion [8-14]. Tungsten oxide and viologens are representative EC materials but, they are not always suitable to the flexible ECDs. Plastic film with an ITO layer (ITO film) is the required component in the flexible ECDs, but the ITO film is not proper to vapor deposition process at high temperature, which is necessary to prepare a layer of inorganic EC materials such as tungsten oxide, because of the low thermal stability. The ITO film is not also appropriate to fabricating ECDs with organic molecules containing viologens, because the flexibility of the ITO films tends to cause leaking a solution of the EC molecule, which is injected to the cell, from the sealed part of the fabricated ECD.

One of the best coating methods on the ITO film at low temperature is spin- or spray-coating a solution of EC material. From the viewpoint, metallo-supramolecular polymers (MSPs) are good candidates as the EC material in flexible ECDs, because the polymers have high solubility in polar solvent such as water and methanol. MSPs are composed of metal ion and multi-topic organic ligand. They are expected to show unique electronic properties because of the electronic interaction between the metal and the ligand [15,16].

Fe(II)-based MSP composed of Fe(II) ion and bis(terpyridyl)benzene (polyFe) shows EC properties triggered by the redox between Fe(II) and Fe(III) (Fig. 1) [17,18].

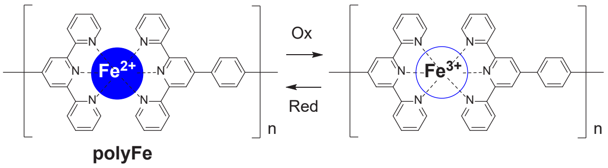

Fig. 1. Redox of polyFe.

PolyFe with Fe(II) (reduced state) has bluish purple color caused by the metal-to-ligand charge

Received April 6, 2021
Accepted April 22, 2021

transfer (MLCT) absorption around 580 nm. The color becomes colorless by electrochemical oxidation of Fe(II) to Fe(III) in polyFe (oxidized state), because of the disappearance of the MLCT absorption. The appearance and disappearance of the MLCT absorption by the redox between Fe(II) and Fe(III) can be explained by the energy diagram as shown in Fig. 2. It is considered that the d electron of Fe(II) contributed to the MLCT absorption is removed electrochemically in the oxidized state of polyFe then the MLCT absorption is vanished.

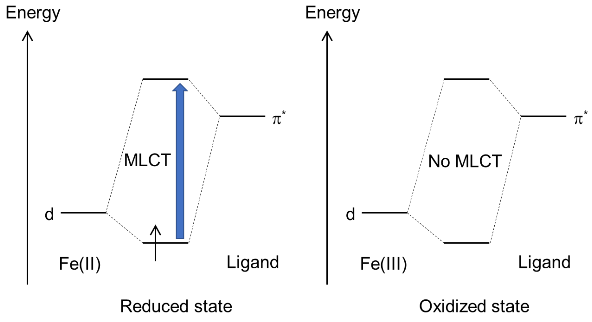

Fig. 2. Energy diagrams of the reduced and oxidized states in polyFe.

A general device structure with MSP is shown in Fig. 3 [19,20]. The electrolyte layer provides anion to the MSP layer when the MSP is oxidized electrochemically. The counter material layer is introduced to accept the complementary redox in the device, which is accompanied with the redox of MSP. Plastic is available as the substrate, because MSPs can be coated on an ITO layer by spin- or spray-coating.

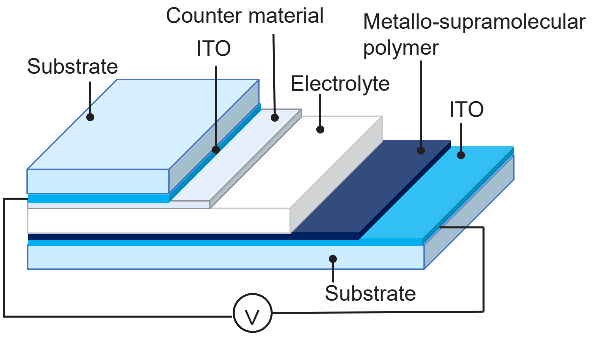

Fig. 3. A device structure of ECDs with MSP.

Here we report fabrication of a designed ECD with polyFe by mechanical etching an ITO film and the EC properties.

2. Experimental

2.1 Chemicals

All reagents and solvents were of high pure analytical grade and used without further purification. PolyFe was purchased from NARD institute, Ltd. Indium tin oxide (ITO)-coated plastic sheets were provided from Nitto Denko Co. Poly(methyl methacrylate) (PMMA) was obtained from Tokyo Chemical Industry Co. (M0088). Battery-grade propylene carbonate (PC), battery-grade LiClO$_4$, and spectrochemical analysis-grade methanol (MeOH) were supplied by Fujifilm Wako Chemicals Co. Nickel hexacyanoferrate (NiHCF) was got from Kanto Chemical Co.

2.2 Equipment

A cutting machine (Roland Desktop Cutter STIKA SV-15) was used to scratch the ITO film (Fig. 4). Spray coater (API-40RA, apeiros) was utilized to prepare thin layers of polyFe and NiHCF on ITO films.

2.3 Gel electrolyte

The gel nonaqueous electrolyte was prepared by the mixing of PMMA, PC, and LiClO$_4$ [PMMA/PC/LiClO$_4$ = 20:20:3 (w/w)] with continuous stirring.

2.4 EC device fabrication

(i) Mechanical etching was performed on an ITO film (size: 10 × 10 cm; film thickness: 150 μm) using the cutting machine with the blade of which length was adjusted so as not to cut off the film. The depth of scratching was controlled to be about 50 μm. The film was used as an electrode of a polyFe layer.

(ii) The mechanically etched ITO film and another ITO film, which was used as the counter electrode, were fixed on flat glass substrates for spray-coating (Fig. 4a).

(iii) A polyFe layer was prepared on the mechanically etched ITO film by spray-coating a methanol solution of polyFe (8.3 g/mL) (Fig. 4b). A NiHCF layer as the counter material was formed on another ITO film by spray-coating an aqueous solution of NiHCF (4.2 mg/mL).

(iv) A prepared gel electrolyte was dropped on the NiHCF layer and the two ITO films with the polyFe or NiHCF layer were stacked face-to-face through the gel electrolyte. Then, the two supporting glass substrates outside were clipped to fix the stacked layers. The assembled device was heated at 98 °C for 5 min. During the heating, the electrolyte became transparent and physically glued the two ITO films. Finally, the flexible ECD with polyFe was obtained by the removal of the supporting glass substrates.

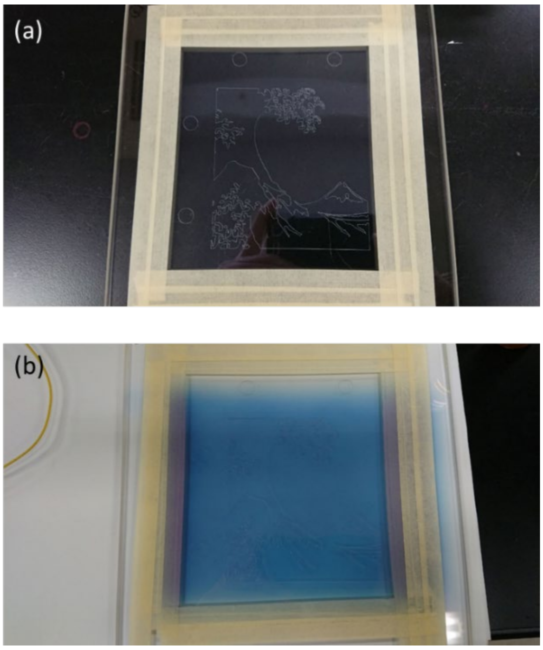

Fig. 4. (a) The mechanically etched ITO film, which was fixed on a glass substrate for spray coating. (b) The spray-coated polyFe layer on the ITO film.

3. Results and discussion

3.1. Strategy

Strategies to display an image on an ECD are shown in Fig. 5.

(a) Drawing an image with MSP

The simplest way to display an image on an ECD is to draw the image with MSP (Fig. 5a). The colored image becomes colorless by applying a voltage between the two ITO electrodes, because the MSP is oxidized electrochemically.

(b) Pasting a designed transparent insulating film

Inserting a transparent insulating film between the MSP layer and the ITO layer is another way to display an image on the ECD. When an oxidative potential is applied to the MSP layer, the part covered with the insulating film cannot change the color, because the anion transfer from the electrolyte layer to the MSP layer is prevented by the insulating film. As the result, the shape of the insulating film appears, because the rest uncovered part becomes colorless (Fig. 5b).

(c) Mechanical etching an ITO film (this work)

Chemical or physical etching is a useful method to process electrode in electronics. In ECDs, mechanical etching (= scratching) the electrode is expected to provide a unique display, because the etched lines prevent electron transfer on the ITO layer (Fig. 5c).

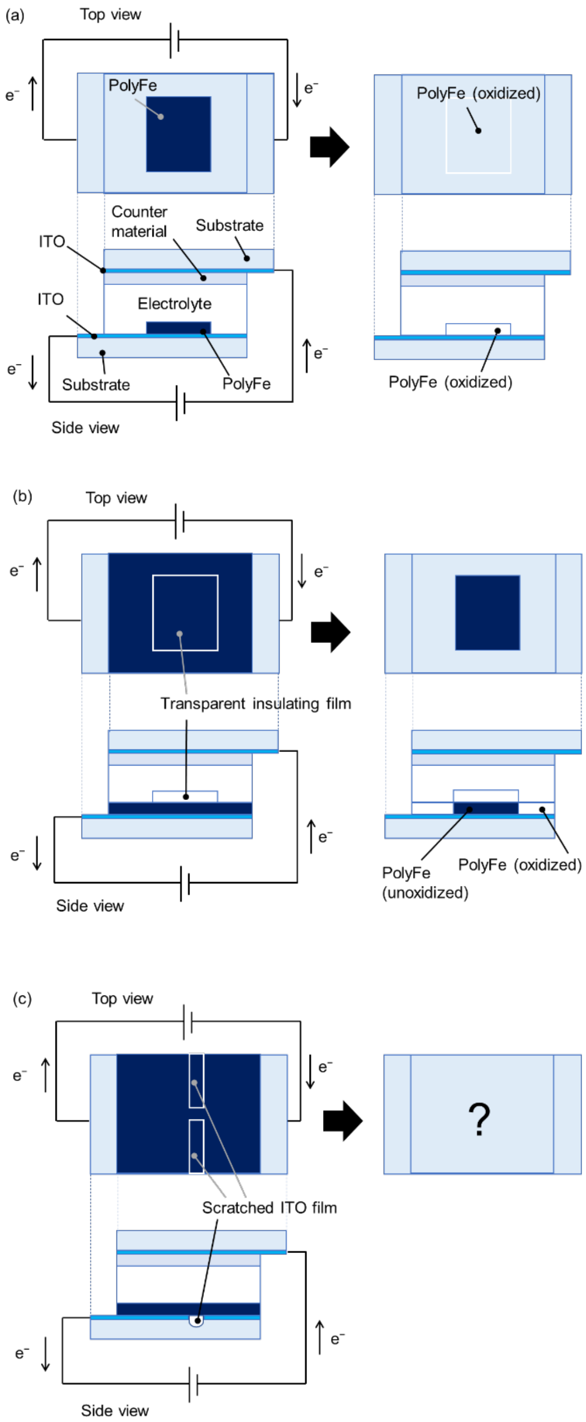

Fig. 5. Strategies to display an image on an ECD. (a) drawing an image with MSP, (b) displaying an image by inserting a transparent insulating film, and (c) this work (scratching an ITO film).

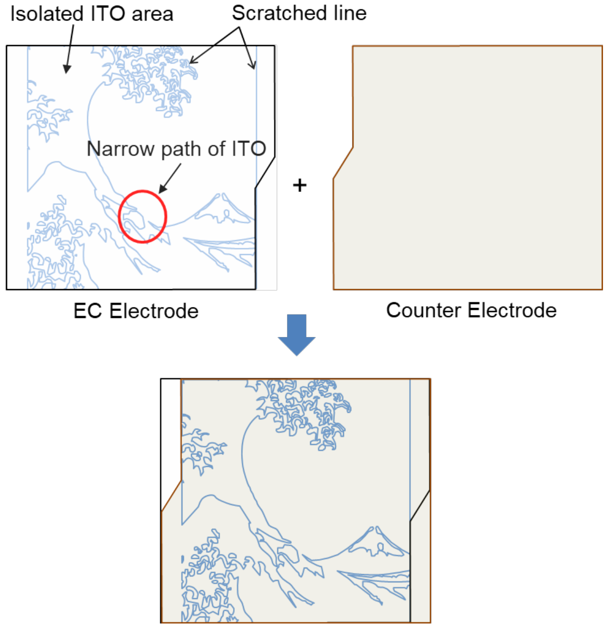

Fig. 6. The fabrication scheme of the designed ECD. An ITO film with an image depicted by scratching the ITO layer, a counter ITO film, and the stacked state.

3.2. Design concept

To display an image on a flexible ECD with polyFe, an ITO film was etched mechanically using a cutting machine (Fig. 6). The ITO layer was separated to the following three area by the etched design.

(a) Totally isolated area, surrounded with the etched line

(b) Area surrounded with the etched line imperfectly, with narrow connecting path to the other area

(c) Area which is not prevented by the etched line until the left edge of the ITO layer, where the voltage is connected.

3.3. EC behavior on the device

It is known that polyFe slightly changes the color by exchanging the counter anion species. The color of the polyFe layer was changed from blue to blueish purple during the device fabrication because the counter anion was exchanged from acetate anion to perchlorate anion in the device (Fig. 7a). Before applying a voltage, the ECD showed the blueish purple color based on the MLCT absorption of the

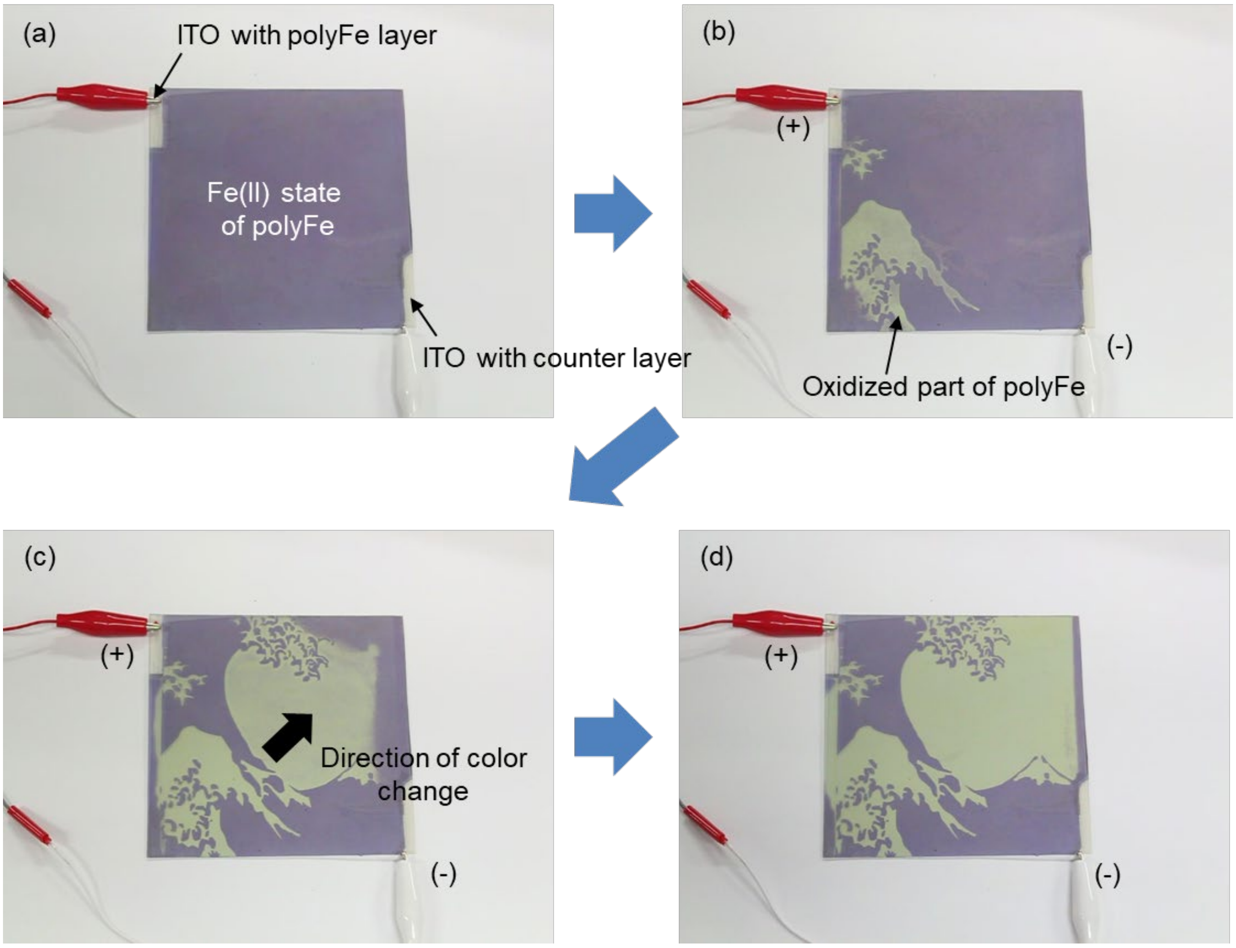

Fig. 7. (a) The flexible ECD with polyFe before applying a voltage. Images of the device at (b) 7 sec, (c) 30 sec, and (d) 90 sec when 1.5 V was applied.

Fe(II) complex moieties in polyFe. When the Fe(II) is oxidized to Fe(III) electrochemically, the MLCT absorption disappears and the color is changed to colorless.

When applying 1.5 V in the device by connecting the electrode coated with polyFe to the positive electrode side, interestingly, the color change from purple to colorless (pale green) occurred only on the left side image in the device during the first seven seconds (Fig. 7b). Then, the color change expanded from the center toward the right side, but the speed of the color change became slow. Eventually, it took 90 sec to display the whole image after applying the voltage.

The EC behavior provided the following findings in the display system of polyFe using the mechanically etched ITO film (Fig. 8).

(i) Unlike the previously reported two display systems (Figs. 5a and 5b), the color change in the EC layer first occurs only on the near side where the battery is connected, when a narrow path of ITO is formed by the mechanical etching.

(ii) The color changes at the far side to the battery from the narrow ITO path become slow. The narrow path is considered to have high resistance. Therefore, the voltage applied between the etched electrode and the counter electrode will decrease at the far side from the narrow path. The decrease of the applied voltage between the electrode causes the slow color changes.

(iii) The color of the polyFe layer on the area of ITO surrounded with the etched line perfectly does not show the EC changes, because the electron transfer on the ITO layer is cut off by the etching.

4. Conclusion

A designed, flexible electrochromic (EC) display device with polyFe was successfully fabricated using a mechanically etched ITO film. The mechanical etching of an ITO film was quickly performed with a cutting machine under ambient conditions. The fabricated device showed unique changes of the display upon applying a voltage of 1.5 V between the two ITO electrode. This display system using the etching technique is widely available in the EC displays with the other MSPs, which show various colors or multi-color EC changes.

Acknowledgement

This work was financially supported by JST CREST (grant No. JPMJCR1533).

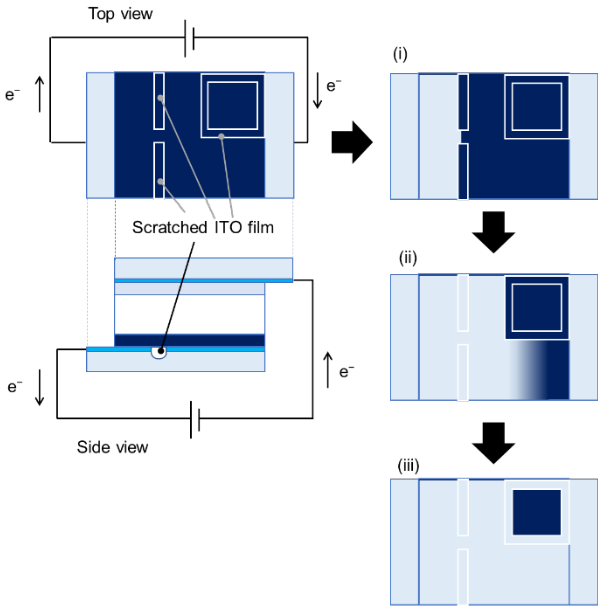

Fig. 8. Schematic images of the color changes in the ECD with polyFe using the mechanically etched ITO film. In case a narrow path of ITO and a closed area are included, the color changes occur by the order of (i) the initial change, (ii) the intermediate state, and (iii) the final state upon applying a voltage.

References

1. J. W. Xu, M. H. Chua, and K. W. Shah (eds), “Electrochromic Smart Materials”, Smart Materials Series, Royal Soc. Chem. (2019).
2. C. G. Granqvist, *Sol. Energy Mater. Sol. Cells*, **60** (2000) 201.
3. G. A. Niklasson and C. G. Granqvist, *J. Mater. Chem.*, **17** (2007) 127.
4. L. Groenendaal, F. Jonas, D. Freitag, H. Pielartzik, and J. R. Reynolds, *Adv. Mater.*, **12** (2000) 481.
5. N. Kobayashi, S. Miura, M. Nishimura, H. Urano, *Sol. Energy Mater. Sol. Cells*, **92** (2008) 136.
6. A. Tsuboi, K. Nakamura, and N. Kobayashi, *Adv. Mater.*, **25** (2013) 3197.
7. K. Takada, R. Sakamoto, S.-T. Yi, S. Katagiri, T. Kambe, and H. Nishihara, *J. Am. Chem. Soc.*, 137 (2015) 4681.
8. P. Andersson, R. Forchheimer, P. Tehrani, and M. Berggren, *Adv. Funct. Mater.*, **17** (2007) 3074.
9. C. Yan, W. Kang, J. Wang, M. Cui, X. Wang, C. Y. Foo, K. J. Chee, and P. S. Lee, *ACS Nano*, **8** (2014) 316.
10. S. Lin, X. Bai, H. Wang, H. Wang, J. Song, K. Huang, C. Wang, N. Wang, B. Li, M. Lei, and H. Wu, *Adv. Mater.* **29** (2017) 1703238.

11. H.-J. Yen, C.-J. Chen, and G.-S. Liou, *Adv. Funct. Mater.* **23** (2013) 5307.
12. C. Wang, X. Jiang, P. Cui, M. Sheng, X. Gong, L. Zhang, and S. Fu, *ACS Appl. Mater. Interfaces*, **13** (2021) 12313.
13. R. Li, X. Ma, J. Li, J. Cao, H. Gao, T. Li, X. Zhang, L. Wang, Q. Zhang, G. Wang, C. Hou, Y. Li, T. Palacios, Y. Lin, H. Wang, and X. Ling, *Nature Commun.*, **12** (2021) 1587.
14. G. Balamurugan, G. K. Pande, J. H. Choi, J. S. Park, *Sol. Energy Mater. Sol. Cells*, **216** (2020) 110714.
15. M. Higuchi, “Metallo-Supramolecular Polymers”, NIMS Monographs, Springer, Springer Nature (2019).
16. M. Higuchi, *J. Mater. Chem. C*, **2** (2014) 9331.
17. M. Higuchi and D. G. Kurth, *Chem. Rec.*, **7** (2007) 203.
18. F. Han, M. Higuchi, and D. G. Kurth, *J. Am. Chem. Soc.*, **130** (2008) 2073.
19. M. Higuchi, Y. Akasaka, T. Ikeda, A. Hayashi, and D. G. Kurth, *J. Inorg. Organomet. Polym. Mater.*, **19** (2009) 74.
20. S. Mondal, T. Yoshida, U. Rana, M. K. Bera, and M Higuchi, *Sol. Energy Mater. Sol. Cells*, **200** (2019) 110000.

Journal of Photopolymer Science and Technology
Volume 34, Number 2 (2021) 181－186 ©2021SPST

Micropatterning Performance and Physical Characteristics of Water-soluble High Molecular Weight Polysaccharide Photoresist Materials

Toru Amano[1,2*], Makoto Kobayasi[2], Satoshi Takei[1]

[1]Department of Mechanical Systems Engineering, Toyama Prefectural University,
Imizu, Toyama 939-0398, Japan
[2]Gunei Chemical Industry, Takasaki, Gunma 370-0032, Japan
**t-amano@gunei-chemical.co.jp*

Pullulan, a base polymer, is a water-soluble high-molecular-weight polysaccharide that easily forms films and is used for edible films and the like. We examined whether a photoresist material that makes the best use of its film-forming property and water solubility could be realized. The hydroxyl group of pullulan was modified with a photosensitive group to the extent that water solubility could be maintained, and a photosensitive material was created. This material is applied on a silicon wafer using spin coating, exposed with a mask contact exposure device, and then developed with water to evaluate sensitivity, etching resistance, and coating film strength. Microfabrication evaluation was performed. The result may be applicable as a water-soluble micropatterning material. Because this material does not use an organic solvent or a highly toxic strong alkaline developer, it is useful as a low environmental load-patterning material.

Keywords: Micro-patterning, Photoresist, Polysaccharide chain, Water-soluble material

1. Introduction

Photoresist materials are indispensable in semiconductor manufacturing, as electronic devices become more integrated, smaller more reliable, and faster in signal speed. Conventional photoresist materials used in semiconductor manufacturing are synthesized from fossil raw materials such as acrylic resin and phenolic resin, coated with an organic solvent, and developed with a strong alkaline developer or organic solvent. The many resins, solvents, and alkaline developers currently create significant waste, which is a problem.

In recent years, much attention has been paid to water-soluble photoresist materials that can be applied and developed with water. The main materials are water-soluble resin and water, and these are low environmental load-patterning materials that do not use an organic solvent or a highly toxic strong alkaline developer.

Although polyvinyl alcohol, polyacrylamide, and the like are often studied as water-soluble resins, they cannot be said to have a small environmental load because they are produced from fossil raw materials. [1-8]

Saccharides have been proposed as a water-soluble resist material with low environmental load, but it cannot be said that the low environmental load is sufficient because the coating is performed using an organic solvent. [9]

In addition, a plant-derived and water-soluble sugar (dextrin) photoresist material that can be coated and developed with water has been studied, but the coating strength is low due to the low molecular weight. As a result, the film strength after UV curing is low. [10]

Therefore, a photosensitive material using a high molecular weight polysaccharide (pullulan) with film-forming properties as the base polymer leads to a new micro-patterning material with improved coating strength compared with conventional water-soluble nanopatterning material.

In this paper, to confirm effectiveness of the water-soluble micropatterning material, the hydroxyl group of pullulan is modified with a photosensitive group to the extent that water solubility can be maintained, and exposure sensitivity and etching are

Received March 4, 2021
Accepted May 6, 2021

tested. We report that resistance, coating strength, and patterning properties.

2. Experimental

2.1. Materials

The high molecular weight polysaccharide used in this study was made from pullulan manufactured by HAYASHIBARA Co., Ltd.

For comparison, dextrin manufactured by San-ei Sucrochemical (NSD500) and NSD500 with the low molecular weight fraction removed (NSD500Hi, hereinafter) were used. To remove the low molecular weight fraction, dextrin was dissolved in water, and then methanol and ethanol were added to precipitate only the polymer portion in dextrin. The low molecular weight fraction removed can be arbitrarily controlled by the mixing ratio of water and solvent. The more water is, the higher the amount of low molecular weight fraction removed.

The results of gel permeation chromatography (HLC-8320GPC: Tosho) measurements to confirm the molecular weight distribution of each raw material are shown in Fig. 1 and Table 1.

The number average molecular weight (*M*n) of pullulan used as a raw material was 73292, and the weight average molecular weight (*M*w) was 161980. For NSD500, *M*n was 2454 and *M*w was 11383, and for NSD500Hi, *M*n was 7164 and *M*w was 32637.

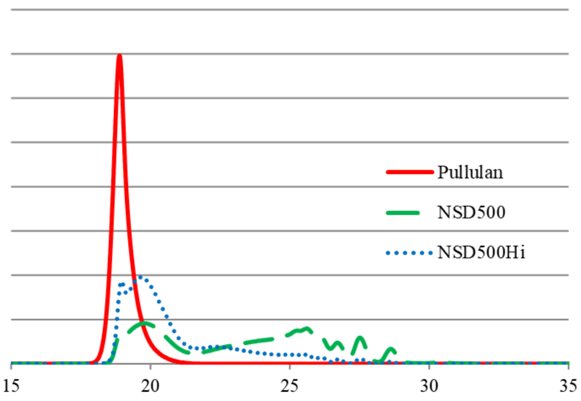

Fig. 1. Molecular weight distributions of base polymer.

Table.1. GPC measurement results of base polymer.

	*M*n	*M*w
Pullulan	73292	161980
NSD500	2454	11383
NSD500Hi	7164	32637

2.2. Synthesis of photosensitive polymer

The base polymers (Pullulan, NSD500, NSD500Hi) are dissolved in *N*-methylpyrrolidone, and acrylic acid is used to denature photosensitive groups by 30% with respect to all hydroxyl groups while maintaining the system temperature at 15°C or lower. Chloride was weighed and dropped over 2 h.

The solutions were then aged for 2 h at 15°C or below and neutralized with triethylamine. Next, *N*-methylpyrrolidone and a neutralizing salt were purified and removed, and the inside of the system was replaced with water to obtain a polysaccharide-based photosensitive material.

The modification to the photosensitive group was confirmed by ^{13}C-NMR and FT-IR. As an example, the synthesized structure of pullulan is shown in Fig. 2.

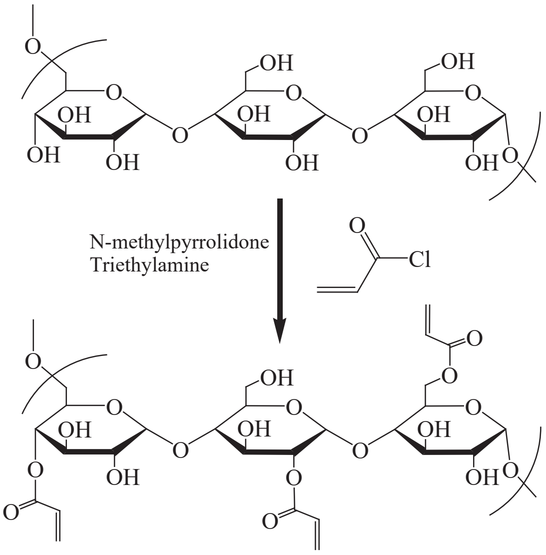

Fig. 2. Modification of pullulan hydroxyl groups to photosensitive groups.

Hereafter, the acrylic acid-denatured polysaccharide chains are referred to as Pullulan-A, NSD500-A, and NSD500Hi-A.

2.3. Measurement of exposure sensitivity

Omnirad 2959 (manufactured by IGM Resins B.V.) was used as the photosensitizer, and 1, 2, or 3 wt% was added to each aqueous solution of the acrylic acid-modified base polymer.

The obtained aqueous solutions were applied to a silicon wafer, spin-coated at 3000 rpm for 30 s using a spin coater (MS-B100: MIKASA) and baked at 80° C for 60 s to volatilize and remove water. Next, exposure is performed using a mask contact exposure device (LTCET-500: Lithotec Japan) and a sensitivity confirmation mask (Taiyo-ink Corporation: 5-inch Multi-Transmission Mask), the film thickness is measured, and then the film is

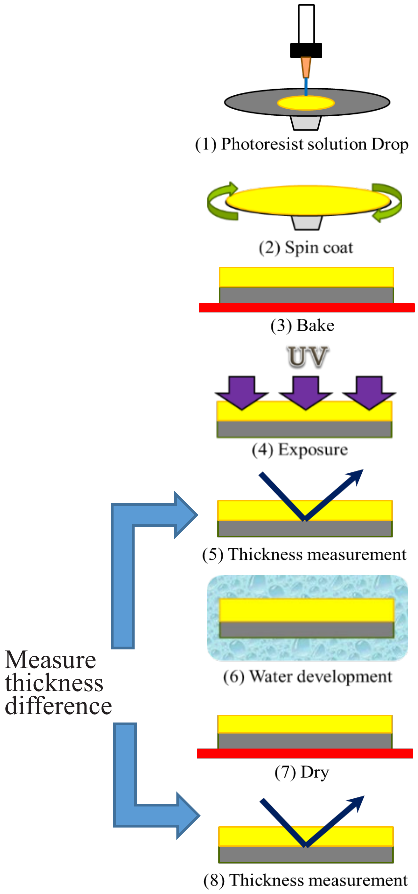

Fig. 3. Sensitivity measurement process for water-soluble micropatterning materials.

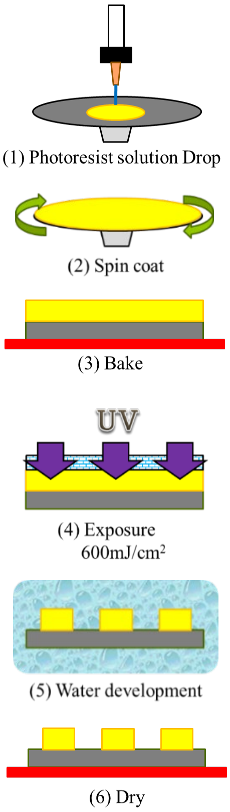

Fig 4. Microfabrication process of water-soluble patterning material.

developed to determine the residual film ratio. This process is diagrammed in Fig. 3. Using the above mask, it is possible to easily create a sensitivity curve.

2.4. Measurement of etching resistance

FA-1-TK manufactured by Samco Corporation was used to measure the etching resistance. For the measurement samples, 3 wt% of photosensitizer was added to each polymer. Pullulan-A was exposed to 100 mJ/cm^2, NSD500-A and NSD500Hi-A were exposed to 600 mJ/cm^2, and Cresol Novolac was used as a reference. CF_4 and O_2 were used as the etching gases.

2.5. Measurement of coating film strength

The measuring device used for coated film strength was a Dynamic Ultra Micro Hardness Tester: DUH-211S manufactured by Shimadzu Corporation.

2.6. Confirm of microfabrication

The evaluation method is as shown in Fig 4. A mask close contact exposure device (LTCET-500: Lithotec Japan) and a mask for microfabrication confirmation (TOPPAN PRINTING CO., LTD: TOPPAN-TEST-CHART-NO1-PN) were used to carry out the evaluations.

3. Research and Discussion

3.1 Exposure sensitivity evaluation

The exposure sensitivity of the water-soluble micropatterning material using high-molecular-weight polysaccharides was confirmed.

Pullulan-A was exposed at 150 mJ/cm^2, and NSD500Hi-A and NSD500-A were exposed at 1200 mJ/cm^2.

The sensitivity data indicate that to obtain a residual film ratio of 80 % or more, NSD500-A requires the addition of 2 wt% or more of photosensitizer and exposure of 900 mJ/cm^2 or more as shown in Fig. 5, and NSD500Hi-A requires the addition of 2 wt% or more of the photosensitizer and exposure of 660 mJ/cm^2 or more as shown in Fig. 6.

Pullulan-A maintained a residual film ratio of 80 % or more, regardless of photosensitizer wt% or >75 mJ/cm^2 exposure, confirming that it is a highly sensitive material (Fig. 7).

As shown in Fig. 5-7, the difference in molecular weight of each base polymer as shown in Fig. 1 has a great influence on its sensitivity.

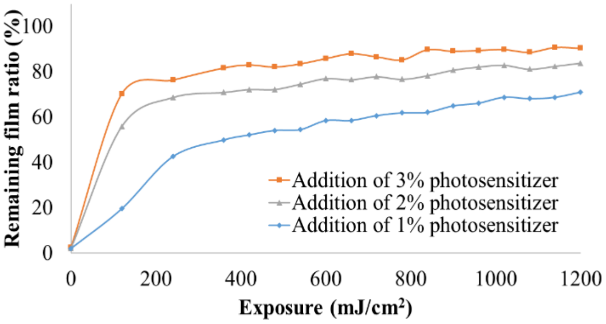

Fig. 5. NSD500-A sensitivity curve.

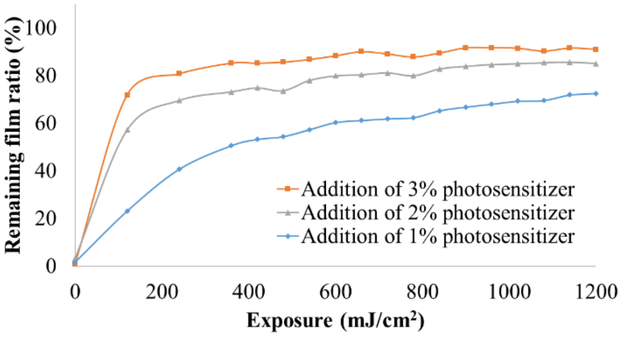

Fig. 6. NSD500Hi-A sensitivity curve.

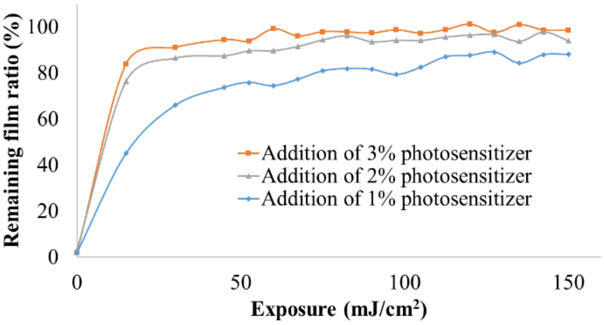

Fig .7. Pullulan-A sensitivity curve.

3.2. Etching resistance evaluation

Polysaccharides have low carbon density (according to the Ohnishi parameter) and relatively low etching resistance. It was measured whether the etching resistance was affected by the bonding mode and the molecular weight of the base polymer.

Etching resistance was low for all polysaccharides, and the reference, Cresol Novolac, gave the best results (Fig. 8 and 9).

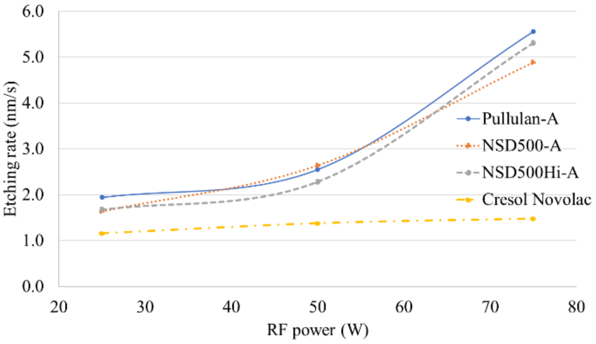

Fig. 8. Etching resistance evaluation result for CF_4.

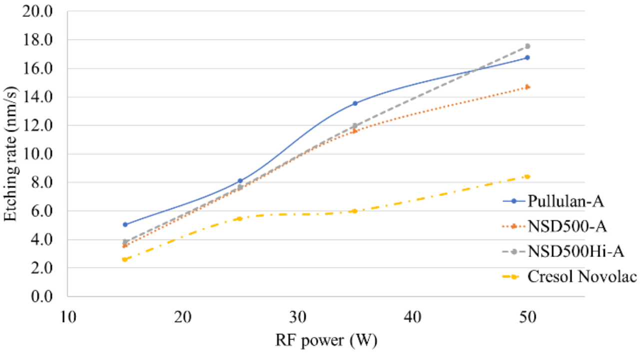

Fig. 9. Etching resistance evaluation result for O_2.

Table 2. Ohnishi parameter calculation results.

	Pullulan-A	NSD500-A	NSD500Hi-A	Cresol Novolac
Structural formula	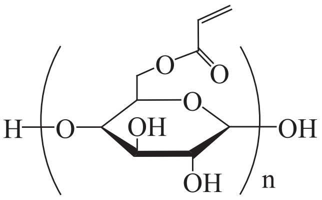			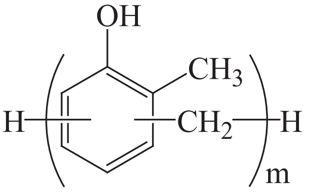
Ntotal	$C_9H_{14}O_7 = 30$			$C_8H_{10}O_1 = 19$
Ncarbon	9			8
Noxygen	7			1
Ohnishi parameter	15.0			2.7

This result is consistent with commonly known Ohnishi parameter results.

The Ohnishi parameter is a formula that uses the difference in etching rate between carbon and oxygen and is expressed by the following formula:

$$\text{Ohnishi parameter} = \frac{\text{Ntotal}}{\text{Ncarbon} - \text{Noxygen}}$$

where Ntotal is the total number of atoms in the molecule, Ncarbon is the number of carbon atoms in the molecule, and Noxygen is the number of oxygen atoms in the molecule.

For example, for benzene C_6H_6, Ntotal is 12, Ncarbon is 6, Noxygen is 0, and the Ohnishi parameter is 2.0. For phenol $C_6H_6O_1$, Ntotal is 13, Ncarbon is 6, and Noxygen is 1; thus, the Ohnishi parameter is 2.6. To increase the etching resistance, it is necessary to increase the carbon ratio and decrease the value of the Ohnishi parameter.

Table 2 lists calculations of the Ohnishi parameter for Pullulan-A, NSD500-A, NSD500Hi-A, and Cresol Novolac.

The Ohnishi parameter value for polysaccharides is large, whereas Cresol Novolac has a small value, which correlates with the results in Figs. 7 and 8.

3.3. Coating film strength evaluation

Pullulan exhibits coating strength that is not found in conventional water-soluble micropatterning polysaccharides because of its film-forming ability. Film strength measurements were also performed.

For the measurement samples, 3 wt% of photosensitizer was added to each polymer. Pullulan-A was exposed to 100 mJ/cm^2, and NSD500-A and NSD500Hi-A were exposed to 600 mJ/cm^2.

NSD500-A was determined to be soft, and Pullulan-A was hard based on the maximum displacement (hmax), indentation hardness, and indentation elastic modulus (Fig. 10).

This phenomenon correlates to exposure sensitivity and the residual film ratio. A material with good sensitivity and high residual film ratio is three-dimensionally crosslinked and has many polymerized portions.

Crosslinking and polymerization have a great influence on hardness (Table 3).

From the load and displacement curves shown in Fig. 10 and the values listed in Table 3, it was confirmed that there are no significant differences in hardness or elastic modulus between Pullulan-A and NSD500Hi-A.

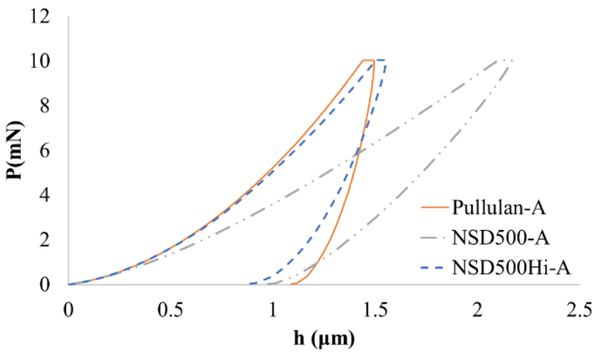

Fig. 10. Displacement measurement result for load by nano indenter.

Table 3. Hardness and elastic modulus measurements by nano indenter.

	Fmax (mN)	Hmax (µm)	Hit^a (MPa)	Eit^b (MPa)
Pullulan-A	10.03	1.493	170.5	7.054E + 03
NSD500-A	10.04	2.166	132.9	1.245E + 03
NSD500Hi-A	10.04	1.553	188.2	3.679E + 03

a) Hit is indentation hardness. b) Eit is indentation modulus.

Pullulan is an effective film former before UV curing, but after curing, it is not much different fromNSD500Hi-A, and pullulan's film-forming properties are lost due to three-dimensional crosslinking. It is suggested that UV curing adversely affects the film-forming ability.

3.4. Microfabrication evaluation

Microfabrication evaluation of the high molecular weight polysaccharide was carried out.

For the evaluation samples, 3 wt% of photosensitizer was added to each polymer. Pullulan-A was exposed to 100 mJ/cm^2, and NSD500-A and NSD500Hi-A were exposed to 600 mJ/cm^2.

NSD500-A and NSD500Hi-A showed good microfabrication results, and Pullulan-A had a lot of undissolved residue between the patterns.

NSD500-A is only slightly affected by UV reflection and diffraction during exposure because the base polymer is small molecular weight and the exposure sensitivity is low. Therefore, the uncured portion is easily dissolved in the developing solution (water), and relatively clean and fine patterning is possible. (Fig. 11).

NSD500Hi-A has the low molecular weight fraction removed, but its molecular weight is still relatively small, and its exposure sensitivity is not so high. Therefore, relatively clean and fine patterning was also possible (Fig. 12).

Pullulan-A has a molecular weight 10 times or more than that of NSD500-A and an exposure sensitivity of 10 times or more.

Therefore, if there is even a small amount of UV reflection or diffraction between patterns that are not exposed to UV, the crosslinking reaction proceeds, and the polymer becomes insoluble in the developing solution (water), making microfabrication difficult. (Fig. 13).

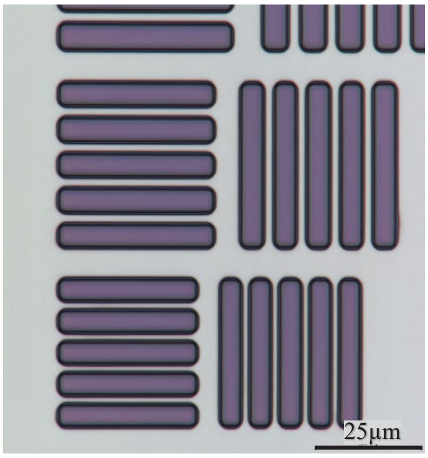

Fig. 11. NSD500-A micropatterning results.

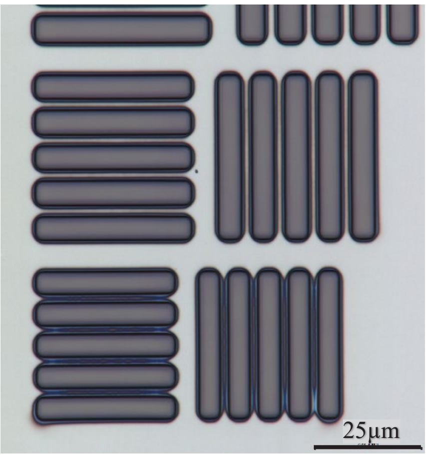

Fig. 12. NSD500Hi-A micro patterning results.

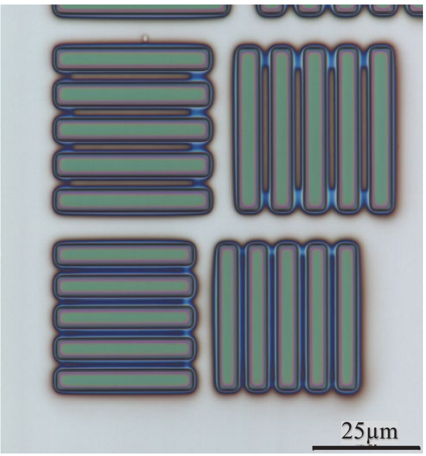

Fig. 13. Pullulan-A micropatterning results.

4. Conclusion

The effectiveness of water-soluble micropatterning materials using high molecular weight polysaccharides was investigated. By converting the hydroxyl groups of the high molecular weight polysaccharide into photosensitive groups to the extent that water solubility can be maintained, a water-soluble micropatterning material was created. The obtained water-soluble micropatterning material had better film-forming properties before UV curing and higher sensitivity than those using dextrins. However, effectiveness of the coating films after UV curing could not be confirmed because it was not much different from that of dextrins. Exposure sensitivity was too high, and even a small amount of UV reflection or diffraction caused the undissolved residue between the patterns, making fine patterning difficult.

It will be necessary to optimize this material by adjusting the amount and concentration of the photosensitizer added to use it as a water-soluble micropatterning material.

References

1. H. Morishita, M. Ito, N. Hayashi, and S. Nonogaki, *J. Photopolym. Sci. Technol.*, **7** (1994) 59.
2. Q. Lin, T. Steinhausler, L. Simpson, M. Wilder, D. R. Medeiros, and C. G. Willson, *Chem. Mater.*, **9** (1997) 1725.
3. J. M. Havard, M. Yoshida, D. Pasini, N. Vladimirov, J. M. J. Frechet, D.R. Medeiros, K. Patterson, S. Yamada, C. G. Willson, J. D. Byers, *J. Polym. Sci.*: *Part A: Polymer Chemistry*, **37** (1999) 1225.
4. J. M. Havard, S.-Y. Shim, and J. M. J. Frechet, *Chem. Mater.*, **11** (1999) 719.
5. K. Kojima, M. Ito, H. Morishita, and N. Hayashi, *Chem. Mater.*, **10** (1998) 3429.
6. J. Swei and J. B. Talbot, *J. Appl. Polym. Sci.*, **102** (2006) 1637.
7. S.-Y. Shim and J.-M. Kim, *Bull. Korean Chem. Soc.*, **22** (2001) 1120.
8. K. H. Chae, G. J. Sun, J. K. Kang, and T. H. Kim, *J. Appl. Polym. Sci.*, **86** (2002) 1172.
9. Y. Y. Liao and J.-H. Liu, *J. Appl. Polym. Sci.*, **109** (2008) 3849.
10. T. Amano, D. Hirata, Y. Hasegawa, and S. Takei, *J. Photopolym. Sci. Technol.*, **33** (2020) 445.

Journal of Photopolymer Science and Technology
Volume 34, Number 2 (2021) 187−193 ©2021SPST

Effect of Sugar Chain Binding Mode on Water-soluble Micropatterning Performance and Physical Characteristics

Toru Amano[1,2*], Makoto Kobayasi[2], and Satoshi Takei[1]

[1]*Department of Mechanical Systems Engineering, Toyama Prefectural University,*
Imizu, Toyama 939-0398, Japan
[2]*Gunei Chemical Industry, Takasaki, Gunma 370-0032, Japan*
**t-amano@gunei-chemical.co.jp*

Dextrins commonly known as sugar chains include 1,4- and 1,6-bonded dextrins, which are obtained by enzymatically decomposing starch, and is indigestible dextrin, which is obtained by decomposing starch by an enzymatic reaction and forming 1,2- or 1,3-bonds by acid catalyst treatment. Herein we investigate the water-soluble micropatterning performance of these indigestible dextrins and the change in physical characteristics depending on the structure. The hydroxyl group of each dextrin was modified with a photosensitive group while maintaining water solubility, resulting in a water-soluble photosensitive material.

This material was applied onto a silicon wafer using spin coating, exposed with a mask contact exposure device, and then developed with water to evaluate the sensitivity, etching resistance, and coating film strength. The microfabrication evaluation indicated that the performance was sensitive to the binding mode, and it was found that the indigestible dextrin is functional as a water-soluble micropatterning material. Given that this material does not require an organic solvent or a highly toxic strong alkaline developer, it is effective as a low environmental load patterning material.

Keywords: Micropatterning, Photoresist, Sugar chain, Water-soluble material

1. Introduction

Photoresist materials are indispensable in the manufacturing of semiconductor devices and are being miniaturized as electronic devices become more integrated, smaller, more reliable, and faster in signal speed.

In the evolution of electronic devices, a problem has arisen that many resins, solvents, and alkaline developers used in semiconductor manufacturing are treated as waste and disposed of in large quantities.

Conventional photoresist materials are synthesized from fossil raw materials (e.g., acrylic resin and phenol resin), coated with an organic solvent, and developed with a strong alkaline developer or organic solvent. Therefore, it is difficult to reduce the waste that is generated by this process.

In recent years, much attention has been focused on producing water-soluble photoresist materials that can be applied and developed using water.

The primary materials are water-soluble resin, which is a low environmental load patterning material that does not require an organic solvent or a highly toxic strong alkaline developer.

Polyvinyl alcohol, polyacrylamide, and related compounds have been widely studied as water-soluble resins, but since they are produced from fossil raw materials, the environmental load is still significant. [1-8]

A material containing saccharides has been proposed as an alternative water-soluble resist material, but the total environmental load of the process is still substantial because the coating is performed using an organic solvent. [9]

In addition, water-soluble photoresist materials that can be coated and developed with water and are composed of plant-derived and water-soluble sugars (dextrin) have shown promise, but only 1,4- and 1,6-bonds have been studied. An evaluation of only the main general dextrin system was performed, and

---

Received March 4, 2021
Accepted May 6, 2021

the effect of the binding mode is still unknown. [10]

Therefore, we report that the synthesis of water-soluble micropatterning materials using indigestible dextrin formed by 1,2- and 1,3-bonds, along with their exposure sensitivity, etching resistance, coating film strength, and patterning characteristics.

2. Experimental

2.1. Materials

The indigestible dextrins used in this study were made from Roquette (product name: NUTRIOSE) and Matsutani Chemical Industry Co., Ltd. (product name: Fiber Sol 2).

For comparison, dextrin manufactured by Sanei Saccharification Co., Ltd. (product name: NSD500), and NSD500 with the lower molecular weight fractions removed (hereinafter referred to as NSD500Hi) were used.

Gel permeation chromatography (HLC-8320GPC: Tosho) measurements were used to confirm the molecular weight distribution of each raw material and are shown in Fig. 1 and Table 1.

The number average molecular weight (*Mn*) of the NUTRIOSE raw material was 3297 and the weight average molecular weight (*Mw*) was 4567, while Fiber Sol 2 had a *Mn* of 2783 and a *Mw* of 4180. In comparison, NSD500 had a *Mn* of 2454 and a *Mw* of 11383, while NSD500Hi had a *Mn* of 7164 and a *Mw* of 32637.

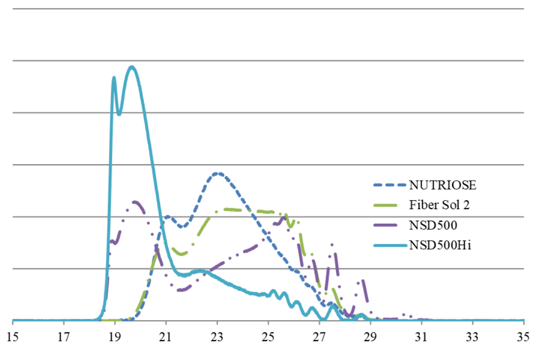

Fig.1. Comparison of molecular weight distribution of base polymer.

Table. 1. GPC measurements results of the base polymers.

	Mn	*Mw*
NUTRIOSE	3297	4567
Fiber Sol 2	2783	4180
NSD500	2454	11383
NSD500Hi	7164	32637

2.2. Analysis of dextrin binding mode

Indigestible dextrin is a dextrin that contains 1,2- or 1,3-bonds in its structure, as described in the previous section.

The 1,2- and 1,3-bond ratios were analyzed by ^{13}C NMR spectroscopy (ECZ500R manufactured by JEOL RESONANCE), and the three-dimensional structure was analyzed by Chem3D (ChemOffice 2016 manufactured by PerkinElmer).

2.3. Synthesis of photosensitive polymer

The base polymers (NUTRIOSE, Fiber Sol 2, NSD500, and NSD500Hi) were separately dissolved in *N*-methylpyrrolidone so that the photosensitive groups (acrylic acid) were 30% denatured with respect to all hydroxyl groups. The system temperature was maintained at 15°C or lower.

Acrylic acid chloride was then added dropwise over a period of two hours.

The solution was then aged for two hours at 15°C or below followed by neutralization with triethylamine. Next, *N*-methylpyrrolidone and a neutralizing salt were removed and purified, and the remaining material was dissolved in water to obtain a photosensitive material formed from saccharides, as shown in Fig. 2.

The modification to the photosensitive group was confirmed by ^{13}C NMR and Fourier-transform infrared (FTIR) spectroscopies. As an example, the reaction path of NSD500 is shown in Fig. 2.

Hereafter, the acrylic acid-denatured sugar chains are referred to as NUTRIOSE-A, Fiber Sol 2-A, NSD500-A, and NSD500Hi-A.

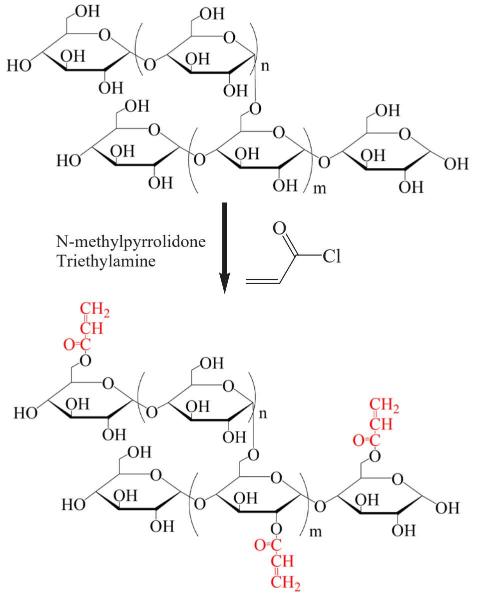

Fig. 2. Modification of hydroxyl groups to photosensitive groups.

2.4. Measurement of exposure sensitivity

The exposure sensitivity of each dextrin with the added photosensitive groups was evaluated.

Omnirad 2959 (manufactured by IGM Resins B.V.) was used as the photosensitizer, and 1 wt%, 2 wt%, or 3 wt% of the photosensitizer was added to aqueous solutions of the acrylic acid-modified base polymers.

The obtained aqueous solutions were applied onto a silicon wafer by spin coating (MS-B100: MIKASA) at 3000 rpm for 30 seconds followed by calcination at 80°C for 60 seconds to volatilize and remove any residual water.

Next, exposure was performed using a mask close contact exposure device (LTCET-500: Lithotec Japan) and a sensitivity confirmation mask (Taiyo-Ink Co.: 5-inch multi-transmission mask), the film thickness was measured, and then the film was developed to determine the residual film ratio, as shown in Fig. 3. By using the above mask, it is possible to easily create a sensitivity curve. NUTRIOSE-A and Fiber Sol 2-A were exposed at 600 mJ/cm^2, and NSD500Hi-A and NSD500-A were exposed at 1200 mJ/cm^2.

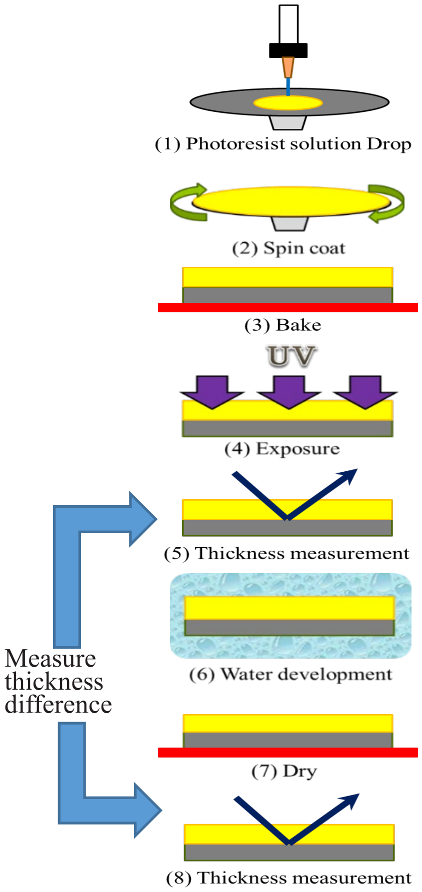

Fig. 3. Sensitivity measurement process for water-soluble micropatterning materials.

2.5. Measurement of coating film strength

To determine the effect that the 1,2- and 1,3-bonds of the indigestible dextrin have on the strength of the coating film, the strength was measured by a nanoindenter. The device used was a dynamic ultra micro hardness tester: DUH-211S, manufactured by Shimadzu Corporation.

For the measurements, 3 wt% of a photosensitizer was added to each dextrin, and NUTRIOSE-A and Fiber Sol 2-A were exposed to 300 mJ/cm^2, and NSD500-A and NSD500Hi-A were exposed to 600 mJ/cm^2.

2.6. Confirm of microfabrication

Finally, the effect of the 1,2- and 1,3-bonds of the indigestible dextrin on the microfabrication was investigated.

The measurements were conducted with 3 wt% of a photosensitizer added to each dextrin, followed by exposure to 300 mJ/cm^2 for NUTRIOSE-A, Fiber Sol 2-A, and LitesseHF-A, and 600 mJ/cm^2 for NSD500-A and NSD500Hi-A.

The evaluation method is shown in Fig. 4, where a mask close contact exposure device (LTCET-500: Lithotec Japan) and a mask for microfabrication confirmation (Toppan Printing Co., Ltd: TOPPAN-TEST-CHART-NO1-PN) were used.

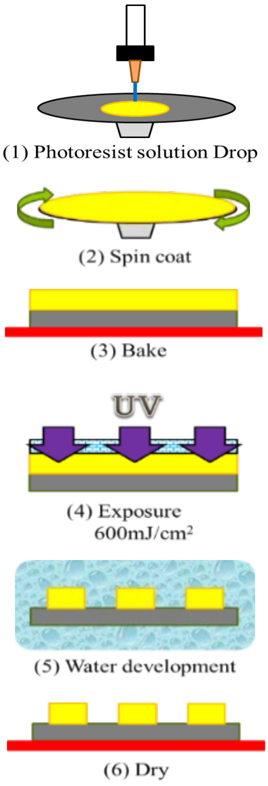

Fig.4. Microfabrication process of water-soluble patterning material.

3. Research and discussion

3.1. Characterization of the indigestible dextrin

The ^{13}C NMR spectra are shown in Fig. 5 and Table 2.

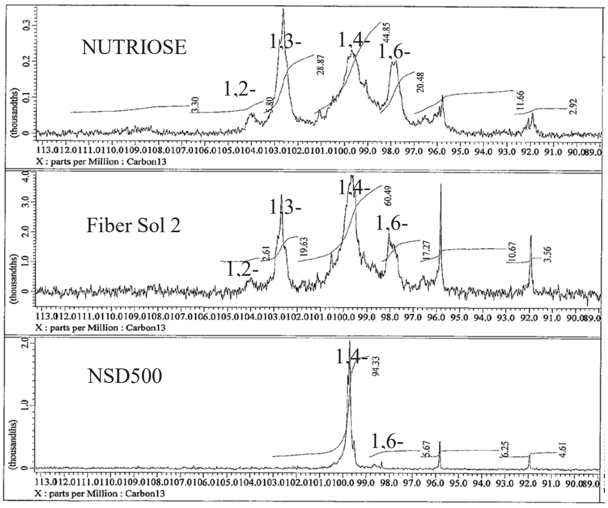

Fig.5. ^{13}C-NMR measurement results of various dextrins.

Table .2. Results of Measurements of relative binding modes of for various dextrins by determined by ^{13}C-NMR spectroscopy.

	1,2-	1,3-	1,4-	1,6-
NUTRIOSE	5.8%	28.9%	44.9%	20.5%
Fiber Sol 2	2.9%	19.2%	60.2%	17.7%
NSD500	—	—	94.3%	5.7%

It was confirmed that indigestible dextrins with 1,2- and 1,3-bonds were not present in generic dextrin. It is speculated that the cause of the high 1,2- and 1,3-bonding ratio in NUTRIOSE is a longer acid catalyst treatment time compared to that of Fiber Sol 2, and the resulting polymer is polymerized. From these results, it was clear that indigestible dextrins contain many branched structures.

The results of the 3D structural analysis by Chem3D are shown in Fig. 6. It can be observed that the molecules are entangled in the case of 1,3-bonds, but there is little entanglement in the other bond types.

From the ^{13}C NMR spectra and Chem3D, it was found that indigestible dextrins are sugar chains containing many branched structures with some degree of entanglement within the molecules.

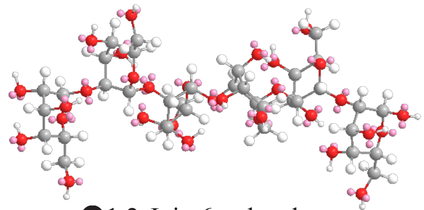

●1,2-Join 6molecules.

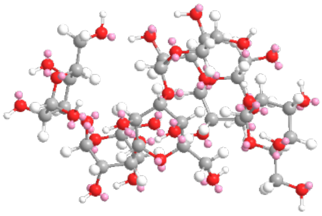

●1,3-Join 6molecules.

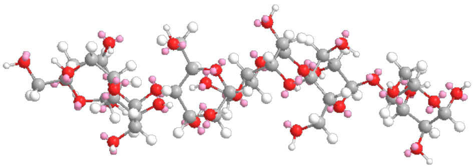

●1,4-Join 6molecules.

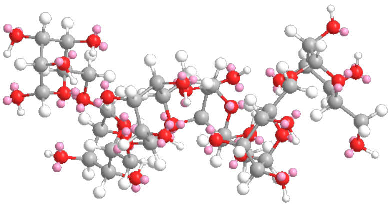

●1,6-Join 6molecules.

Fig. 6. Three-dimensional structure of the binding mode of sugar chains.

3.2. Exposure sensitivity evaluation

The results indicate that to obtain a residual film ratio of 80% or more, NSD500-A and NSD500Hi-A must have a photosensitizer concentration of 2 wt% or more and an exposure of at least 900 mJ/cm^2 (Fig. 9 and Fig. 10). NUTRIOSE-A and Fiber Sol 2-A were found to achieve a residual film ratio of 80% or more (Fig. 7 and Fig. 8) at a photosensitizer concentration of 2% or more and an exposure of 300 mJ/cm^2.

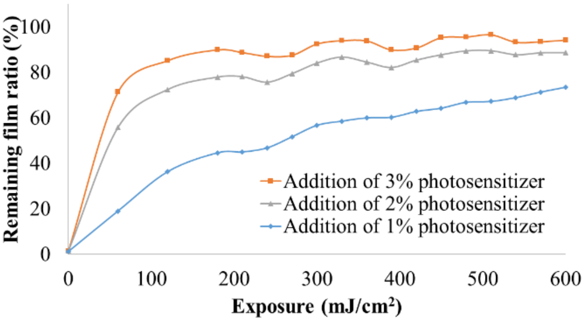

Fig. 7. NUTRIOSE-A sensitivity curve.

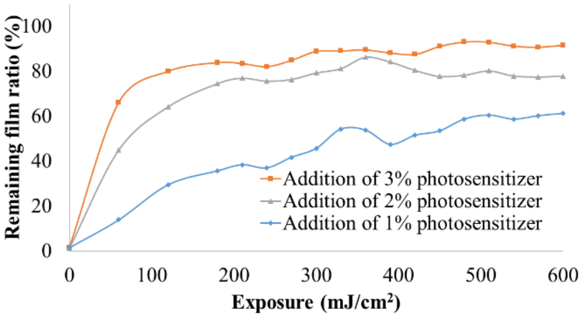

Fig. 8. Fiber Sol 2 -A sensitivity curve.

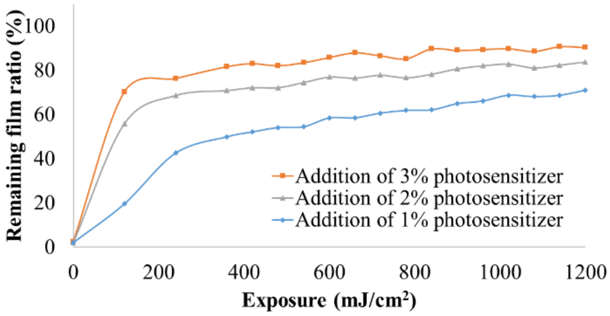

Fig. 9. NSD500-A sensitivity curve.

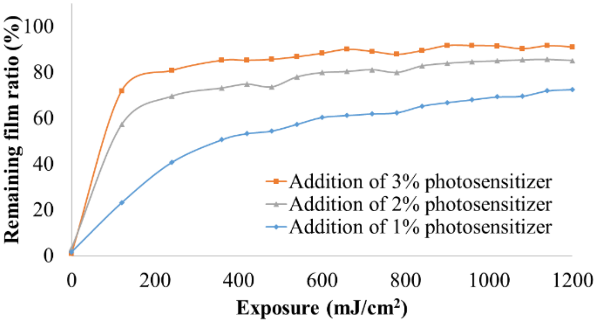

Fig.10. NSD500Hi-A sensitivity curve.

Typically, the higher the molecular weight, the higher the sensitivity, but NUTRIOSE-A and Fiber Sol 2-A were found to have higher sensitivities than NSD500Hi-A, even though they have much lower molecular weights.

The cause of this discrepancy is likely from the difference in the binding modes.

Indigestible dextrins with 1,2- and 1,3-bonds are sugar chains with many branched structures and many entangled molecules, and with the addition of a hardening reaction, the molecules become more entangled and insolubilized, leading to an increase in the sensitivity.

3.3. Coating film strength evaluation

The hardness measurements indicated that NSD500-A was soft in terms of the maximum displacement (h_{max}), indentation hardness (H_{it}), and indentation elastic modulus (E_{it}), and no significant difference was found between the other three dextrins (Table 3 and Fig. 11). indentation elastic modulus (E_{it}), and no significant difference was found between the other three dextrins (Fig. 11 and Table 3).

This phenomenon is explained by the relationship between the exposure sensitivity and the residual film ratio, where a material with a good sensitivity and a high residual film ratio is three-dimensionally crosslinked and contains many polymerized sections.

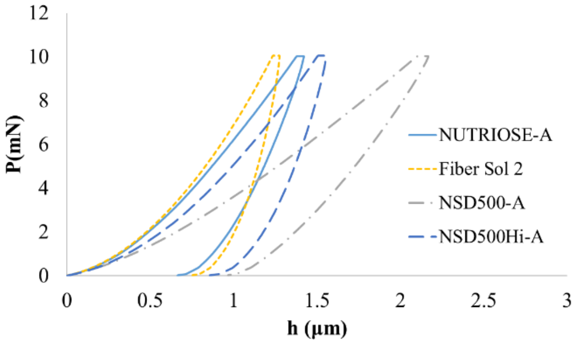

Fig.11. Displacement measurement result for load by nano indenter.

Given that NSD500Hi-A is originally a polymer, a high elastic modulus can be obtained. In addition, NUTRIOSE-A and Fiber Sol 2-A have 1,2- and 1,3-bonds, which results in a multitude of molecular entanglements and therefore an increase in the hardness.

Table.3. Measurement results of hardness and elastic modulus by nano indenter.

	F_{max} (mN)	H_{max} (µm)	H_{it} (MPa)	E_{it} (MPa)
NUTRIOSE-A	10.04	1.421	267.9	3.325E+03
Fiber Sol 2-A	10.04	1.273	261.9	6.502E+03
NSD500-A	10.04	2.166	132.9	1.245E+03
NSD500Hi-A	10.04	1.553	188.2	3.679E+03

3.4. Microfabrication evaluation

Figure 12-15 shows the microfabricated shapes of NSD500-A, NSD500Hi-A, and Fiber Sol 2-A.

During the development as shown in Fig. 4, NUTRIOSE-A peeled off from the silicon wafer, and microfabrication could not be confirmed. In addition, it was observed that while NSD500-A and NSD500Hi-A gave a microfabrication thickness of about 6 μm, Fiber Sol 2-A gave a microfabrication thickness of about 3 μm.

Fiber Sol 2-A has high solubility in water due to its low molecular weight and is highly sensitive given the 1,2- and 1,3-bonds in its structure. These factors provide a good balance between solubility and sensitivity for use in microfabrication.

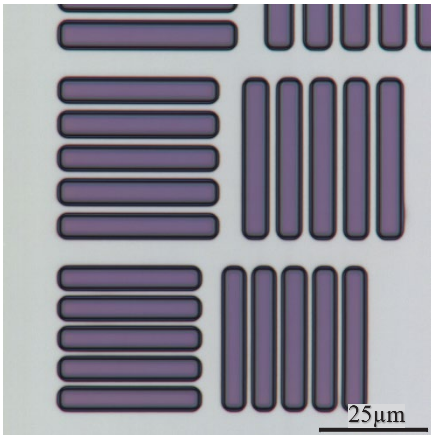

Fig.12. NSD500-A micro patterning results.

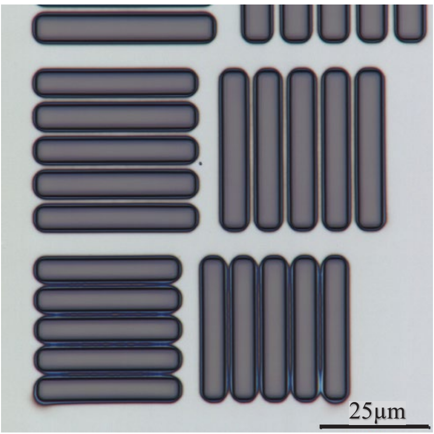

Fig.13. NSD500Hi-A micro patterning results.

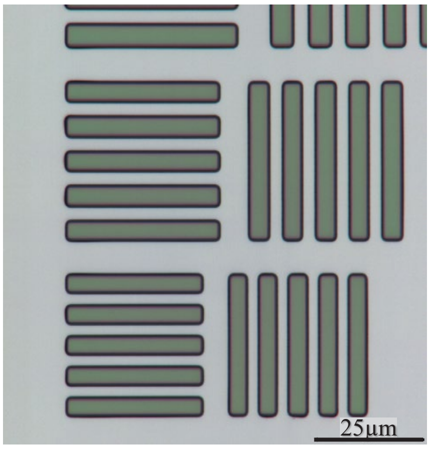

Fig.14. Fiber Sol 2-A micro patterning results-1.

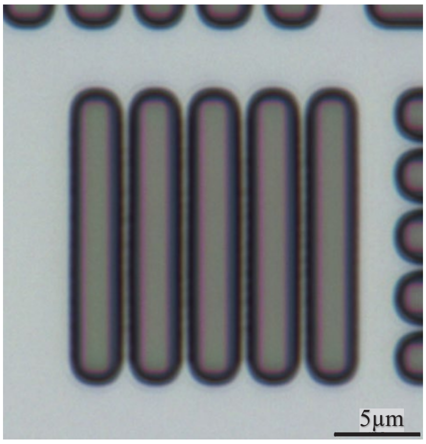

Fig.15. Fiber Sol 2 micro patterning results-2.

4. Conclusion

The effectiveness of water-soluble micropatterning materials composed of indigestible dextrins containing 1,2- and 1,3-bonds were investigated.

By converting the hydroxyl groups of the indigestible dextrins into a photosensitive group to the extent that water solubility could be maintained, a water-soluble micropatterning material composed of indigestible dextrin was created.

The resulting water-soluble micropatterning material has solubility in water and a high sensitivity suitable for microfabrication, in contrast 1,6-bonds.

However, peeling from the silicon wafer was observed in some samples, so improvements in the adhesiveness are necessary.

References

1. H. Morishita, M. Ito, N. Hayashi, and S. Nonogaki, *J. Photopolym. Sci. Technol.*, **7**

(1994) 59.

2. Q. Lin, T. Steinhausler, L. Simpson, M. Wilder, D. R. Medeiros, and C. G. Willson, C*hem. Mater.*, **9** (1997) 1725.
3. J. M. Havard, M. Yoshida, D. Pasini, N. Vladimirov, J. M. J. Frechet, D.R. Medeiros, K. Patterson, S. Yamada, C. G. Willson, and J. D. Byers, *J. Polym. Sci.: Part A: Polymer Chemistry*, **37** (1999) 1225.
4. J. M. Havard, S.-Y. Shim, and J. M. J. Frechet, *Chem. Mater.,* **11** (1999) 719.
5. K. Kojima, M. Ito, H. Morishita, and N. Hayashi, *Chem. Mater.,* **10** (1998) 3429.
6. J. Swei and J. B. Talbot, *J. Appl. Polym. Sci.*, **102** (2006) 1637.
7. S.-Y. Shim and J.-M. Kim, *Bull. Korean Chem. Soc.*, **22** (2001) 1120.
8. K. H. Chae, G. J. Sun, J. K. Kang, and T. H. Kim, *J. Appl. Polym. Sci.*, **86** (2002) 1172.
9. Y. Y. Liao and J.-H. Liu, *J. Appl. Polym. Sci*., 109 (2008) 3849.
10. T. Amano, D. Hirata, Y. Hasegawa, and S. Takei *J. Photopolym. Sci. Technol.*, **33** (2020) 445.

Journal of Photopolymer Science and Technology
Volume 34, Number 2 (2021) 195－199 ©2021SPST

Low Stress and Low Temperature Curable Photosensitive Polyimide

Yu Shoji[1]*, Keika Hashimoto[1], Yutaro Koyama[1], Yuki Masuda[1], Hitoshi Araki[1], and Masao Tomikawa[1]

[1] *Department of Electronic & Imaging Materials Res. Labs., Toray Industries Inc.,*
1-2, Sonoyama 3-Chome, Otsu, Shiga 520-0842, Japan
**yu.shoji.r7@mail.toray*

Low stress / low temperature curable photosensitive polyimide (PSPI) with excellent reliability during thermal cycle (TC) has been developed for a quite some time. The effect of residual stress concerning PSPI on copper-PSPI inter-connect structure was examined by Finite Element Method (FEM), and it became evident that the crack has tendency to appear at the top corner between copper and PSPI, where highest stress lay during the cooling process of TC test. Low stress PSPI is one of the candidates to reduce residual stress on copper-PSPI inter-connect structure, and indeed, no crack was found after FEM and TC test. Through a series of tests mentioned above, we came to realize that an introduction of soft segment into polyimide backbone of PSPI is the key factor to create a robust low stress PSPI. In addition of creating a robust low stress / low temperature curable PSPI, further research was conducted to improve the copper compatibility of PSPI through grasping the ways of controlling the oxidation of copper.

Keywords: Photosensitive polyimide, Low stress, Finite element method, Reliability

1. Introduction

Recently, higher density, narrower bump pitch and thinning of 3D Jisso are the trends in the advanced integrated packages. Moreover, in order to implement the trends of advanced integrated packages, an application processor (AP) controlling all functions of mobile devices is believed to be one of the key devices to do so. Thus far, most APs are integrated by Package on Package (PoP) technology, which includes considerable thick substrate for mounting devices [1]. In the recent package trend, Fan-Out Wafer Level Package (FO-WLP) technology became a remarkable package technology, which opened-up a technological window to manufacture extremely thin devices [2]. The FO packages are usually composed of semiconductor die placed in mold resin and re-distribution layer (RDL) fabricated on the top of semiconductor die, within mold resin. RDL patterns consist of conductive copper metal and non-conductive insulant materials such as photosensitive polyimide (PSPI) and polybenzoxazole (PSPBO) to insure package reliability. When selecting non-conductive low temperature curable materials, there are several critical requirements to prevent damages to the FO-WLP packages, and one of the requirements is the curing temperature. Selection can easily be fulfilled if robust conventional PSPI and PSPBO, which require high temperature treatment to complete the ring closure reaction; however, FO-WLP require low temperature cure. It is widely known that to complete low temperature ring closure reaction for PBO precursor, introduction of flexible structure in polymer chain worked successfully [3,4]. On the same note, report has indicated that PBO ring closure reaction was accelerated by adding sulfonic acid and photo base generator during low temperature imidization [5,6]. A phenomenon of applying additives to PSPI was also reported by Sasaki [6], which made the development of low temperature curable PSPI for RDL insulator of FO-WLP.

We have developed various type of PSPI materials for several electronic devices such as semiconductor and OLED. A PSPI composed of novel partially esterified poly (amic acid) and

---

Received March 20, 2021
Accepted April 13, 2021

diazonaphthoquinone compound was developed by utilizing photosensitive polymer technologies [7,8]. However, the problem with this polymer technology was that curing temperature over 300 °C necessitated the conversion of poly (amic acid) to polyimide by intermolecular cyclization. For FO-WLP applications, low temperature curable PSPIs were required due to low thermal stability of mold compound and memory device as mentioned before. In addition, copper compatibility and mechanical reliability of PSPI are also important because the FO-WLP technology requires to form copper RDL with PSPI as an insulator.

In this report, the development of low temperature curable PSPI by utilizing a pre-imidized polyimide with low temperature curable cross-linker will be introduced. We have investigated our own development through a series of demonstrative stress simulation of quasi FO-WLP package by changing physical parameters of PSPI by FEM as well as the effect of residual stress of PSPI when utilized for RDL insulators. Furthermore, we have also focused our study to implement copper compatibility to the reliability of PSPI.

2. Experimental

Materials. PI was synthesized by polycondensation of tetracarboxylic dianhydrides with diamines. The proper amount of diamines was placed in a 4-neck flask with a mechanical stirrer, thermometer, and nitrogen inlet. Then, *N*-methyl-2-pyrridone (NMP) was added to the flask. The flask was heated to 60 °C under nitrogen flow. After diamines have dissolved, the proper amount of tetracarboxylic dianhydrides was added into the diamine solution. The mixture was stirred for an hour at 60 °C, then heated to 180 °C. Polycondensation reaction was carried out at 180 °C for 4 hours. After cooling to room temperature, PI solution was poured into the water to precipitate. The obtained PI was collected by filtration, then dried at 50 °C for 72 hours in a convection oven.

PSPI varnish sample was prepared by following procedure. The dried PI (3.51g), diazonaphthoquinone compound (DNQ, 0.62g), and cross-linker (0.12g) were mixed into 5.75 g of γ-butyrolactone (GBL). The solution was filtered through a 0.2 μm pore poly (tetrafluoroethylene) filter to remove the particles. Chemical structures of DNQ and cross-linkers are shown in Fig. 1.

Pattern formation. The obtained varnish sample was coated on an 8-inch Si wafer by a spin-coater (ACT-8, Tokyo Electron), then soft-baked at 120 °C for 3 min on a hot plate equipped with ACT-8. The film was exposed by an i-line stepper (Nikon, NSR-2205i14) from 200 mJ cm^{-2} to 800 mJ cm^{-2}. After lithographic exposure, the exposed film was developed by 2.38% tetramethylammonium hydroxide aqueous solution (TMAHaq) at 23 °C. Finally, the 5–15 μm PSPI patterned wafer was obtained after cured in a clean oven (CLH-21CD (V)-S, KOYO THERMOSYSTEMS Co., Ltd) at a condition of 180–250 °C.

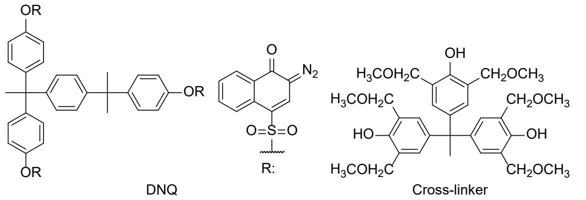

Fig. 1. Chemical structures of DNQ and cross-linker.

Measurement. Number- and weight-average molecular weights (M_n and M_w) were evaluated by size exclusion chromatography (SEC) on Waters Alliance e2695 equipped with following features: pump, 2489 UV/Vis detector, two polystyrene gel columns of TSK Gel α–2500, and TSK Gel α–4000 (TOSOH) based on a conventional calibration curve using polystyrene standards. *N*-Methylpyrrolidone (NMP) containing 50 mmol L^{-1} of LiCl and 50 mmol L^{-1} of H_3PO_4 (50 °C) was used as a carrier solvent at a flow rate of 0.4 mL min^{-1}. Thermal analysis was performed on a Seiko EXSTAR 6000 TG/DTA6200 thermal analyzer at a heating rate of 10 °C min^{-1} for thermogravimetry (TG). Seiko EXSTAR 6000 TMA/SS6100 thermal analyzer was also used at a heating rate of 5 °C min^{-1} for glass transition temperature (T_g) and coefficient of thermal expansion (CTE) measurement. Residual stress of cured samples on silicon wafer was evaluated on FLX-3300-T (TOHO) by measuring the curvature radius using a laser at room temperature. Mechanical properties of films such as tensile strength, young's modulus, and elongation were measured on TENSILON at a speed of 5 mm min^{-1}. To observe the cross-sectional patterns using a scanning electron microscope (SEM) with secondary electrons (FE-SEM S4800, Hitachi Ltd.), the specimens were treated to Pt/Pd sputtering. Film thickness was measured by STM-802 (Lambda Å, SCREEN). The accelerative reliability tests were carried out by treating the film on the substrate with Temperature and Humidity Chamber (PI-2ST, TABAI ESPEC CORP.) as Thermal Humidity

Storage (THS) test , with a convection oven for High Temperature Storage (HTS) test, and with Thermal Shock Chamber (TSE-11-A, ESPEC CORP.) as Thermal Cycle (TC) test, respectively. Copper migration test was conducted by using copper patterned substrate (Line and Space, 2/2 µm) stored in thermal and humidity chamber with 3.3 V bias. Abaquas 2018.HF3 was applied to carry out stress simulation of FO-WLP model by FEM.

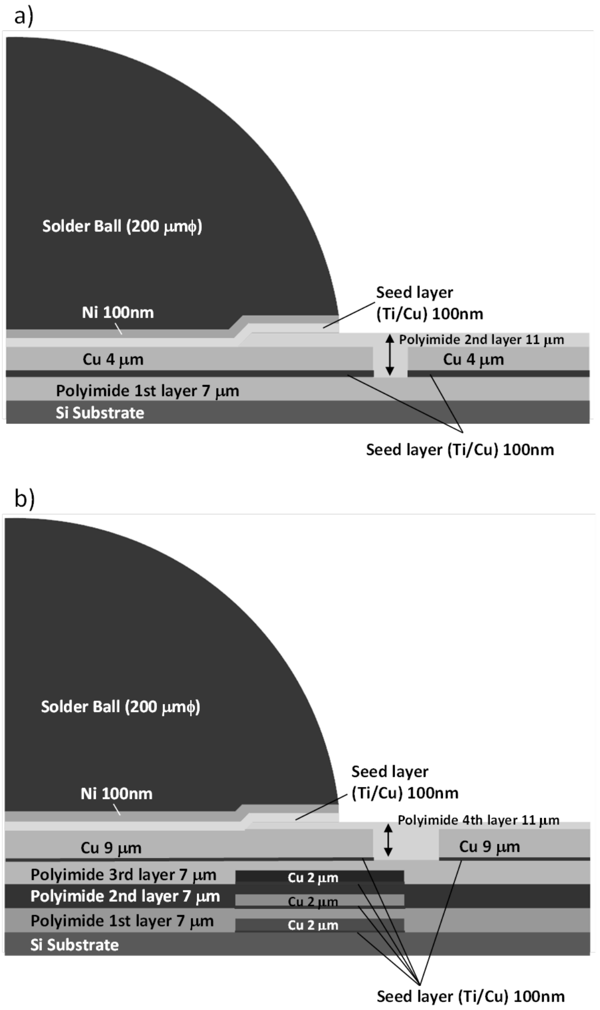

Fig. 2. Mechanical models of a) 2 PI-layer structure and b) 4 PI-layer structure for FEM simulation.

3. Results and discussion

3.1. Stress simulation by FEM

Stress simulation was carried out by Abaquas 2018.HF3 with quasi FO-WLP structure as shown in Fig. 2, and material parameters are summarized in Table 1.

Fig. 3 shows that a single layer RDL stress simulation with parameters of Polyimide A during TC test. The highest stress was observed at the top corner between copper and polyimide, especially, during cooling process of TC test. From this data, it is safe to say that crack during TC test may be occurring at high stressed regions.

Table 1. Material parameters for FEM simulation.

Material	Modulus / GPa			Poisson Ratio			CTE / ppm K^{-1}		
	–55℃	25℃	125℃	–55℃	25℃	125℃	–55℃	25℃	125℃
Polyimide A	4.2^{a}	2.1	1.2^{a}	0.33^{a}	0.35	0.40^{a}	48.2	55.9	69.6
Polyimide B	3.2	1.7	0.8^{a}	0.33^{a}	0.35	0.40^{a}	48.2	55.9	69.6
Ti / Cu	108^{a}	108^{a}	108^{a}	0.34^{a}	0.34^{a}	0.34^{a}	10.7^{a}	12.5^{a}	13.2^{a}
Cu	110^{a}	110	110^{a}	0.34^{a}	0.34	0.34^{a}	14.8	16.6	17.3
Ni	209^{a}	209	209^{a}	0.31^{a}	0.31	0.31^{a}	11.3	13.7	14.4
Solder (Sn)	50^{a}	50	50^{a}	0.36^{a}	0.36	0.36^{a}	25.1^{a}	26.9	27.6^{a}
Si substrate	188^{a}	188	188^{a}	0.28^{a}	0.28	0.28^{a}	1.7	2.6	3.0

[a] Estimated value.

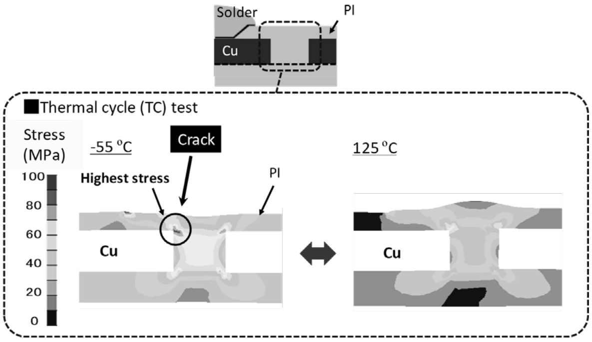

Fig. 3. Stress simulation results by FEM during TC test at –55°C and 125°C).

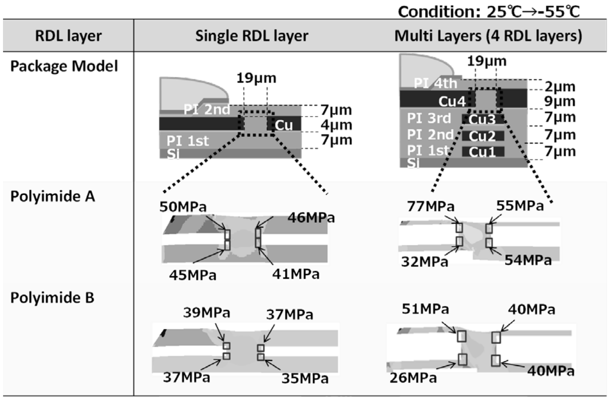

Fig. 4. Stress simulation results by FEM applying for multi layered model during TC test at –55°C.

Moreover, the influence of the number of the RDL layer verses occurrence of crack to the package stress simulation was also investigated. When comparing 2 layer structure to 4 layer structure, 4 layer structure showed rather high stress at the top corner between copper and PI (Fig. 4). In order to prove this phenomenon, comparative data between Polyimide A and Polyimide B revealed the answer. These particular results showed Polyimide B with lower modulus than that of Polyimide A showed decreased stress at the corner between copper and PI even in multi layered structure. Therefore, low modulus PI can be considered to effectively suppress or release the package stress, which is expected to enhance the durability for reliability test.

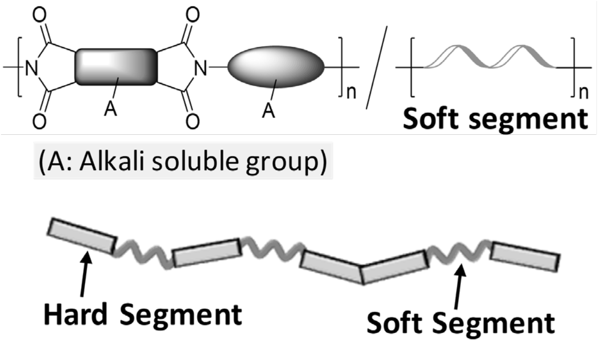

Fig. 5. The schematic model of low modulus PI.

3.2. Development of photosensitive polyimide with high reliability

According to FEM simulation results, low modulus PI (Polyimide B) is one of the suitable materials for making the stress between copper and PI lower. We designed PI backbone with special soft segment as shown in Fig. 5. The coating material of the obtained PI with soft segment containing DNQ, cross-linker and other ingredients has low modulus nature (1.7 GPa). Furthermore, low residual stress including alkaline solubility and fine PSPI patterns were successfully obtained even at the thickness range of 5 to 15 μm. Basic properties are summarized in Table 2. Newly developed PSPI shows high thermal stability, mechanical property and high sensitivity in addition to low modulus and stress nature. Fig. 6 shows the SEM images of the fine patterns. The resolution of PSPI is around 5 μm and 10 μm at a 7 μm film thickness, which could be applicable for the metal sputtering.

Table 2. General properties for PSPIs.

Properties		Measurement Method	Previous type High reliability		Newly developed Low stress	
Curing Condition	°C/min	Oven	200/60	230/60	200/60	230/60
Tensile strength	MPa	Tensile Test	135	135	120	120
Elongation	%	Tensile Test	65	60	100	100
Young's modulus	GPa	Tensile Test	2.1	2.1	1.7	1.7
CTE	ppm/°C	TMA	60	58	58	55
Residual stress	MPa	Bending Bow	28	29	20	20
5% weight loss temp.	°C	TGA	340	350	340	350
T_g	°C	TMA	270	280	275	280
Volume resistance	Ωcm	LCR meter	>1.0x10^{17}	>1.0x10^{17}	>1.0x10^{17}	>1.0x10^{17}
Surface resistance	Ω/□	LCR meter	>1.0x10^{14}	>1.0x10^{14}	>1.0x10^{14}	>1.0x10^{14}
Breakdown voltage	kV/mm	LCR meter	>400	>400	>400	>400
Photo sensitivity (7μm after Cure)	mJ/cm^2	i-line stepper	300	300	400	400
Water Absorption	%	TGA	1.0	1.0	0.8	0.8

3.3. Reliability and copper compatibility of photosensitive polyimide

Reliability tests for the newly developed PSPI with low modulus and low residual stress included TC test, HTS test, and copper migration test. The condition for TC-B test was 1000 cycles at –55 °C to 125 °C. The result of this reliability test was successful, which resulted with no crack.

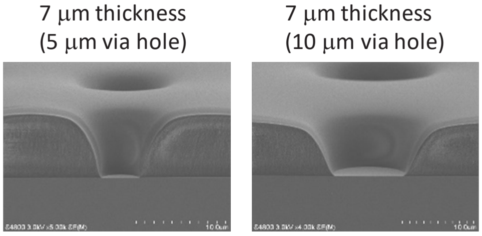

Fig. 6. Cross-sectional view of via patterns for newly developed PSPI.

The other issue regarding reliability is the delamination between copper and PSPI during HTS. Although there is no delamination after cure, delamination and void build-up tend to occur during and after HTS at a condition of 150 °C for 1000 hours. Through a detailed observation by SEM, the interface where delamination and void build-up doesn't occur between copper and PI, rather it occur between copper and copper oxide layers (Fig. 7 a)). Fig. 7 b) shows the interface by secondary ion mass spectrometry (SIMS) to understand the changes during HTS. Horizontal axis is the depth of copper and PI layers and vertical axis is the detection intensity of various elements. After curing, copper oxide was not formed because curing condition was inert. However, copper oxide was generated after HTS. This result indicates diffusion of copper ion into polyimide and oxidation of copper is taking place during HTS. Therefore, in order to prevent copper oxidation, an introduction of anti-copper oxidant into newly developed PSPI was necessary to suppress copper oxidation. Evidently, when we introduced an anti-copper oxidants into our newly developed PSPI, it successfully suppressed the growth of copper oxide and the diffusion of copper ion.

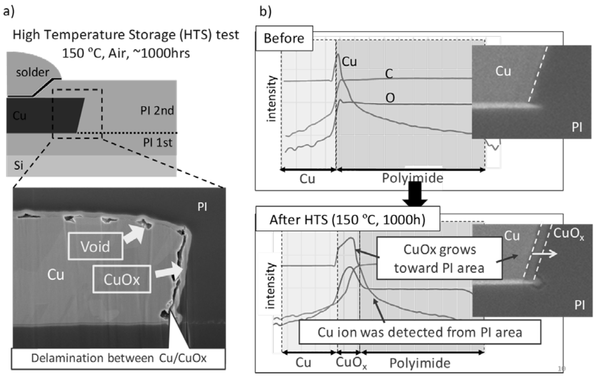

Fig. 7. a) Cross-sectional view of the test vehicle, b) SIMS analysis before/after HTS.

Finally, the insulation property of PSPI called copper migration was investigated by bias HAST with 2 μm line and space copper electrode. The result indicates that the reliability of PSPI is quite high because of its ability to keep the resistivity even after THS test at a condition of 130 °C, 85%RH and 3.3 V for 300 hours (Fig. 8).

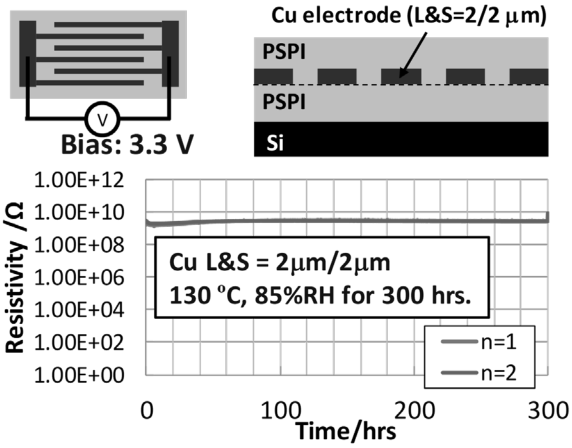

Fig. 8. The result of copper migration test under bias HAST condition (2 μm line and space copper electrode, 130 °C, 85%RH and 3.3 V for 300 hours).

4. Conclusion

We have investigated the stress effect of polyimide on copper multi-layer structures by FEM simulation. Polyimide designed with soft segment which has low modulus and low residual stress tends to decrease the stress at the corner between copper and PI even in multi layered structure.

The result of PSPI composition based on PI with soft segment when utilized on quasi FO-WLP structure showed promising durability result without crack after TC-B test. In addition, delamination between copper and copper oxide can be successfully suppressed by introducing anti-copper oxidant into PSPI. Moreover, newly developed PSPI showed excellent insulation property investigated by bias HAST using 2 μm line and space copper electrode.

This material is expected to make huge impact and contributions to enhance the reliability of advanced semiconductor packaging.

References

1. M. Takegoshi, N. Suzuki, M. Oze, and T. Ikeuchi, *J. Japan Institute of Electronics Packaging*, **15** (2012) 148.
2. M. Brunbauer, E. Fergut, G. Beer, T. Meyeer, H. Hedler, J. Belonio, E. Nomura, K. Kikuchi, and K. Kobayashi, *Electronic Comp. Technol. Conf. ECTC 2006*, **56th** (2006) 5.
3. F. Toyokawa, Y. Shibasaki, and M. Ueda, *Polym. J.*, **37** (2005) 517.
4. K. Iwashita, T. Hattori, S. Ando, F. Toyokawa, and M. Ueda, *J. Photopolym. Sci. Technol.*, **19** (2006) 281.
5. T. Minegishi, S. Ando, F. Toyokawa, and M. Ueda, *J. Photopolym. Sci. Technol.*, **19** (2006) 281.
6. T. Sasaki, *J. Photopolym. Sci. Technol.*, **29** (2016) 380.
7. M. Tomikawa, S. Yoshida, and N. Okamoto, *Polym. Prep. Jpn.*, **56** (2007) 4899.
8. M. Tomikawa, M. Suwa, S. Yoshida, Y. Fujita, R. Okuda, and G. Ohbayashi, *J. Photopolym. Sci. Technol.*, **13** (2000) 357.

Technical Paper

Journal of Photopolymer Science and Technology
Volume 34, Number 2 (2021) 201－204 ©2021SPST

Effect of Cross-linker on Photosensitive Polyimide to Achieve Full Imidization and Lower Stress for Good Reliability

Ayaka Azuma*, Satoshi Abe, and Mamoru Sasaki

Technology Development Center, HD MicroSystems, Ltd.
13-1, Higashi-cho 4-chome, Hitachi-shi, Ibaraki 317-8555, Japan
**ayaka.azuma@hdms.co.jp*

Advanced packaging technology requires low temp. curable and low residual stress material as dielectric layer. Because wafer warpage will be increased with increasing the number of redistribution layers (RDLs) and higher residual stress could induce reliability failure due to cracking and delamination. One method to make residual stress lower is to decrease curing temperature. However, lower warpage by decreasing cure temp. is in a trade-off relation with lower reliability performance due to insufficient imidization ratio of polyimide dielectric layer. To overcome the trade-off relationship, we investigated the effects of number of functional groups and backbone in cross-linker agent. High imidization and low residual stress by curing at 160deg.C have been demonstrated by applying bi-functional cross-linking agent.

Keyword: Polyimide, High imidization, Low stress, Cross-linker, Ultra-low temp cure

1. Introduction

Due to the excellent thermal, mechanical and electrical properties as well as good chemical resistance, polyimide (PI) and poly(benzoxazole) (PBO) have been widely used as stress buffer coatings and redistribution layers (RDL) for packages that have copper re-routing distribution layers to improve the reliability of semiconductor devices [1, 2].

Package structures have been developed to achieve higher performance, downsizing, and cost reduction of electronic devices. Among them, Fan-out packages such as FOWLP (Fan-Out Wafer Level Package) FOPLP (Fan-Out Panel Level Package) are attracting most attention as a new packaging technology［3-5］. Dielectric material used for FOWLPs requires various characteristics such as insulation, low warpage, high reliability, and adhesion strength for metals used as RDL. Particularly in recent years, lower stress has been required to reduce the wafer warpage by increasing the number of RDL and the thinning of chip to prevent failure from cracking and delamination.

Low temperature curing is one method to reduce the warpage. However, lower warpage by lower curing temperature is in a trade-off relation with poor reliability performance due to insufficient imidization ratio.

In order to improve imidization ratio, addition of imidization accelerator such as a thermal acid generator or a thermal base generator can be mentioned, but it is conceivable that these additives remain in the film cure at low temperature. Residual acid and base may corrode Cu wiring and reduce insulation reliability. Therefore, instead of using a new additive, we focused on cross-linker, which is material contained in photosensitive composition and occupies high proportion. Then, cross-linker structure was studied to achieve both high imidization ratio and low stress by curing at 160 °C.

2. Experimental

2.1. Materials

Polyamic acid ester as polyimide precursor was synthesized with tetracarboxylic acid dianhydride, diamine and alcohol which is

Received April 1, 2021
Accepted April 9, 2021

introduced to side chain of polyimide precursor. Monomers, additives and solvents were used as purchased.

2.2. Evaluation of a model composition

A photosensitive polyamic acid ester varnish was prepared by adding the polymer, photo-initiator, cross-linker, adhesion promoter and other additives to solvent. The varnish was filtered before being spin-coated onto silicon wafers and then prebaked on a hot plate at 100 °C for 2 minutes and 110 °C for 2 minutes. The prebaked wafer was exposed to broadband (g, h, i-line) radiation using a broadband alighner and developed in cyclopentanone by puddle method. The patterned wafer was finally cured at 160 °C for 2 hours under nitrogen atmosphere.

2.3. Calculation of imidization ratio

Imidization ratio calculated by transmission method of FT-IR. Aromatic ring (1500 cm^{-1}) and C－N vibration mode (1370 cm^{-1}) were used to calculate the imidization ratio. The peak of an aromatic ring was reference to normalize C－N peak. The imidization ratio is defined as 0% for prebaked film and 100% for the film cured at 375°C. The imidization ratio was calculated by the following equation,

$$Imidizatio\ raio\ (\%) = \frac{Area\ of\ around\ 1370\ cm^{-1}}{Area\ of\ around\ 1500\ cm^{-1}} \times 100$$

2.4. Measurement of residual stress

The varnish was coated, soft-baked and blanket exposed onto 6inch silicon wafers and then cured at 160 °C for 2 hours under nitrogen flow. The residual stress of the samples was measured by a thin film stress measurement system.

3. Results and discussion

3.1. Screening of cross-linkers

Various acrylate type cross-linkers and the composition of polyimide precursors were evaluated.

First, we investigated the effect of the number of functional groups of cross-likers. The structure of the cross-linker is shown in Figure 1. Mono-, bis-, tetra- and hexa-functional cross-linkers were evaluated. Amount of cross-linker was decided so that the number of functional groups were equivalent.

Then, we investigated the effect of backbone on the cross-linkers with the most effective functional number.

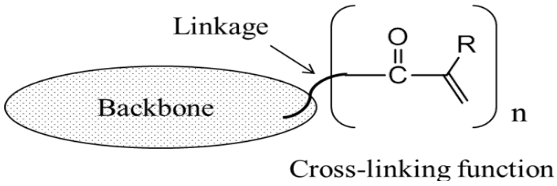

Fig.1 Structure of cross-linker

3.2. Results of Imidization ratio

The imidization ratio was evaluated for a 10μm cured film thickness. As shown in table 1, we found bi-functional type cross-linker showed high imidization ratio even at 160 °C of cure temp. compared to mono-, or multi-functional type. Then, we also found possibility that the imidization ratio can be improved only by selecting the suitable cross-linker, which is essential in the product composition, without using another additive such as a cyclization accelerator.

Table 1 Imidization ratio for each functional cross-linker

Run	Number of functional groups	Imidization ratio (%)
1	no cross-linker	41.5
2	1	35.8
3	**2**	**70.3**
4	4	22.9
5	6	25.6

It is presumed that the imidization ratio was lower by using mono-functional type cross-linker since the polyimide main chain has large side chain made of the cross-linker and reduce flexibility to the polyimde main chain. It is also considered to the composition which no cross-linker is added.

The imidization raio on Run3 showed relatively higher value than the other experimental runs. It is presumed that bi-functional cross-linker polymerize by itself at exposure step, then the polyacrylate acts as a plasticizer and induce high imidization ratio.

On the other hand, the multi-functional cross-linker didn't show the acceleration of imidization. it is presumed that cross-linking structure of multi-functional cross-linker was complex and less flexible than bi-functional cross-linker.

Since the bi-functional cross-linker showed higher imidization ratio, we evaluated the effect of the backbone of cross-linker on the imidization ratio. The results are shown in Table 2.

Table 2 Results of imidization ratio of bi-functional group type cross-linker

Run	Backbone	Rigidity	Imidization ratio (%)
3	**Aliphatic type**	**Flexible**	**70.3**
6	Cyclo-aliphatic type	Rigid	27.6
7	Heterocyclic type	Rigid	27.9
8	**Bisphenol type**	**Flexible**	**86.0**

From the Table 2, the influence of backbone was significant, and the cross-linker with a flexible structure showed higher imidization ratio than rigid type structure.

Based on these results, it was revealed that bi-functional flexible backbone cross-linkers are remarkable imidization promotor.

3.3. Results of residual stress

Next, the effect of the number of functional groups on residual stress was investigated. Then Run 8, which showed higher imidization ratio, was added to evaluation sample. The residual stress was evaluated for a 10μm cured film thickness. The result is shown in Table 3.

Table 3 Results of residual stress

Run	Number of functional groups	Residual stress (MPa)
1	no cross-linker	25.9
2	1	26.0
3	**2**	**19.6**
4	4	22.0
5	6	22.8
8	**2**	**19.7**

As shown in table 3, bi-functional cross-linker was also effective to reduce residual stress compared to mono- or multi-functional cross-linkers. Run 3 and Run 8, which showed high imidization ratio, showed lower stress under 20MPa.

3.4. Discussion

For imidization ratio, the presence of plasticizer accelerates thermal imidization reaction [6]. Therefore, we focused on the Tg of homopolymer made from cross-linker.

Table 4 Tg of homopolymer by cross-linkers

Run	Number of functional groups	Tg of cross-linker homopolymer (℃)
1	no cross-linker	-
2	1	140
3	2	23
4	4	108
5	6	>250
8	2	75

As shown in table 4, effective cross-linker on imidization ratio and residual stress showed lower Tg of homopolymer than 100 ℃. Then, the homopolymer of cross-linker seems to act as plasticizer at curing process and accelerate thermal imidization. Run 4 also showed Tg below the cure temperature. However, it is presumed that the mobility of the polyimide precursor chain with tetrafunctional cross-linker was more restricted than that with bi-functional cross-linkers because cross-linking density with tetrafunctional cross-linker was higher. The lower imidization ratio with tetrafunctional cross-linker also suggested higher the cross-linking.

Not only imidization but also stress was affected by the number of functional groups of cross-linker. The stress is calculated by the following equation [7].

$$\sigma = K\ (\alpha p\ -\alpha s)(Tp-T)Ep \qquad (1)$$

σ: residual stress, αp : CTE for polyimide, αs: CTE for silicon wafer , Tp: glass transition temperature of polyimide , T: measuring temperature , Ep: Young's modulus of polyimide , K:constant

The equation indicates that lower Young's modulus, lower Tg and lower CTE can reduce the stress. Since the bi-functional cross-linker had higher imidization ratio, it is considered that the cross-linking density was lower than that of other cross-linkers. It is presumed that the decrease in crosslink density reduced the young modulus and CTE. Furthermore, Tg of homopolymer made from cross-linkers also affected Tg of polyimde film. For these reasons, the composition with bi-functional cross-linker showed lower residual stress.

Consequently, the adoption of bi-functional cross-linker having a flexible backbone is an effective method, not only for higher imidization ratio but also for residual stress reduction. By achieving high imidization ratio and low stress, it is expected that good reliability can be obtained even by curing at 160 ℃.

3. Conclusion

We evaluated the effect of the number of functional groups of cross-linkers. Higher imidization ratio and low stress can be achieved by selecting a suitable bi-functional cross-linker by curing even at 160 ℃ cure. It seems that bi-functional cross-linkers with flexible backbone act as plasticizer by polymerization during exposure step and that helps acceleration of imidization during curing step. For residual stress, to control cross-linking density and Tg are effective to reduce of residual stress. We can conclude the adoption of bi-functional cross-linker having a flexible backbone is an effective method for both imidization ratio and residual stress.

References

1. A. Saiki, S. Harada, T. Okubo, K. Mukai, and T. Kimura, *J. Electrochem. Soc.*, **124** (1977) 1619.
2. K. Katoh, Latest Technology of Stress Buffer Material for Semiconductor Application: Nihon Gomu Kyoukai-shi, Vol.58, No.2, p-20-25 (2012)
3. Y. Muno, et al, “FOWLP/FOPLP/Sentan Package Shijoubunnseki,” *Global Net Corp.*, (2020).
4. D.-C. Hu, W.-L. Yeh, Y.-H. Chen, R. Tain, “*2/2μm Embedded Fine Line Technology for Organic Interposer Applications*”, 66th Electronic Comp. Technol. Conf., Las Vegas, NV, 147-152, (2016).
5. S. Brokar, “*3D-technology-A System Perspective*”, in International 3D-System Integration Conference, 1-14 (2008).
6. Y. Shirai, S. Tokiwa, T. Kawauchi, T. Takeichi, and T. Sasaki. *J. Photopolym. Sci. Technol.,* **25**. (2012) 389.
7. M. Ree, C-W. Chu, and M. J. Goldberg *J. Appl. Phys.,* **75** (1994) 1410.

Communication

Journal of Photopolymer Science and Technology
Volume 34, Number 2 (2021) 205−211 ©2021SPST

Purification Method for Achieving Low Trace Metals in Ultra-High Purity Chemicals

**Mitsuaki Kobayashi[1]*, Yukihisa Okada[1], Takaaki Shirai[1], Osamu Sawajiri[1],
Robert Gieger[2], and Majid Entezarian[2]**

[1] *3M Japan Innovation Ltd, Separation and Purification Sciences Division, Minami-Hashimoto, Chuo-ku, Sagamihara-shi, Kanagawa 252-5285, Japan*
[2] *3M Purification and Separation Science Division, 400 Research Parkway, Meriden CT, USA 06450*
kobayashi.m@mmm.com

The high purity requirements of materials used in semiconductor manufacturing are being pushed to unprecedented levels as demand for reliability in computer processors over increasingly longer lifetimes continues to rise. The production of these high purity chemicals requires new purification methods and technologies where the metal concentrations of low parts per billion (ppb) were effectively reduced to low parts per trillion (ppt). The new approach discussed in this paper would present a method for dividing the fluid through micro-channels that form tortuous pathways. These micro-channels allow for further dividing and converging of the fluid thereby presenting the metal species to the purifying surfaces throughout the porous matrix. The ion exchange capability was a function of the concentration and the presence of the species in the solution. Two ion exchange chemistries of strong acid and chelating were made into these structures and their purification performances were assessed and compared in terms of removal efficiencies. Furthermore, these two chemistries were evaluated in series to demonstrate the overall synergistic purification capabilities.

Keywords: High purity chemicals, Metal reduction, Ion exchange, Advanced photolithography

1.Introduction

In recent years, the electronic devices have becoming more complex. The line / pattern size in electronic devices is decreasing to levels that impurities play a critical role in the manufacturing, function, and longevity of advanced devices. These impurities are usually classified as cations usually in the form of metal ions, anions of chlorine or hydroxide, or as organic compounds in the form of low to high molecular weight. The removal of these impurities from any fluid that comes in contact with these devices during the manufacturing process is paramount to improving yields and enabling these devices that will shape the future technological advances in medical, diagnostics, communications, artificial intelligence and many more applications. The fluids are Ultra-Pure Water (UPW), etchants, cleaning solutions, Photoresists, developers, coatings, and Chemical Mechanical Planarization (CMP) slurries [1].

There are several purification methods that can be used for purifying fluids. These are evaporation, distillation, affinity purification, filtration, adsorption, fractionation, electrolysis, and ion exchange to just name a few. The focus of this study was the use of ion exchange mechanism. It is stated that the ion exchange process is controlled solely by the diffusion, which is dictated by the materials micro-. and macro-structures [2]. One approach that has been utilized to overcome some of the diffusion challenges is to reduce the pore size by utilizing a membrane and grafting an ion exchange on to the membrane surface [3]. Providing high ion exchange capacity does not always results in higher purification outcome. This is more pronounced when approaching very low concentrations for the start. When approaching low ppb metals level and the objective is to achieve low ppt, the diffusion is becoming the rate limiting factor. New approach to improve diffusion is reducing the diffusion path. This is achieved by flowing the fluid through narrower channels. Assuming the ionic species are

Received March 30, 2021
Accepted April 14, 2021

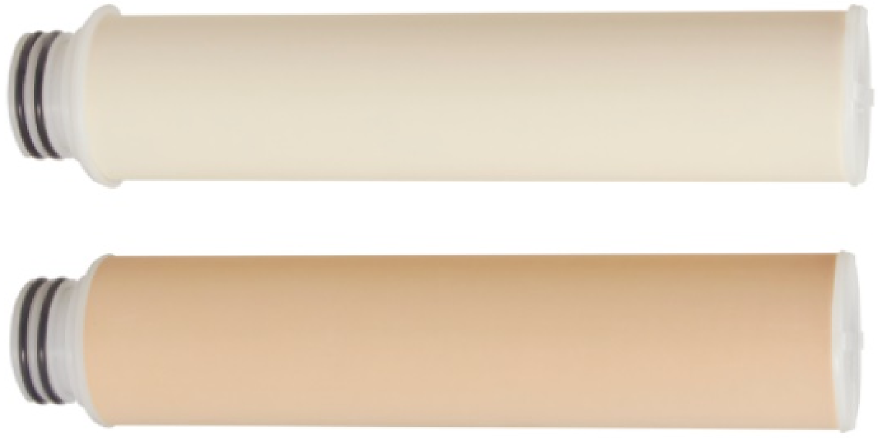

Fig. 1. Photos of two types of 3M^{TM} Metal Ion Purifier, APP purifier (upper) and SCP purifier (lower).

the center of the channel, which would be the farthest from the channel walls, the reduction of the channel width directly reduces the diffusion path and reducing the diffusion time. Another approach is to increase the surface contact area between the fluid and the active ion exchange surface, or residence time. Using smaller pore sizes, increasing number of pores, and lengthening of the porous structure would result in increased contact between the fluid and the active surface. Furthermore, dividing the fluid to numerous channels and converging and diverging the stream increases mixing the likelihood of the species coming in contact with active surfaces. The 3M^{TM} Metal Ion Purifiers are building on the above diffusion-controlled parameters by presenting the ion exchange in an immobilized porous micro-channel microstructure. This structure is a porous tubular format, with a similar industry form factor to filtration cartridges. The interaction of the fluid and the microporous immobilized structure is of great interest.

2. Experimental

In this study, two types of 3M^{TM} immobilized ion exchange resin products were evaluated, as shown in Fig. 1. One type is composed of strong acid cation exchange chemistry, identified as "SCP purifier". The other type is based on a chelating chemistry and is identified as "APP purifier". SCP and APP represent the model name of two types of 3M^{TM}, Metal Ion Purifier, respectively. The products were cleaned by 3M^{TM} purification technology.

Metals in organic solution were analyzed using Agilent 8900 ICP-QQQ instruments and metals in UPW were analyzed using Agilent 7900 ICP-MS instruments. System was washed with acid several times to obtain a below detection samples before running the tests. Controls were incorporated into the test plan to ensure the elimination of extraneous factors. The sample aliquots were collected by volume intervals processed through the ion exchange blocks.

An effective surface area was measured in use of a Quantachrome (Anton-Parr) Autosorb IQ2-MP. The samples were placed in 9 mm tubes. Outgassing was performed at 60 °C for 14 hours prior to analysis under < 20 mTorr of pressure. The samples were analyzed at liquid nitrogen temperature (~77 K) using ultra high purity nitrogen gas. Void volume was determined using helium. 16 points were taken (adsorption branch) from 0.01 P/Po to 0.3 P/Po. The points between 0.05 P/Po and 0.3 P/Po were fit to the BET equation which defined by S. Brunauer, P.H. Emmett, and E. Teller.

The purifier was initially dry. The dry purifier was so wetted that the purifier works sufficiently. The dry purifier was soaked in an operating fluid. The purifier was mounted in a housing and flushed in minimum of 2 BVs (bed volume) with the fluid before a purification. In pre-conditioning test, 10-inch cartridge was soaked in UPW with the specific resistance of more than 18.2 MΩcm for 12 hours and flushed by 10 L of UPW. The UPW filtrate was collected in Perfluoroalkoxy alkane (PFA) bottles at 0 L, 6 L, 8 L, and 10 L. The metal concentration was analyzed by Agilent 7900 ICP-MS.

The schematic diagram for performance test was show in Fig. 2. Electronic-grade (EL-grade) 1-Methoxy-2-propanyl acetate (PGMEA) was transferred into an ultra-pure PFA vessel in a pressure tank and pushed through the system by increasing the pressure of the pressure tank. High

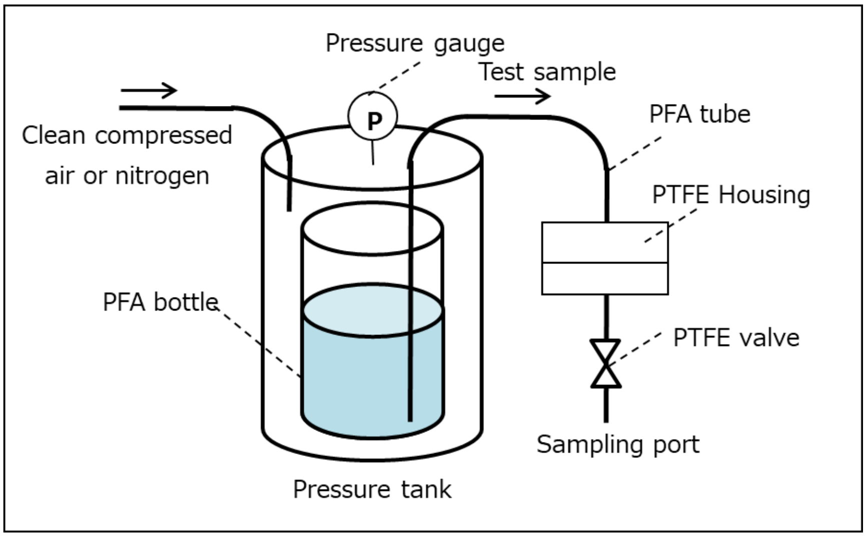

Fig. 2. Schematic diagram for the purifier performance test.

purity air was used to pressurized and maintain a constant pressure. The test pressure was adjusted by a compressed air. The clean air was filtered to 0.003 µm rating to ensure no particulate was introduced into the fluid through the line. Prior to starting the test, the 2-inch purifier was installed into the high purity polytetrafluoroethylene (PTFE) housing and sealed to prevent any bypass or leaks. Downstream of the housing, a needle valve was installed for adjusting the flow rate. The 2-inch purifier were soaked in PGEMA for a minimum of 12 hours to ensure the structure is fully wetted by PGMEA and the air in the pores is replaced with the PGMEA in order to maximize the utilization of the ion exchange capacity. The purifier was flushed by 200 mL of PGMEA and was collected in high purity PFA bottles. After completion of the pre-conditioning, the PGMEA in the housing was emptied. The PGMEA spiked standard metal solution the initial 500 mL was discarded, and then subsequent filtrate was collected in high purity PFA bottles. The untreated sample was labeled as "Initial". All the samples were sealed immediately after filling and opened only when ready for metal analysis by Agilent 8900 ICP-QQQ. More than twenty metal elements were analyzed to assess the effectiveness of each ion exchange chemistry. The metal concentration of spiked PGMEA was around 1 ppb.

3. Results and discussion

3.1. Reaction rate

Generally, the reversible reaction formular of an ion exchange resin is expressed by (1)

$$\overline{\text{R-H}}+\text{M}^{+} \rightleftarrows \overline{\text{R-M}}+\text{H}^{+} \quad (1)$$

where $\overline{\text{R-H}}$ and $\overline{\text{R-M}}$ represents an ion exchange resin bonded with a hydrogen, H, and metal, M, respectively.

The forward reaction velocity v_f and the backward reaction velocity v_b are written by (2) and (3), respectively.

$$v_f = \alpha \left[\overline{R\text{-}H}\right]\left[M^{+}\right] \quad (2)$$

$$v_b = \beta \left[\overline{R\text{-}M}\right]\left[H^{+}\right] \quad (3)$$

where α, β are reaction rate constant for forward and backward reaction, respectively, which strongly related to diffusion velocity in the ion exchange layer.

When fluid with metal ion M^+ passes through the ion exchange layer with the thickness δx at a liner velocity LV for δt, as shown in Fig. 3. Here LV is the amount of the fluid which flowed for δt per a unit surface.

A metal variation δM^{+} is shown as

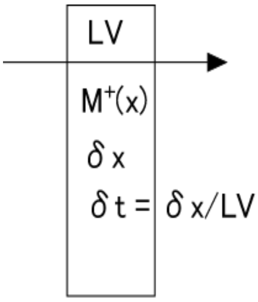

Fig. 3. Schematic diagram of fluid flow passing through ion exchange layer.

$$\delta M^+ = \delta t(v_f - v_b) = (\delta x/LV)(-\alpha\,[\overline{R\text{-}H}][M^+] + \beta[\overline{R\text{-}M}][H^+]) \quad (4)$$

Initially, an ion exchange resin has initially a hydrogen form $[\overline{R\text{-}H}]$. Then $[\overline{R\text{-}H}] \gg [M^+], [\overline{R\text{-}M}], [H^+]$

$$\delta M^+/[M^+] \simeq (\delta x/LV)(-\alpha\,[\overline{R\text{-}H}]) \quad (5)$$

Metal reduction ratio, $\delta M^+/[M^+]$, is proportional to $[\overline{R\text{-}H}]$ and inversely proportional to LV. Also, the metal concentration is a function of the depth, x, Thus the thicker the ion exchange layer, the more is the metal reduction.

3M^{TM} immobilized ion exchange resin technology enabled a purifier with thick ion exchange layer, *i.e.* depth purifier, as shown in Fig. 4. The depth purifier is more than 100 times as thick as membrane filters. The thick porous micro-channel microstructure enabled to increase. It is seemed that the depth is more effective than membrane filter for trace metal reduction.

While the extreme minimum metal ion concentration $[M^+]_{min}$ was obtained at $\delta M^+ = 0$, that is,

$$[M^+]_{min} = (\beta/\alpha)\,[\overline{R\text{-}M}][H^+]/[\overline{R\text{-}H}] \quad (6)$$

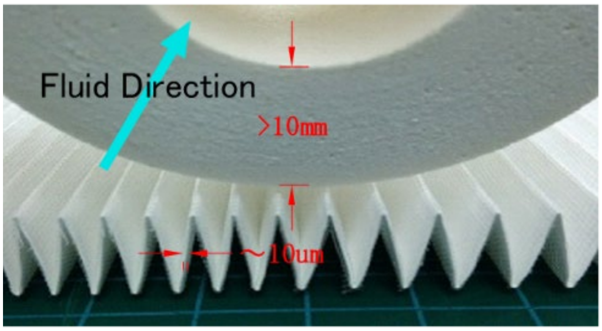

Fig. 4. Photos of the cross section of the 3M^{TM} Metal Ion Purifier and a membrane filter.

The extreme minimum metal ion concentration $[M^+]_{min}$ depends on the metal concentration $[\overline{R\text{-}M}]$. The depth filter may be able to achieve less minimum metal ion concentration $[M^+]_{min}$ than a membrane filter, because the depth filter can supply continuously a fresh layer of $[\overline{R\text{-}H}]$ in the downstream. Also it is very important to reduce the initial metal contaminations, $[\overline{R\text{-}M}]$, in ion exchange layer in order to lower the $[M^+]_{min}$. 3M^{TM} purification technology enabled to reduce the metal extraction less than 50 ppt in UPW.

3.2. Surface area

The cross section of the 10-inch 3M^{TM} Metal Ion Purifier was shown in Fig. 5. The purifier was tubular with around 15 mm thick and single open end (SOE) where the one end of the tubular was closed by flat end cap and the other end was open through 222-connector. The fluid flowed into from the tubular surface and came out from the connector. The outer surface area of the tube was about 0.05 m^2. The effective surface area of the purifier was measured by BET to have 32.1 m^2/g and 27.1 m^2/g for the purifier of the APP and SCP purifiers, respectively. The effective surface area of 10inch APP and SCP purifiers were about 8,000 m^2 and 7,500 m^2, respectively, which was extremely larger than the tube surface area. Therefore, it was clarified that the purifiers consisted of porous micro-channel microstructure.

3.3. Pre-conditioning

10-inch SCP was dry. The 10-inch SCP purifier was soaked in UPW for 12 hours and then flushed by UPW at the flow rate of 2 L/min. The other 10-inch

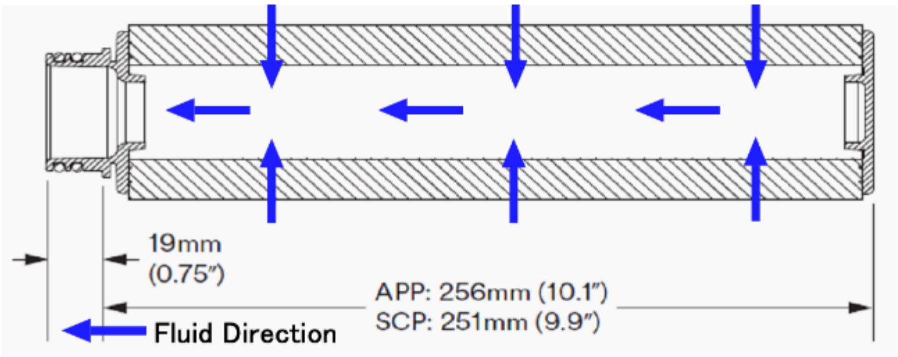

Fig. 5. Cross section of 3M^{TM} Metal Ion Purifier and a fluid direction.

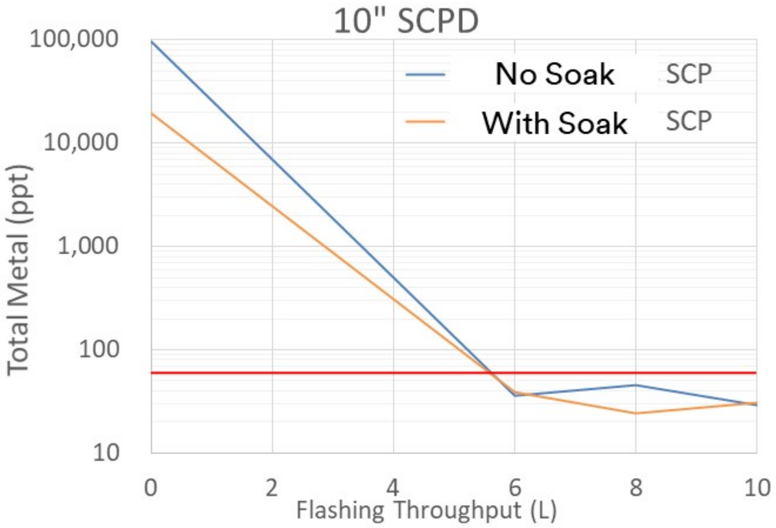

Fig. 6. Pre-condition of SCP purifier.

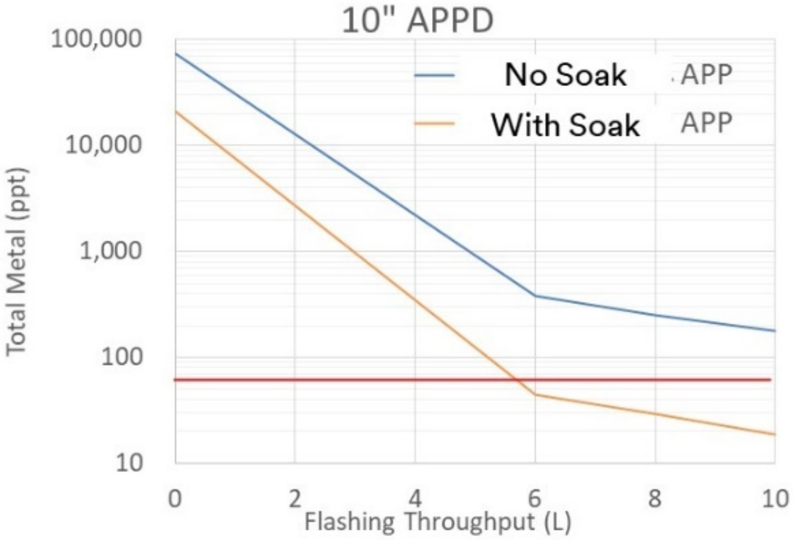

Fig. 7. Pre-condition of APP purifier.

purifier was flushed without soaking. The total trace metal concentration in the filtrate was analyzed by Agilent 7900 ICP-MS, as shown in Fig. 6. The total metal of both SCP purifiers was less than 50 ppt after flushing of 6 L. It was supposed that the low trace metal extraction was owed to increasing contact between the fluid and the active surface by using smaller pore sizes, increasing number of pores, and lengthening of the porous structure. It was clear that 3M^{TM} purification technology could achieve the very high pure SCP purifier with trace metal extraction less than 50 ppt by the increasing contact. The most initial extraction was sodium which seemed to come from the environment and washed out by flushing.

APP purifiers were also flushed in the same manner. The total trace metal was in accordingly with flushing throughput, as shown in Fig. 7. The total metal for the purifier with soaking was less than 50 ppt after flushing of 6 L, while the total metal for the purifier without soaking could not achieve less than 50 ppt even after flushing of 10 L. It is seemed that APP is a little bit slower to be swelled than SCP. It was necessary to swell sufficiently 3M^{TM} Metal Ion Purifier before applying to fluids. It was recommended that the 3M^{TM} Metal Ion Purifier could be swelled sufficiently and flushing.

3.4. Flushing with PGMEA

2-inch purifiers were soaked in PGMEA for 12 hours and then flushed with PGMEA. The trace metal concentration in the filtrate was analyzed by

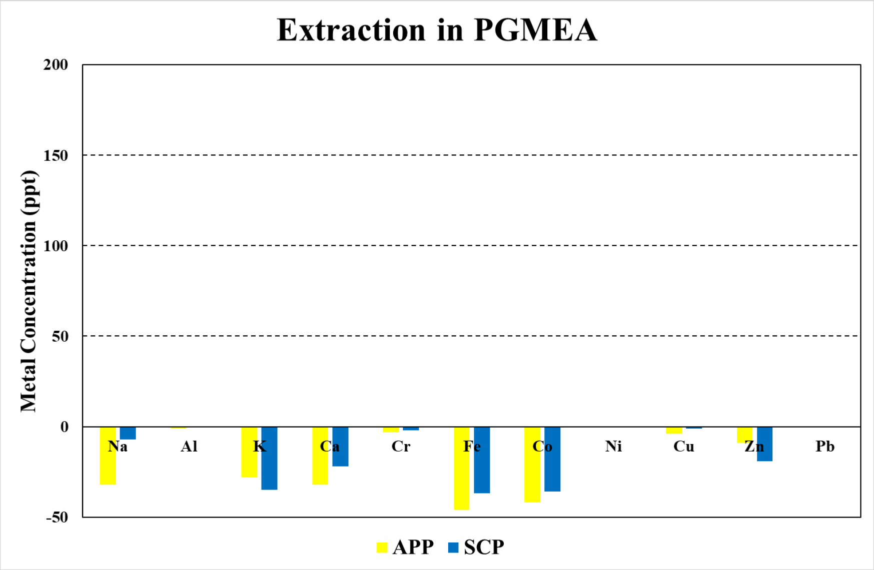

Fig. 8. Metal extraction from the purifier. Negative means reduction.

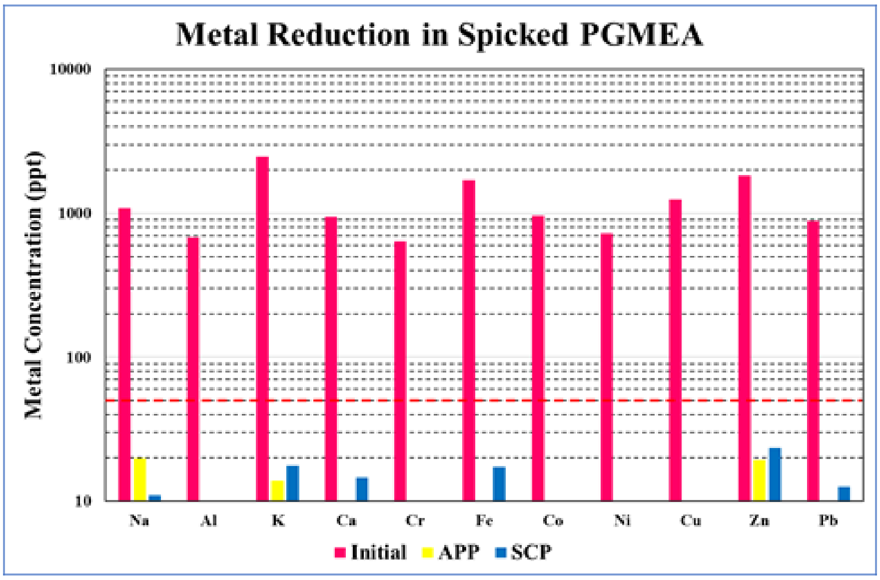

Fig. 9. Metal reduction by APP and SCP purifiers in PGMEA.

Agilent 8900 ICP-QQQ. The difference of trace metal concentration in filtrate from the initial PGMEA was shown in Fig. 8. The negative means the reduction from the initial concentration. Any metal extraction from both purifiers of APP and SCP was not observed.

3.5. Metal reduction results

A PGMEA was spiked by metal standard solution so that metal concentration was around 1 ppb. The PGMEA was filtrated by 3M^{TM} Metal Ion Purifier. The results of metal reduction were shown in Fig. 9. The metals less than the quantitative limit of 10 ppt was not shown in Fig. 9. All metals were reduced either to single digit or double digit ppt levels from low ppb or high ppt levels. Both types of the ion exchange were effective in removing all trace metals. It was found that the SCP purifier could remove more sodium than the APP purifier, while the APP purifier could remove more iron than the SCP Purifier. It was supposed that the difference is came from the ion exchange spices of the APP and SCP purifier. The APP and SCP purifier could compensate each other for trace metal reduction.

4. Conclusion

The fixed pore structure in 3M^{TM} Metal Ion Purifier contains high surface area micro channels which reduces the diffusion path allowing for proximity of the metal species to the active sites and which achieves high cleanness of the active sites. The results of the studies presented in this paper demonstrate that the $3M^{TM}$ immobilized ion exchange resin technology and purification technology can meet the new requirements for trace metals in high purity chemicals to single digit or low double digit ppt levels from low ppb or high ppt levels.

Acknowledgement

The authors would like to acknowledge the contribution of Emiko Toh at corporate research analytical laboratory of 3M Japan Innovation Ltd. for the metal analysis.

References

1. *Yield Enhancement of International Roadmap for Devices and Systems*: (2017)
2. A. Zagorodni, *Ion Exchange Materials,* (2007), Pages 221-241.
3. Y. Tanaka, *Ion Exchange Membranes*, Volume **12** (2015).

Journal of Photopolymer Science and Technology
Volume 34, Number 2 (2021) 213−218 ©2021SPST

Study on Fabrication of X-ray Collimators by X-ray Lithography Using Synchrotron Radiation

Shunya Saegusa[1*], Noriyuki Narukage[2], Yuichi Utsumi[1], and Akinobu Yamaguchi[1]

[1] Laboratory of Advanced Science and Technology for Industry, University of Hyogo,
3-1-2 Kouto, Kamigori, Hyogo 678-1205, Japan
[2] National Astronomical Observatory of Japan,
2-21-1 Osawa, Mitaka, Tokyo 181-8588, Japan
**saesae54@lasti.u-hyogo.ac.jp*

X-ray lithography using synchrotron radiation enables the microfabrication of plastic solid materials in scale from micrometers to millimeters with high aspect and nanoscale surface roughness. We investigate fabrication of X-ray collimator mold for the space telescope using the X-ray lithography. A honeycomb-like structure consisting of hexagonal columns with diameter of several hundred micrometers is required for the X-ray collimator. In this study, target resin molds for manufacturing a metallic X-ray collimator were created from polymethyl methacrylate (PMMA) substrate. We succeeded in producing a honeycomb pillar array structure with diagonal length of 100 μm and its distance of 14.1 μm between pillars.

Keywords: Synchrotron radiation, X-ray, LIGA, Microfabrication

1. Introduction

In 2016, the Focusing Optics X-ray Solar Imager (FOXSI) was started to study particle acceleration and coronal heating on the Sun through unprecedented high-resolution imaging in the X-ray energy band region. An observation device equipped with a telescope and an X-ray detector is launched by a rocket, and soft X-rays and hard X-rays are captured in outer space to continuously photograph the sun at high speed.

The purpose of FOXSI is to understand high-energy phenomena in the solar corona [1-4]. For example, elucidation of the mechanism of nanoflare [5] can be mentioned. This flare is about one billionth of normal flare. However, while the temperature of the normal corona is several million degree Kelvin (MK), it is thought that 10 MK of plasma is generated when nanoflare occurs. Accelerated plasma is called non-thermal plasma and cannot be analyzed without capturing the X-rays generated by the plasma. Information on the position, time, and energy of each X-ray photon can be obtained from the image obtained by FOXSI. It is thought that the understanding of particle acceleration of solar flares will be improved by examining the presence or absence of the constant existence of 10 MK plasma in the solar corona from the obtained information.

This research aims to improve the X-ray collimator [6-9] of the observation device. A X-ray collimator is a component that removes stray light during observation and allows light parallel to the telescope to pass through to reduce image noise. Improvements include spectral accuracy and weight. Improving the spectral accuracy means narrowing the incident angle of the light entering the observation device so that only light with higher parallelism can be extracted. A collimator picks out parallel light by reflecting light inside a metal cylinder, as illustrated in Fig. 1(a). The angle of incidence can be reduced and more parallel light rays can be obtained if the cylinder is longer and if the inner diameter is smaller. Thus, fabricating a cylindrical structure with a high aspect ratio and a small inner diameter will improve spectral accuracy and eliminate noise from stray X-rays.

Weight reduction is very important from the viewpoint of rocket weight limitation. In order to reduce the weight, it is necessary to use a honeycomb structure [10,11] with a large aperture ratio as shown in Fig. 1(b). This structure becomes possible to secure the strength while reducing the

Received April 7, 2021
Accepted May 6, 2021

materials required for manufacturing the collimator, leading to weight reduction. Furthermore, from the viewpoint of strength and X-ray blocking, it is required to make the above structure from metal.

In the previous studies [1-4], a collimator was created using a metal 3D printer to remove light outside 18′ with an aspect ratio of 190. In order to improve the performance, it is necessary to make it finer with a higher aspect ratio. However, a collimator that removes light outside the 14′ with an aspect ratio of 250 is required to have a processing accuracy of about 10 μm, and it is difficult to manufacture due to the limitation of the powder size (about 30 μm). In order to create a finer and higher-aspect structure, attention was focused on the X-ray lithography using the synchrotron radiation (SR) facility New SUBARU, which can perform deep processing on the order of microns [12 -14].

X-ray lithography is the most appropriate technique for the nano- or microfabrication of structures with both nanoscale surface roughness and high aspect ratios. This is because X-ray processing using SR is the only technique to date that has a deep depth of focus and can process large area at once as a top-down process [12–20]. Further, the LIGA process, which combines lithography (LIthographie), electroforming (Galvanoformung), and molding (Abformung), allows for the manufacture of metallic nano- to microscale structures which are otherwise difficult to fabricate.

In this study, we demonstrate deep X-ray lithography for the fabrication of X-ray collimators.

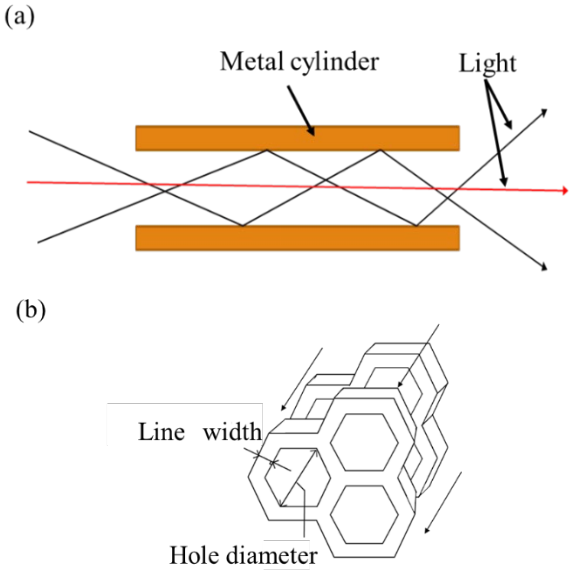

Fig. 1. Schematics of (a) the structure of a collimator in cross-section, (b) a collimator mold comprising laminated honeycomb membranes.

2.Experimental

In X-ray lithography, an X-ray mask is typically placed above the target surface to direct and limit exposure of the substrate. The vertical gap between the X-ray mask and the substrate results in the formation of a tapered structure, which is not desirable for a collimator cylinder. To address this, we employed a novel X-ray masking procedure, illustrated in Fig 2(a). The Au X-ray mask is directly fabricated on the surface of the polymethyl-methacrylate (PMMA) substrate, which improves transferability. The optical photograph in Fig. 2(a) is a typical resulting structure; the example shown produces hexagonal cylinders with an aperture ratio of 70% and a hole diameter of 100 μm. The aperture ratio is defined as the ratio of the area of the hole to the total cross-sectional area of the collimator. Masks to create molds for cylinders with hole diameters of 50, 100, 200, and 300 μm and aperture ratios of 80%, 70%, 60%, and 50% were prepared.

The irradiation experiments were performed using beamline BL11 at the New SUBARU synchrotron radiation facility at the University of Hyogo [14]. The X-ray beam obtained from the bending magnet is condensed using a mirror and subsequently passed through two Be filters to reduce the photon energy to below 2 keV. The energy spectrum of BL11 is shown in Fig. 2(c); the X-ray bandwidth comprises energies between 2 and 8 keV, and has a flux maximum at approximately 5 keV. The operation electron energy of the storage ring was set at 1.5 GeV and the storage current value ranged from 320 to 160 mA. In this operation mode, the storage current decreased exponentially during exposure. The irradiation doses to PMMA in this experiment were 1 J/mm^2 and 3 J/mm^2.

As described above and schematically illustrated in Fig. 2(a), a contact Au metal mask was prepared directly on the surface of 2-mm-thick PMMA substrate, which was purchased from Nippon Jushi Kogyo Co., Ltd. Fig. 2(b) shows a schematic diagram of the experimental setup for X-ray irradiation. The exposure stage was moved vertically over a range of ±50 mm at a speed of 5 mm/s to enable vertical scanning with the beam. The SR dose was controlled by the number of scans, which were performed under 0.05 atm of helium gas that was introduced into the chamber after vacuuming with a scroll pump. The temperature of the irradiated surface was maintained at room temperature by heat exchange with the helium gas. The Au contact mask was fabricated by combining Au electroplating and magnetron sputtering to

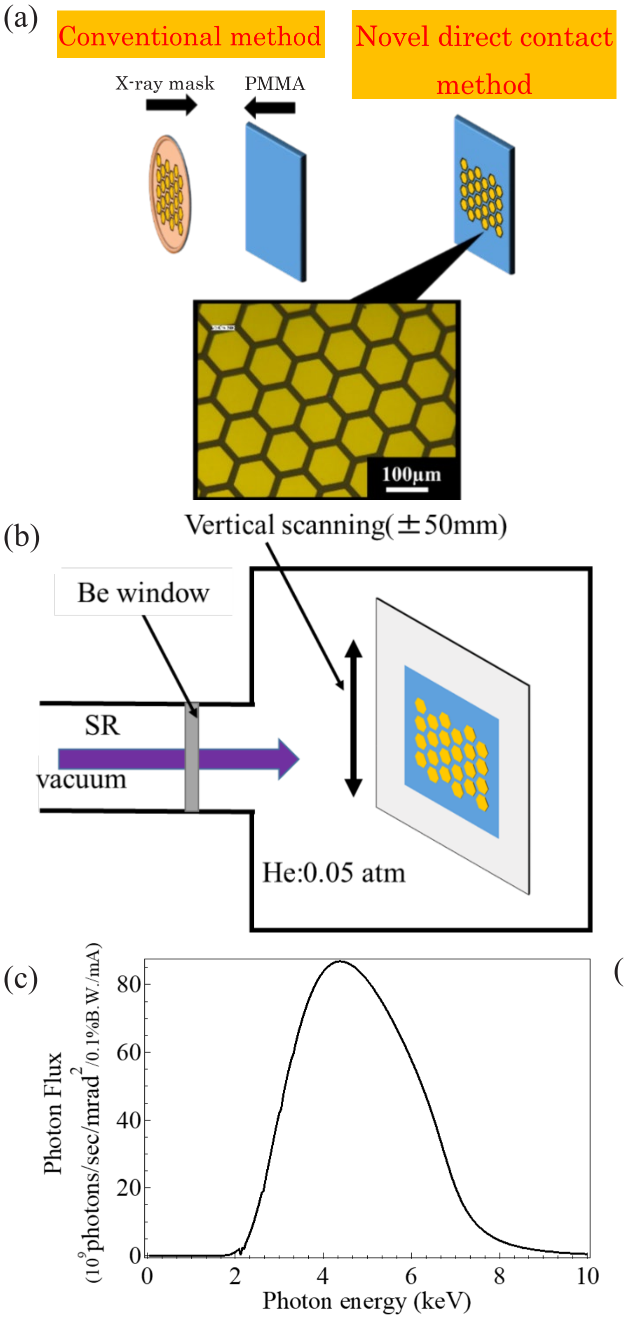

Fig. 2. Schematics of (a) the method and structure of a direct contact X-ray mask, (b) the X-ray exposure experimental setup in the chamber in the beamline BL11 of NewSUBARU at the University of Hyogo, and (c) Photon intensity distribution as a function of photon energy at the beamline BL11.

create an array of hexagonal Au masks, with a hole diameter of about 50 – 300 µm and a distance between hexagons of about 4.51 –76.2 µm. The Au plating solution (Microfab Au640) and sputtering target were purchased from Tanaka Precious Metals Co., Ltd. After irradiation, the PMMA was developed with a GG-developer to prepare the structure. Before Au electroplating, hexagonal patterns were fabricated by UV lithography using Cr glass mask. Tracking dimensional accuracy was measured using an optical microscope.

3. Results and discussion

Scanning electron microscope (SEM) images of typical PMMA molds fabricated with X-ray lithography are shown in Fig. 3 and 4. We found that X-ray mask lithography can produce honeycomb PMMA microstructures with a diameter of 100 – 300 µm, a distance between pillars of 14.1 – 76.3 µm. From SEM images, we found the height was about 300 µm at 1 J/mm^2 and about 550 µm at 3 J/mm^2. Fig. 5 shows summary of topview optical micrographs of the PMMA molds developed after X-ray 1 J/mm^2 irradiation. Here, we found that the pillar structures collapsed under the severer design conditions as pointed by an arrow in Fig. 4 and 5.

In Fig. 4, the part indicated by the arrow is broken. Looking at Fig. 5, it can be seen that the hexagonal structure is not orderly. This is because the hexagonal columns collapse and the distance between the columns is not constant. From pointed by the arrow in Fig.5, a microstructure with a distance between pillars of less than 14.1 µm resulted in collapse. 14.1 µm is the distance when the diameter is 100 µm and the aperture ratio is 70%. In addition, when irradiating at 3 J/mm^2, there was

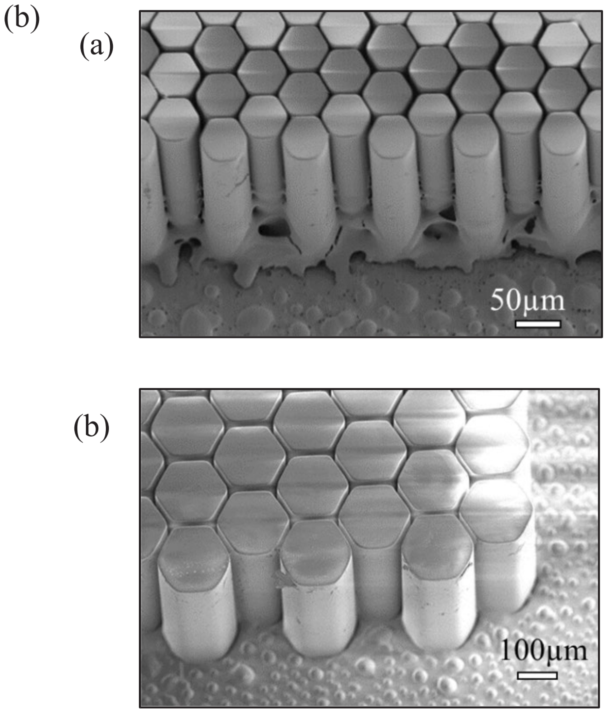

Fig. 3. SEM images of PMMA mold (aperture ratio: 70%, hole diameter: (a) 50 µm, (b) 100 µm,iradiation dose: 1 J/mm^2)

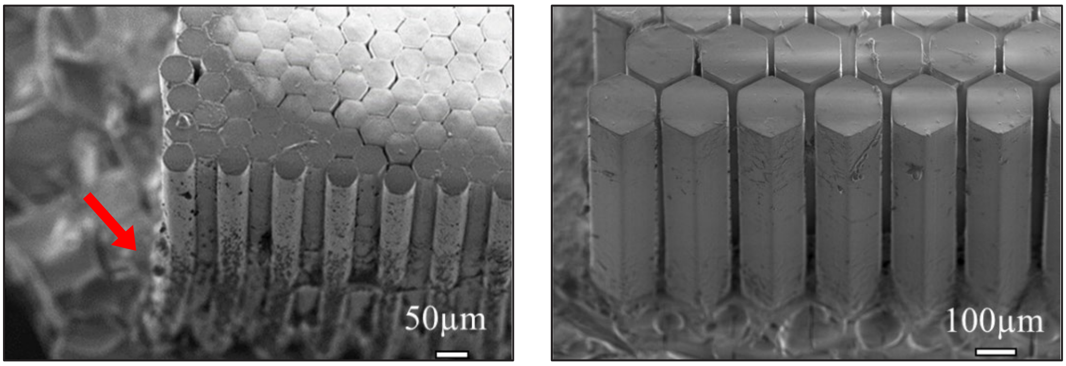

Fig. 4. SEM images of PMMA mold (aperture ratio: 70%, hole diameter: (a) 50 µm, (b) 150 µm, iradiation dose: 3 J/mm^2).

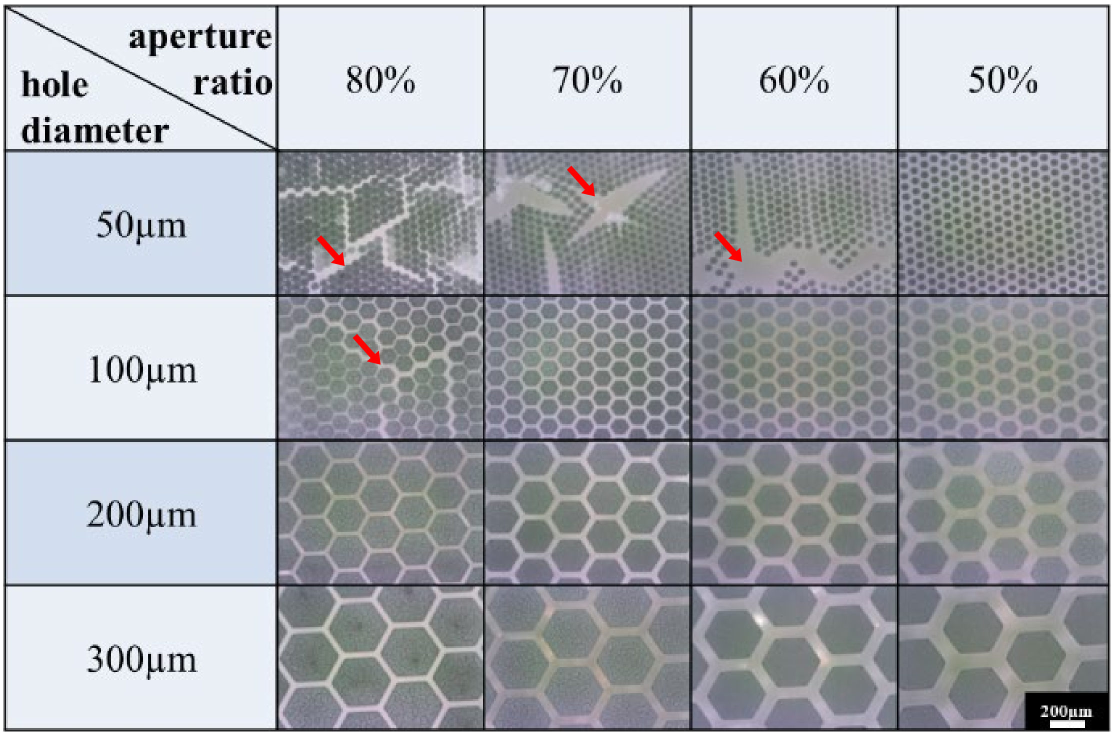

Fig. 5. Optical micrographs of the topview of PMMA molds developed after X-ray exposure.

a part that collapsed in most patterns. This is likely because of the influence of surface tension during development, which, if too large, causes sticking and the collapse of the hexagonal columns. This phenomenon is especially likely to occur when the structure is taken out of the developer.

Despite this limitation, the X-ray lithography technique described here can be reliably employed to produce a structure with an aspect ratio of 3, a diameter of 100 µm, and a line width of 14.1 µm, suitable for producing a collimator. However, in order to achieve the target aspect ratio of 250, it is very difficult to make it because it is necessary to laminate 84 layers of the same structure. We found that there are process issues in this direct contact mask method. However, as shown in Figs. 3 – 5, this process can achieve the high processing accuracy for the top surface. Table 1 and 2 show summaries of the tracking dimensional accuracy for each process completion in this direct contact mask method and conventional mask procedure, respectively. Here, the evaluation results are shown as the results of the conventional procedure in the dihedral corner reflector arrays (DCRA) fabricated in the previous study [13]. The difference in size between the Cr glass mask and the product is less than 2.80 µm for the collimator mold, while 5.39~ 13.21 µm for the DCRA. These numbers were derived from a comparison of the numbers for each process in Table 1.2. The collimator mold made with the contact mask transfers the mask pattern more accurately. This is attributable to that the pattern distortion due to diffraction hardly occurs due to the direct bonding of the X-ray mask to the substrate

Table 1. The tracking dimensional accuracy for each process completion in this direct contact mask method.

	Cr glass mask	Contact mask	PMMA mold	Design value
Diameter	97.8±0.81 μm	96.7±0.89 μm	96.8±0.58 μm	100 μm
Line width	16.5±0.58 μm	16.5±0.3 μm	15.6±0.66 μm	14.1 μm
Sample number	10	10	10	

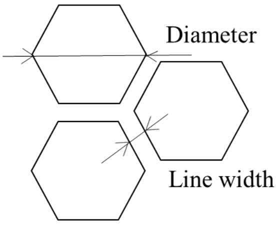

Table 2. The tracking dimensional accuracy for each process completion in conventional mask method.

	Cr glass mask	DCRA structure	Design value
Diameter	202.0±0.90 μm	208.2±2.19 μm	200 μm
Line width	41.7±0.91 μm	32.4±3.0 μm	40 μm
Sample number	10	10	

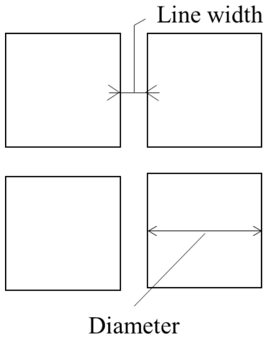

4. Conclusion

A honeycomb structure for an X-ray collimator mold was produced by microfabrication of PMMA using X-ray lithography. From multiple conditions, the higher the aspect ratio and the shorter the distance between the pillars, the greater the risk of structural collapse. From the experimental results, a structure having a hole diameter of 100 μm, an aperture ratio of 70%, and a height of 300 μm and an aspect ratio of 3 was achieved. However, in order to create the target structure, it is necessary to create a large number of similar structures. It is considered necessary to develop a novel process that can improve the aspect ratio that can be processed at one time. In addition, a method is required for preventing the sticking.

As mentioned above, although there are process issues to be improved, it has been shown that there is a direct contact mask method as one of the novel structure fabrication methods which can achieve high processing accuracy.

Acknowledgement

This research is supported by the 2018 and 2019 Space Science Committee.

References

1. L. Glesener, S. Krucker, S. Christe, S. –N. Ishikawa, J. C. Buitrago-Casas, B. Ramsey, M. Gubarev, T. Takahashi, S. Watanabe, S. Takeda, S. Courtade, P. Turin, S. McBride, V. Shourt, J. Hoberman, N. Foster, and J. Vievering, *Proc. SPIE* **9905** (2016) 99050E.
2. J.C. Buitrago-Casas, S. Christe, L. Glesener, S. Krucker, B. Ramsey, S. Bongiorno, K. Kilaru, P.S. Athiray, N. Narukage, and S. Ishikawa, *J. Instrumentation*, **15** (2020) 11032.
3. S. Krucker, S. Christe, L. Glesener, et al., *Astrophys. J.* **793** (2014) L32.
4. S. Christe, L. Glesener, C. Buitrago-Casas, et al., *J. Astron. Instrum.* **5** (2016) 1640005.
5. E. N. Parker, *Astrophys. J.* **330** (1988) 474.
6. S. Ishikawa, L. Glesener, S. Krucker, S. Christe, J. C. Buitrago-Casas, N. Narukage, and J. Vievering, *Nature Astronomy* **1** (2017) 771.
7. R. A. Nobles, L. W. Acton, E. G. Joki, J. W. Leibacher, and R. C. Peterson, *Appl. Opt.* **19** (1980) 2957.
8. J. Hrdy and P. Oberta, *Rev. Sci. Inst.* **79** (2008)

073105.

9. S. Kowarik, L. Bogula, S. Boitano, F. Carlà, H. Pithan, P. Schäfer, H. Wilming, A. Zykov, and L. Pithan, *Rev. Sci. Inst.* **90** (2019) 035102.
10. Q. Zhang, X. Yang, P. Li, G. Huang, S. Feng, C. Shen, B. Han, X. Zhang, F. Jin, F. Xu, and T. J. Lu, *Progress in Materials Science* **74** (2015) 332.
11. T. Thomas and G. Tiwari, *Int. J. Crashworthiness*, **24** (2019) 555.
12. Y. Utsumi, T. Kishimoto, T. Hattori, and H. Hara, *Jpn. J. Appl. Phys.* **44** (2005) 5500.
13. A. Yamaguchi, S. Maekawa, T. Yamane. I. Okada, and Y. Utsumi, *Transactions of The Japan Institute of Electronics Packaging*, **8** (2015) 23.
14. M. Takeuchi, A. Yamaguchi, Y. Utsumi, *J. Synchrotron Radiation*, **26** (2019) 528.
15. A. J. Sangster, R. L. Reuben, and U. Wallrabe, *Journal of Microelectromechanical Systems*, **7** (1998) 214.
16. Y. Hirai, S. Hafizovic, N. Matsuzuka, and J. G. Korvink, O. Tabata, *Journal of Microelectrochemical Systems*, **15** (2006) 159.
17. J. M. Park, J. H. Kim, J. S. Han, D. S. Shin, S. C. Park, S. H. Son, and S. J. Park, *Materials* **12** (2019) 2056.
18. G. Wells, S. Achenbach, V. Subramanian, M. Jacobs, D. Klymyshyn, S. Iyer, B. Moazed, J. Hanson, C. Shen, and D. Haluzan, *J. Synchrotron Radiation* **26** (2019) 565.
19. L. Wang, J. Pfeifer, C. Balázsi, I. M. Szilágyi, and P. I. Gouma, *Proc. SPIE*, **6769** (2007) 6769E1.
20. V. Saile, U. Wallradbe, O. Tabata, and J. G. Korvink, "*Advanced Micro and Nanosystems* Vol. **7** "LIGA and its Applications," (WILEY-VCH Verlag GmbH & Co. KgaA, Weinheim, 2009).

Effect of Sugar Chain Binding Mode on Water-soluble Micropatterning Performance and Physical Characteristics 187
Toru Amano, Makoto Kobayasi and Satoshi Takei

Low Stress and Low Temperature Curable Photosensitive Polyimide 195
Yu Shoji, Keika Hashimoto, Yutaro Koyama, Yuki Masuda, Hitoshi Araki and Masao Tomikawa

Effect of Cross-linker on Photosensitive Polyimide to Achieve Full Imidization and Lower Stress for Good Reliability 201
Ayaka Azuma, Satoshi Abe and Mamoru Sasaki

Purification Method for Achieving Low Trace Metals in Ultra-High Purity Chemicals 205
Mitsuaki Kobayashi, Yukihisa Okada, Takaaki Shirai, Osamu Sawajiri, Robert Gieger and Majid Entezarian

Study on Fabrication of X-ray Collimators by X-ray Lithography Using Synchrotron Radiation 213
Shunya Saegusa, Noriyuki Narukage, Yuichi Utsumi and Akinobu Yamaguchi

JOURNAL OF PHOTOPOLYMER SCIENCE AND TECHNOLOGY

Volume 34, Number 2, 2021

Computational Lithography for 3-Dimensional Fine Photolithography using Sophisticated Built-in Lens Mask 123
Tomoaki Osumi, Akio Misaka, Kousuke Sato, Masaaki Yasuda, Masaru Sasago and Yoshihiko Hirai

Impact of Water Treatment Reactor using TiO_2-coated Micropillar Made by UV-NIL 127
Kazuki Daigo, Ryota Akama, Noriyuki Unno, Shin-ichi Satake and Jun Taniguchi

Fabrication of Moth-eye Antireflective Nanostructures via Oxygen Ion-beam Etching on a UV-curable Polymer 133
Takao Okabe, Katsuyuki Yatagawa, Kazuki Fujiwara and Jun Taniguchi

Molecular Dynamics Simulation of the Resist Filling Process in UV-nanoimprint Lithography 139
Hiroki Uchida, Ryosuke Imoto, Tadashi Ando, Takao Okabe and Jun Taniguchi

Proposal of hybrid deep learning systems for process and material design in thermal nanoimprint lithography 145
Sou Tsukamoto, Hidekatsu Tanabe, Ryuhei Yamamura, Kai Kameyama, Hiroaki Kawata, Masaaki Yasuda and Yoshihiko Hirai

Flexible and Semi-Transparent Antenna for ISM Band Fabricated by Direct Laser Writing 149
Ashiqur Rahman and Akira Watanabe

Self-assembly of Amphiphilic Peptide in Phospholipid Membrane 155
Anju Kawakita, Noriyuki Uchida, Yunosuke Ryu and Takahiro Muraoka

Properties of Imidazolinium-containing Multiblock Amphiphile in Lipid Bilayer Membranes 161
Miki Mori and Kazushi Kinbara

Oriented Nanowire Arrays with Phthalocyanine – C_{60} Multi-Heterojunctions 167
Masaki Nobuoka, Koshi Kamiya, Shugo Sakaguchi, Akira Idesaki, Tetsuya Yamaki, Tsuneaki Sakurai and Shu Seki

Designed, Flexible Electrochromic Display Device with Fe(II)-Based Metallo-Supramolecular Polymer Using Mechanically Etched ITO Film 175
Masayoshi Higuchi and Yukio Fujii

Micropatterning Performance and Physical Characteristics of Water-soluble High Molecular Weight Polysaccharide Photoresist Materials 181
Toru Amano, Makoto Kobayasi and Satoshi Takei